

MSC. thesis

Exploration of LiDAR measured turbulence via met mast comparison, fatigue analysis & Measure Correlate Predict



MSc. thesis

Exploration of LiDAR measured turbulence via met mast comparison, fatigue analysis & Measure Correlate Predict

by

L. R. A. Pol

to obtain the degree of Master of Science Sustainable Energy Technology (SET) at the Delft University of Technology, to be defended publicly on Friday June 26, 2020 at 13:30 PM.

Student number: 4244877

Project duration: July 2019 – June 2020

Thesis committee: Dr. ir. W. A. A. M. Bierbooms, TU Delft, supervisor

Prof. dr. S. J. Watson, TU Delft
Dr. S. Basu, TU Delft
Drs. J. P. Coelingh, Vattenfall NV

This thesis is confidential and cannot be made public until June 26, 2022.

An electronic version of this thesis is available at http://repository.tudelft.nl/.





Preface

This thesis is the final step in completing the MSc. Sustainable Energy Technology at Delft University of Technology and also marks the end of my student life in Delft. I am sincerely happy that my time in Delft will come to an end. A time that brought me many learnings, interesting insights and useful knowledge. This master thesis project in particular has been tough and sometimes frustrating, but also gave me the opportunity to conduct research in the interesting field of wind energy. It was not always easy, but I have learned a lot on the way and have overcome many obstacles to arrive at this final product. I could not have done this without the help and support of several people.

Firstly, I would like to thank my supervisors for their help and guidance throughout the project. Jan Coelingh, you gave me the opportunity to conduct research at Vattenfall. An interesting environment, in which I found support and the possibility to take a closer look at the wind energy working field. Wim Bierbooms, you provided me with feedback on my work and helped me making decisions in the process of writing this thesis. Simon Watson and Sukanta Basu, thanks for joining my thesis committee and the help with my midterm and final presentation. Others at Delft University of Technology and Vattenfall, thanks for the valuable discussions and motivational pep talks.

Next to that, I want to express my utmost gratitude to my parents and sister: Jo, Nienke and Franca. They always supported me in every possible way and believed in me, not only during my thesis, but during my entire student time. It was not always easy and lasted a bit longer than necessary, but the final result is something to be happy about and proud of. Furthermore, all my friends who made my student time the most awesome period of my life so far, thank you for sharing all those great moments together. Finally, I would like to thank my loving girlfriend Davine. You helped me out at moments I was having a hard time and always kept confidence in me. Thanks a lot for supporting me last year and being there for me all the time.

L. R. A. Pol June 2020 Delft, The Netherlands

Abstract

Several factors play a role in the ongoing process of the acceptance and eventual universal use of LiDAR remote sensing technology in wind site assessment. Especially turbulence parameter TI is still giving food for thought. Three important aspects of LiDAR measured TI that are considered key are picked out and feature in this work, which attempts to contribute to the handling of LiDAR measured turbulence.

Firstly, the accuracy in measuring several wind characteristics compared to met masts, which have been the standard in wind science and industry for the past centuries, is an issue. This thesis evaluates a LiDAR met mast comparison for a Dutch onshore wind farm site to support the handling of the biases between both sources, with a focus on TI. It finds LiDAR suitable for basic wind measurements, but it still struggles with measuring turbulence accurately. Patterns in biases are exposed and explained and propositions of an alteration of the internal LiDAR correction factor \mathcal{C} , as well as the use of a new turbulence parameter called transience $\tau_{\rm m}$, are made.

The second factor addressed in this thesis is an indirect one and originates from the fact that turbulence, and so TI, plays an important role in the fatigue lifetime damage of a wind turbine. It is tried to answer the question what influence small biases in TI have on the fatigue lifetime damage of the tower and blades of a common wind turbine by means of a simulation based sensitivity study. Increments with an order of magnitude found in the first part of this work form an input for this. It is found that the fatigue damage due to stresses from certain bending moments is higher than others and that the blades and tower are affected differently by turbulence.

The third factor is related to the inherent flexibility of LiDAR devices. This forms a big advantage over met masts in general and also possibly paves the way for short-term measurement campaigns by LiDAR. It is proven that TI shows intra-annual variability, which would therefore require extrapolation techniques. The Measure Correlate Predict (MCP) methodology is chosen to conduct a case study on the application of several MCP algorithms on TI data, containing several experiments. It was found that the linear regression method (LR) is unsuitable for making long-term turbulence predictions, but that the variance ratio method (VR) shows promising results on the used performance metrics It seems that it does not matter whether the short-term data length is 3 or 6 months and that the picked season does not harm the final result significantly.

Contents

Lis	of Figures	xiii
Lis	of Tables	xvii
1	ntroduction .1 Research context	2 2 3
2	Theoretical background 2.1 Wind characteristics 2.1.1 Wind in the atmospheric boundary layer 2.1.2 Turbulence 2.2 Measuring wind characteristics 2.2.1 Conventional anemometry 2.2.2 Remote sensing techniques 2.3 Statistics for wind resource assessment 2.3.1 Uncertainty 2.3.2 Regression analysis 2.3.3 Accuracy and precision 2.3.4 Measure Correlate Predict methodology 2.4 Loads, moments and stresses on a onshore wind turbine	5 8 10 10 12 15 15 16 18 19
3	Literature review 3.1 History of wind resource assessment	25 27
4	Research Setup I.1 Research objectives	
5	Comparison of LiDAR and met mast 5.1 Method	36 36 42
6	Sensitivity analysis on fatigue lifetime of wind turbines 3.1 Method 6.1.1 Generating TI differentiated wind fields in TurbSim 6.1.2 Performing aeroelastic simulations in FAST 6.1.3 Fatigue lifetime determination with help of MLife 6.1.4 Method overview 3.2 Results 6.2.1 Interim results 6.2.2 Final results 5.3 Discussion and conclusion	55 59 62 65 65 65 68

viii Contents

7	Intra-annual variability of turbulence 7.1 Method	78
8	Application of MCP methodology on short LiDAR measurement campaigns 8.1 Method 8.1.1 Proceeding of applying Measure Correlate Predict methodology 8.1.2 Experimental setup 8.1.3 Performance metrics 8.2 Results 8.2.1 First step: Measure 8.2.2 Second step: Correlate 8.2.3 Third step: Predict 8.3 Discussion and conclusion	86 87 87 88 89 89
9	Conclusion and discussion	97
Α	Application of LR and VR MCP method on data sets with low coefficient of determination	101
В	Least-squares fit Weibull parameters	103
С	An example case study on the versatility of transience C.1 Argumentation for and setup of case study	
D	TurbSim input file	109
Ε	FAST input file	111
F	Chi-squared test example	113
G	Overview intermediate results for correlation step in MCP	115
Н	Overview final results for prediction step in MCP	119
Bi	bliography	121

Nomenclature

α	Wind shear exponent
β	Offset linear regression
$\chi^2_{ m norm}$	Normalized chi-squared statistic
$\Delta f_{\mathrm{Doppl}}$	ler Doppler frequency shift
ϵ	Bias between LiDAR and met mast measurements
λ_0	wavelength of the laser signal
μ	Dynamic viscosity of the fluid
μ	Population mean
$\mu_{ m norm}$	Normalized mean
\overline{U}	Mean part Reynolds averaged wind speed
ϕ	Azimuth angle LiDAR
ρ	Air density
ρ	Density fluid (air)
σ	Standard deviation
σ	Stress
$\sigma_{ m norm}$	Normalized standard deviation
σ_u	Standard deviation of mean wind speed
$ au_m$	Transience
θ	Cone angle LiDAR
$\theta_{ m d}$	Wind direction as observed by LiDAR
\boldsymbol{A}	Cup area exposed to wind
Α	Rotor area
а	Scale parameter Weibull distribution
С	Internal correction factor ZX300 LiDAR
C	Fitting constant MCP linear regression method
c_d	Drag coefficient
c_d	Tower drag coefficient
c_T	Thrust coefficient
$D_{ m life}$	Lifetime fatigue damage

Slope parameter linear regression

x Contents

D_T	Tower diameter
e	Standard deviation of bin MCP Mortimer method
$f_{ m bs}$	Frequency reference light beam
$f_{ m ref}$	Frequency back-scattered light beam
F_d	Drag force
F_T	Tower drag force
Н	Height LiDAR measurement
I_{x}	Area moment of inertia
k	Shape parameter Weibull distribution
L	Characteristic linear dimension
$L^{ m MF}$	Fixed mean of the load
$L^{ m RF}$	Cycle's load range around the fixed mean
$L^{ m ult}$	Ultimate design load component
Μ	Bending moment
m	Slope parameter MCP linear regression method
N	Population size
$n_i^{ m life}$	Cycle count fatigue damage
$N_{\rm month}$	Number of element in a certain month
$N_{\rm year}$	Number of element in a year
N_i	Cycles until failure
n_i	Number of elements in bin
P(TI)	Turbulence intensity probability distribution
r	Average ratio of bin MCP Mortimer method
r	Lever arm
R^2	Coefficient of determination
Re	Reynolds number
$SS_{\rm res}$	Residual sum of squares
SS_{tot}	Total sum of squares
T_{fail}	Time until failure
$T_{ m life}$	Design lifetime turbine
T_R	Thrust force
TI	Turbulence intensity
и	Fluctuating part Reynolds averaged wind speed
и	Horizontal wind speed

Contents xi

 u_{ref} Reference wind speed

 u_{Re} Characteristic velocity of the fluid

 $v_{\rm LOS}$ Line-of-sight velocity

Var Variance

W Vertical wind speed

x Independent variable linear regression

y Dependent variable linear regression

y Tower radius

z Height

 $z_{\rm ref}$ Reference height

List of Figures

1.1	Measuring wind characteristics, met mast versus LiDAR [9]
	Illustration of air flow characteristics and wind profile in the atmospheric boundary layer [10]
2.2	Extrapolation of a $u_{ref} = 12$ m/s at $z_{ref} = 80$ m using the power law. Varying α results in different wind profiles
	Time series of wind speed. The fluctuating part of the wind speed is implicitly visible as the deviation of the blue line around the mean wind speed in red
	IEC turbulence classes for classifying sites [98]
	Top of a typical lattice met mast with mounted meteorological instruments and auxiliary devices
	LiDAR measurement set-up, indicating the LOS velocity and the conical shaped measurement volume
2.7	Gaussian or normal distribution for different values of μ and σ^2 , indicating population mean and spread [1]
	The principle of linear regression [15]
	The principle of ordinary least squares, used in determining the coefficient of determination R^2 [5]
2.10	Four situations describing the definitions of accuracy and precision [77]
2.11	Visual conceptualisation of the general idea of the Measure Correlate Predict methodology [126]
2.12	Aerodynamic loading on a wind turbine, with wind speed U visually decomposed in a mean and fluctuating part [46]
2.13	Sketch representing a wind turbine tower idealized as a 2D cantilever beam, with indicated forces F and moments M [42]
2.14	Wind turbine tower segment to illustrate determination of stresses at the node indicated by the arrow. A certain bending moment is present caused by an aero-dynamic thrust force and a lever arm derived from the cantilever beam model
	of the wind turbine tower. Together with radius y and area moment of inertia I_x , stresses are calculated by means of Equation 2.19 [125]
3.1 3.2	The growth of the average size of wind turbines in the period 1980-2015 [14] . Typical example of the results of a forced OLS regression for comparing LiDAR and cup anemometer TI measurements in the three ABL stability regions, indicating data set size, slope parameter α and coefficient of determination R^2 [81]. Note that the TI is given in percentages here, where throughout this thesis TI is
	given in absolute terms
	Windplan Blauw in northern Flevoland [8]
+.∠	(yellow triangles)
4.3	ZX 300 CW LiDAR device [9]
	Wind rose retrieved from measurement data of met mast 1
5.1	Time series average wind speed \overline{U} at 100 m height for visual comparison of LiDAR 1 and met mast 1
5.2	Time series standard deviations $\sigma_{\rm u}t$ at 100 m height for LiDAR met mast pair 1 of one day: 25-03-2019

xiv List of Figures

5.3	Determining scale parameter a and shape parameter k of the Weibull distribution. On the left the first step: a least squares fit to determine both parameters, and on the right the second step: visualizing the wind speed distribution by	
		39
5.4	Scatter plot of horizontal wind speeds for LiDAR met mast pair 1 at 100 m height. The data in red is excluded in the filtering step since the threshold of $U > 3$ m/s	20
	Scatter plot of horizontal wind speeds for LiDAR met mast pair 1 at 160 m height	39 40
		41
5.7	Wind roses retrieved from LiDAR met mast pair 1 measurements at two different heights	41
	Time series of the week of 03-06-2019, showing turbulence intensity TI at 160 m height for LiDAR met mast pair 1	42
5.9	Time series turbulence intensity TI at 160 m height for visual comparison of LiDAR 1 and met mast 1. This time series covers two days, 8 and 9 June 2019,	40
5.10	Wind speed versus TI at 160 m height from met mast 1 and LiDAR 1. The red	43 44
5.11	I Scatter plots of turbulence intensity measured by LiDAR met mast pair 1 for three different heights. Unfiltered and filtered data are shown in red and blue	
5.12	<u>e</u>	46
	and LiDAR 1	47 48
5.14	Correction factor C as a function of height H in red, proposition for modification in blue	53
6.1	Visualization of an example wind field from TurbSim with a low resolution of grid points, wind speed components u , v and w and the element of time in the form of the consecutive square grids [41]	56
6.2	Standard IEC turbulence categories and classes and their implications on TI	57
6.3	Visualization of an example output of full-field binary time-series data derived from TurbSim of the horizontal u component of the wind speed at different	51
6.4		58
	red box [65]	59
	L J	63 64
6.7	Overview conceptual working of FAST and MLife	65
	Horizontal wind speed component <i>u</i> at the rotor hub of the NREL baseline turbine	66
		00
		66 67
	DBlade root bending moments for <i>TI</i> = 0.09	67
6.11	OBlade root bending moments for $TI = 0.09$	67 67
6.11 6.12	OBlade root bending moments for $TI = 0.09$	67 67 69
6.11 6.12 6.13	Blade root bending moments for $TI = 0.09$	67 67
6.11 6.12 6.13 6.14	Blade root bending moments for $TI = 0.09$	67 67 69 70

List of Figures xv

7.2	The turbulence intensity probability distribution $P(TI_i)$ for every month of 2019 as measured by LiDAR 1, visualized by the orange histograms. The blue his-	
7.3	togram in the background is the $P(TI_i)$ for entire 2019	79
7.4	same year	80
7.5	togram in the background is the $P(TI_i)$ for entire 2019 Yearly pattern of horizontal wind speed U and standard deviation σ_{u} at 100 m	80
	height for both LiDARs	81
	2019	82
8.1 8.2	Flowchart of the Measure Correlate Predict methodology. The grey areas refer to the measured data, the red area includes the second step wherein a correlation is established and the blue area depicts the last step: the prediction	86
	mast (below), with the black dotted lines indicating the four quarters of 2019 that serve as input for the MCP procedure	89
8.4	Prediction via both MCP algorithms for experiment 1	91 92
8.5	Prediction via both MCP algorithms for experiment 5	93
	Data set with high R^2 in linear regression	101 102
C.1	The principle of rainflow-counting used on stress cycles for fatigue determination [35]	106
D.1	Graphic of one of the used TurbSim input files	109
E.1	Graphic of one of the used FAST input files	111
	Bin counts of expected and observed data points	113 114
	Correlation via both MCP algorithms for experiment 2 - wind direction sector 3 Correlation via both MCP algorithms for experiment 2 - wind direction sector 6	116 117
H.2	Prediction via both MCP algorithms for experiment 2	119 120 120

List of Tables

2.1	Properties of ABL stability classes [120]	8
3.1	Overview advantages cup anemometers	23
4.2 4.3	ZX 300 CW LiDAR specifications [9]	31 31 32 32
5.1	Data availability of both met masts and ZX 300 LiDARs for different measurement heights	36
	Comparison of \overline{U} and $\sigma_{\rm u}$ at 100 m of both LiDAR met mast pairs Obtained Weibull distribution parameters for both LiDAR met mast pairs by	37
	applying least squares fit	39
	met mast pairs compared by means of coefficients of determination R^2 , slope parameter α and offset β for different heights	40
	Correction factors used by the ZX300 LiDARs for different ranges of height Comparison of measured turbulence intensity at three heights by pair 1 and two heights by pair 2 by means of the earlier explained metrics: bias between mean	42
5.7	turbulence intensity ϵ_{TI} , standard deviation σ_{TI} and its accompanying bias ϵ_{σ} . Precision and accuracy of TI measurements from both LiDAR met mast pairs	43
	compared by means of coefficients of determination R^2 , slope parameter α and offset β for three different heights	45
5.8	Comparison of μ_{TI} at two heights and for both direction sectors for LiDAR met mast pair 1	47
5.9	Precision and accuracy of TI measurements from LiDAR met mast pair 1 compared by means of coefficients of determination R^2 , slope parameter α and offset β for both defined wind direction sectors	48
	Overview of used turbine/model specifications and meteorological boundary conditions in TurbSim, which are required input parameters to simulate turbulent wind fields	56
	Overview input parameters and files for FAST simulation	60
	General specification of the widely used 5 MW baseline wind turbine developed for research purposes by NREL [64]	61
6.4	Placement of strain gauges in terms of distance in meters from tower base and blade root	61
6.5	Results obtained for tower lifetime fatigue damage calculations in MLife for three <i>TI</i> values, three Wöhler exponents <i>m</i> and due to stresses from side-to-side bending moments and fore-aft bending moments	68
6.6	Results obtained for blade lifetime fatigue damage calculations in MLife for three <i>TI</i> values, three Wöhler exponents <i>m</i> and due to stresses from edgewise bending	00
	moments and flapwise bending moments	71
	Experimental setup of MCP study	87
-	iment: April - June	90

xviii List of Tables

8.3	Intermediate results on correlation for both MCP methods for the sixth experiment: July - December	90
8.4	Resulting performance metrics of the six experiments for both MCP methods .	
C.1	Overview of an example selection of 10 minute intervals with their corresponding values for standard deviation and mean horizontal wind speed over that interval	107
G.1	Intermediate results on correlation for both MCP methods for the first experiment: January - March	115
G.2	Intermediate results on correlation for both MCP methods for the third experiment: July - September	115
G.3	Intermediate results on correlation for both MCP methods for the fourth experiment: October - December	116
G.4	Intermediate results on correlation for both MCP methods for the fifth experiment: January - July	

1

Introduction

To get acquainted with the topic of this thesis and to sketch the importance and relevance of this research, a general context around the topic of measuring wind characteristics by means of LiDAR is provided in Section 1.1. The knowledge gap and problem statement as observed by the author are treated in Section 1.2. This resulted in the aim and scope of this research, which are stated in Section 1.3. The aim of this research was then translated into three research objectives, which are set out in Section 1.4. The outline of this thesis is presented in Section 1.5.

1.1. Research context

All around the world, climate agreements are signed and goals are set to mitigate the effects of the ongoing climate change that is threatening the natural habitat of humanity. With the preservation of the current state of our planet at risk, all kinds of measures are taken to slow down global warming [40]. One of the most important pillars of this set of measures is the change from using polluting fossil fuels (e.g. coal, petroleum and natural gas) to meet our growing energy and electricity demand, to renewable energy sources like solar, wind and hydro power. Besides climatological reasons, unwanted dependence on fossil fuel rich countries, ongoing global electrification of energy demand and the still relentless depletion of raw materials are playing an important role in this energy transition [116].

Although the phenomenon of wind energy was discovered much earlier by humankind, the utilization of the wind to generate electricity by means of wind turbines took rise from the oil crises in the 1970s and triggered research in Denmark and the USA [74]. Nowadays, wind energy is the second largest renewable energy source after hydro power, accounting for 7% of global energy demand. From the fact that the globally installed wind power capacity increased by a factor of 50 to more than 600 GW in the last two decades, it can be derived that wind industry is now mature and a major global player [19]. The proximity of spiritual father Denmark and front runners Germany and UK, the windy northwest European climate and the scarce area form the excellent recipe for Dutch on- and offshore wind projects.

Simultaneously with the above developments, a growth in size and lifetime for wind turbines is clearly visible. New turbines of over 10 MW are no exception anymore and are reaching towards 200 meters and higher. Higher and longer lasting turbines make the accuracy of the prediction of lifetime energy yield increasingly important [107]. This prediction starts with measuring several important wind characteristics, like vertical and horizontal wind speed, wind direction and turbulence intensity (TI), and was usually solely done by so-called meteorological masts (met masts). A met mast is a free standing tower, which carries meteorological instruments such as thermometers, wind vanes and anemometers at different heights up to the turbine hub height, and is considered 'the standard' in wind energy industry [20].

2 1. Introduction

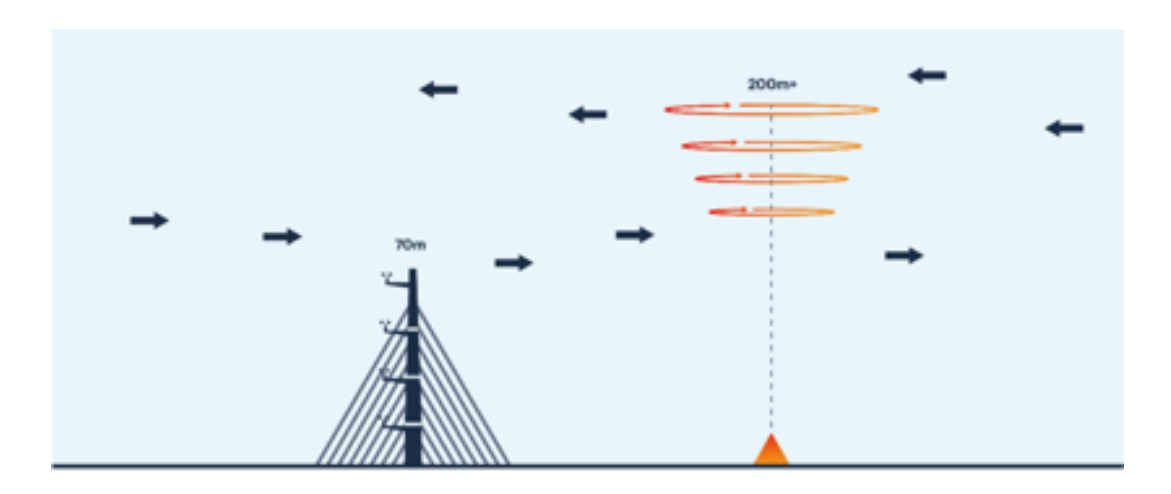


Figure 1.1: Measuring wind characteristics, met mast versus LiDAR [9]

Together with the increasing height and thereby costs of met masts in the past decade came the rise of remote sensing based devices like LiDAR (Light Detection and Ranging), trying to take over the place of conventional anemometry in wind industry [38]. LiDAR devices are relatively small and movable and do not require permits (time) or guy wires and construction (space), like met masts. Next to that, LiDARs are able to measure all important wind parameters at different heights from 10 - 200 m [18]. Where prizes of LiDAR devices are already below €100.000 and declining, the total costs for erecting a 150 to 200 m high met mast are around double that amount. Besides, LiDAR devices can also be leased for shorter periods at lower costs. Figure 1.1 visualizes the different configuration and measurement principle of both techniques.

1.2. Problem statement

Although several studies have shown that these promising devices are able to accurately measure wind speeds, LiDAR is not yet completely trusted by the leading International Electrotechnical Commission (IEC) to serve as stand-alone measurement unit (so without the proximity of a met mast) to measure another important wind site characteristic: turbulence [104]. In wind energy, turbulence is defined as the chaotic, short-term deviation of the wind speed from its mean value and is usually quantified in the turbulence intensity TI.

The influence of TI on annual energy production (AEP) and fatigue lifetime of wind turbines can be significant, which underlines the importance of accurate and reliable TI measurements by LiDAR devices [86]. Since LiDARs devices are still quite expensive, they are not rarely leased for a few months or years. This creates the urge for as short as possible measurement campaigns, without the loss of accuracy. Measure Correlate Predict is a known method used to extrapolate short-term wind speed data [115], but experience and best practices with LiDAR measured TI are lacking. Increasing size of the parts of a wind turbine and longer lifetime of wind turbines enlarges the importance of accurate fatigue lifetime calculations [45]. Although under investigation, the quantitative sensitivity of fatigue lifetime for TI is not yet fully understood and gives room for further research.

1.3. Aim and scope

This research aims to compare the measurements of two LiDARs from a Dutch onshore wind site with those of accompanying met masts to assess their accuracy, especially for turbulence measurements, and to provide a framework for comparing both in such terrain. This encompasses also the possible identification of parameters that are influencing this LiDAR TI accuracy, like wind direction, height, wind speed or diurnal patterns.

Since this thesis assesses the accuracy of LiDAR measured TI, it is worth investigating the effect of an uncertainty interval for TI on the fatigue lifetime of commonly used turbines at Dutch onshore wind sites. Simulated TI differentiated wind fields are used to generate time series of loads on a wind turbine. These loads are then used to calculate damage equivalent loads, time until failure and fatigue lifetime damage.

Because time and use of LiDAR are still quite valuable, attempts will be made to use Measure Correlate Predict (MCP) methods to use short-term TI LiDAR data and long-term reference data from a nearby met mast to 'create' long-term data. The goal here is to see whether it is possible to shorten LiDAR measurement campaigns without loss of accuracy and identify the best MCP method for the average Dutch wind site.

1.4. Research objectives

To summarize and complement the above, the following three research objectives are formulated for this research:

- Assess statistical accuracy and factors influencing this accuracy of ZX300 Continuous Wave LiDARs at Dutch onshore wind sites by comparing them with proximate met masts, especially concerning turbulence (TI)
- Assess **sensitivity of the fatigue lifetime** of a commonly used wind turbine at Dutch onshore wind sites as a function of TI to **quantify the effect of TI on fatigue**
- Use MCP to extrapolate short-term LiDAR TI data (in reference to long-term met mast data) to investigate possibilities of shortening LiDAR measurement campaigns and identify most accurate and workable MCP method by comparing mutual results

1.5. Thesis outline and reading guide

After this introductory chapter, theoretical background knowledge about wind characteristics like TI, measuring methods like conventional anemometry and LiDAR, statistics, Measure Correlate Predict methods and fatigue lifetime for wind turbines is provided in Chapter 2. Having this background information is deemed to be necessary or convenient to properly interpret the remaining parts of this thesis. In Chapter 3, a literature review attempts to give an overview of the current state of research on the subjects of LiDAR replacing met masts, the role of TI in wind industry, MCP methods used for turbulence and the influence of TI on fatigue lifetime of wind turbines. It is primarily important how this research can be placed in the existing scientific framework around LiDAR versus met mast, especially regarding TI. Chapter 4 focuses on the research setup, in which is elucidated on the formulated research objectives and a detailed description of the measurement sites and used instruments is given.

Chapter 5 addresses the first research objective, assessing the accuracy of CW LiDAR, and is roughly subdivided in two parts: a preliminary study on several wind characteristics and the main part which deals with the accuracy of LiDAR measured turbulence intensity and factors influencing this accuracy. Chapter 6 comprises of the sensitivity analysis from the second research objective, assessing the influence of turbulence intensity on the fatigue lifetime of a wind turbine. Chapter 7 explores the intra-annual variability of TI and serves as an input for the next Chapter 8 and the third research objective. In this chapter, the Measure Correlate Predict (MCP) methodology is applied to the TI measurement data derived from the conducted measurement campaign. Several MCP methods are researched and mutually compared. The overall results are discussed in Chapter 9, where conclusions are drawn and recommendations are made.

Theoretical background

This chapter explains several theoretical notions important for complete understanding of the matter treated in this thesis. Section 2.1 deals with wind characteristics like the atmospheric boundary layer, wind shear, stability, wind speed and turbulence. Section 2.2 treats measuring these wind characteristics by means of in met masts incorporated anemometry and remote sensing based devices like LiDAR. Section 2.3 elaborates on the statistics of measuring the earlier described wind characteristics. Uncertainty quantification, regression analysis, accuracy and the Measure Correlate Predict methodology are discussed here. Finally, 2.4 presents an introduction to loads and stresses on onshore wind turbines. Some matter will explicitly return in the next chapters, but parts of this chapter serve just as a solid knowledge basis.

2.1. Wind characteristics

The wind has fascinated humanity for a long time and has been tried to utilize in many different ways ever since. For the nowadays delicate and important applications in wind energy, this utilization of the wind inevitably goes hand in glove with the precise qualification and quantification of the wind and its characteristics. Section 2.1.1 deals with wind in the atmospheric boundary layer and introduces the concepts of wind shear and stability. In Section 2.1.2, turbulence and the important turbulence parameter turbulence intensity (TI), are treated.

2.1.1. Wind in the atmospheric boundary layer

Atmospheric boundary layer - The atmospheric boundary layer (ABL) or planetary boundary layer (PBL) covers the lowest part of the troposphere. The troposphere is that portion of the atmosphere where most weather occurs; the lowest 10 to 20 km of the atmosphere. Higher in the troposphere, above the ABL, the wind is 'free' and approximately geostrophic, which means the wind is parallel to the isobars. Within the ABL, surface drag from the Earth's surface directly influences the wind, causing it to turn less parallel to the isobars [112]. The height of the ABL ranges from a few hundred meters up to 2 kilometres, varying over time depending on its stability. Physical quantities such as wind speed, temperature and moisture display rapid fluctuations in the ABL. As in any flow where a wall or boundary is present, viscous properties of the medium tend to induce shear forces that slow down the medium. This effect increases in strength approaching the boundary and has typically a logarithmic-like shape. The lower tenth of the ABL is defined as the surface layer (SL) and is the region of the ABL where the above described effect of shear is mostly present [112]. In Figure 2.1, the most important aspects in the ABL are visualised.

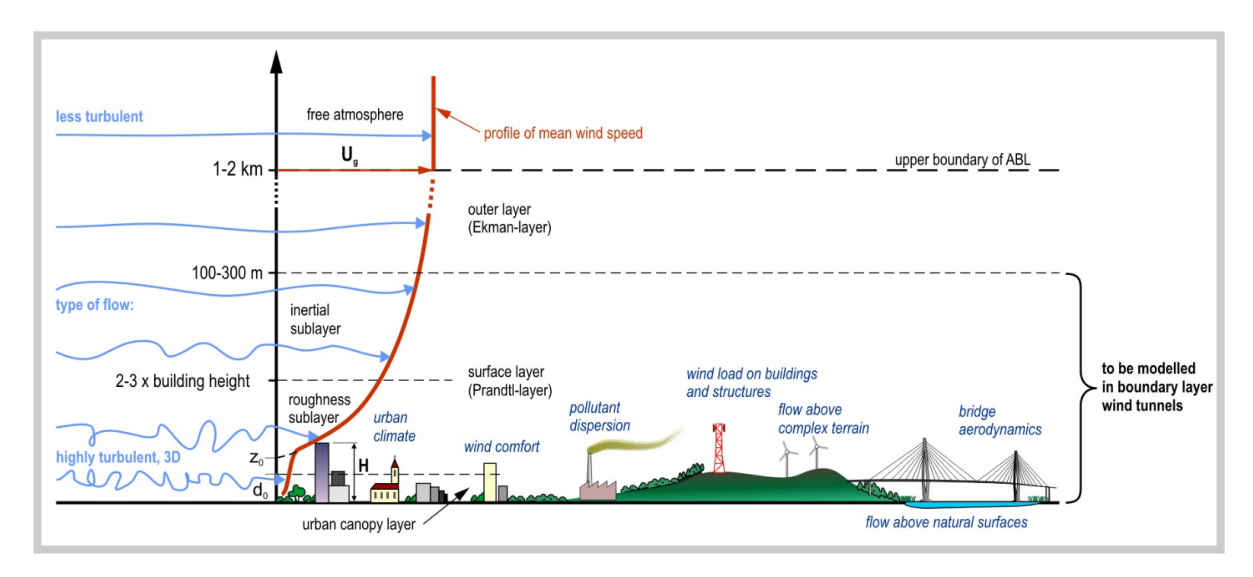


Figure 2.1: Illustration of air flow characteristics and wind profile in the atmospheric boundary layer [10]

Wind shear – The present effect of wind shear in the atmospheric boundary layer is known to be dependent on several atmospheric and surrounding variables, like surface roughness, landscape, radiative forcing, obstacles and buildings. Wind shear in the ABL is often expressed with the help of the shear exponent α . This factor helps to compute and visualize different wind profiles and is utilized in the so-called power law. Although being fully empirical and limited in its validity to the surface layer (up to 200 m), it is widely used for wind turbine design purposes because of its simplicity [87]. The power law is given by Equation 2.1,

$$u(z) = u_{ref} \left(\frac{z}{z_{ref}}\right)^{\alpha} \tag{2.1}$$

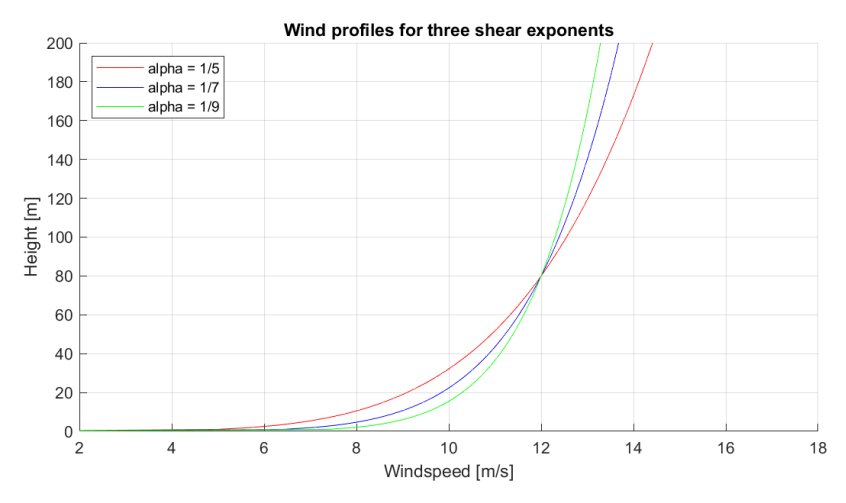


Figure 2.2: Extrapolation of a u_{ref} = 12 m/s at z_{ref} = 80 m using the power law. Varying α results in different wind profiles.

where α is the shear exponent, u_{ref} the reference wind speed, z_{ref} the reference height and z the height of interest. When α is known, a measured wind speed at a certain height can be used to extrapolate this wind speed to other heights, forming a wind profile. A common value for α when considering flat onshore terrain is 1/7, which is used when on-site data is not available for a sufficient number of heights. The effect of different wind shear exponents is visualized in Figure 2.2.

2.1. Wind characteristics 7

Stability classification ABL - Characteristic for the ABL is its quick response to changes in surface radiative forcing. Concerning fair weather over land, the ABL has a marked diurnal cycle. During daytime, the Sun heats up Earth's surface, resulting in a positive heat flux coming from the surface. During night-time, an opposite negative heat flux towards the Earth's surface is present. These and other buoyancy forces affect the wind profile in the ABL significantly and their effects are indicated by the stability of the ABL or the atmospheric stability. The latter is defined as the tendency to resist vertical motion or to suppress existing turbulence. This turbulence can be induced thermally, by the Sun, or mechanically, by friction with the Earth [50].

Atmospheric stability can be classified into three categories: unstable, stable and neutral. An unstable ABL is characterized by increased turbulence and lots of vertical mixing. These are caused by heated air, rising from the ground to form large convection cells, resulting in increasingly homogeneous vertical wind speed profiles. In stable conditions, the opposite situation is present. Turbulent activity and convective processes are suppressed and wind shear is enhanced. A neutral atmospheric boundary layer is in thermal equilibrium with its surroundings and is likely to be found during overcast days with strong winds. The latter makes turbulence from surface roughness to cause sufficient mixing of the ABL [56]. A neutral atmosphere is an important situation for wind energy, especially for fatigue loading, keeping in mind that the strongest winds are blowing at that time.

Monin-Obukhov - Quantification of stability and determination of stability class can be done in several ways. Commonly, the Monin-Obukhov length or simply Obukhov length L_{mo} is used. This is a length parameter defined as the height above the ground where mechanically and thermally created turbulence are in balance [83]. Where mechanical turbulence is the effect of shear, thermal turbulence is caused by heating of the atmosphere by the Sun. The Monin-Obukhov length L_{mo} is defined by Equation 2.2,

$$L_{mo} = -\frac{u_*^3 \theta_v}{\kappa g(w' \theta_v')_s} \tag{2.2}$$

in which u_* is the friction velocity, θ_v is the virtual temperature, κ is the von Kármán constant, g is the gravitational acceleration and $(w^{'}\theta_v^{'})$ surface potential temperature flux. Where L > 0 indicates an stable atmosphere, L < 0 indicates a unstable atmosphere. By definition, $L_{mo} \to \infty$ under neutral conditions, adapted from [83]. An important application of the Monin-Obukhov length is another proposition of a relationship between height and wind speed. According to Monin-Obukhov similarity theory, Equation 2.3 describes this relationship using L_{mo} and is valid for all stability classes.

$$u(z) = \frac{u_*}{\kappa} \left[ln \left(\frac{z}{z_0} \right) - \phi_m \left(\frac{z}{L} \right) \right]$$
 (2.3)

Here z_0 is the aerodynamic surface roughness length, ϕ_m is the correction function and z/L is the stability parameter. This so-called logarithmic wind profile is the counterpart of the earlier discussed power law profile.

Overview stability parameters – It has been shown that the Obukhov length can be used to classify atmospheric stability and Monin-Obukhov similarity theory dictates the formula in Equation 2.3 for the relationship between wind speed and height in the surface layer. The earlier discussed wind shear, which was used in the power law wind profile, can be utilized to classify atmospheric stability too, just as several other factors. For that reason an overview of the characteristics of the stability classes, as well as factors that can be used to identify these classes, are shown in Table 2.1.

Stability class	Stable	Neutral	Unstable
Actual lapse rate	$> (dT/dz)_{adiabatic}$	$(dT/dz)_{adiabatic}$	$< (dT/dz)_{adiabatic}$
Wind speed	Strong	Strongest	Low
Wind shear	Highest	Logarithmic	Low
Shear exponent	0.2 < <i>α</i>	$0.1 < \alpha < 0.2$	α < 0.1
Obukhov length	$L_{mo} > 0$	$L_{mo} \rightarrow \infty$	$L_{mo} < 0$
Turbulence	Weak, mechanical	Moderate	Vigorous, thermal
TI	<i>TI</i> < 0.1	0.1 < TI < 0.13	<i>TI</i> > 0.13
Typical weather	cloudless nights	overcast afternoon	sunny cloudless
Layer depth	shallow, 20 - 500 m	200 m - 1 km	thick, up to 2 km

Table 2.1: Properties of ABL stability classes [120]

2.1.2. Turbulence

Definition – Fluid dynamics defines turbulence as fluid motion characterized by chaotic changes in pressure and flow velocity. Turbulent flow is the counterpart of laminar flow, which implies a fluid flow in parallel layers, without disruption between those layers. The presence of excessive kinetic energy in parts of the fluid flow, which are making it possible to overcome the damping effect of the fluid's viscosity, are the cause of the phenomenon of turbulence. Turbulence therefore commonly occurs in low viscosity fluids, like air, and is characterized by unsteady vortices of different sizes interacting with each other. Consequently, friction effects between these vortices increase drag forces in the fluid [74].

The vortices in turbulent flow are called eddies, which are dissipative in nature. Eddies of different sizes break down into smaller eddies over time. In this so-called energy cascade, kinetic energy is transferred to successively smaller length scales. This cascading process of turbulence continues until the Reynolds number of 4000 is reached, when the length scale is sufficiently small for the viscous properties of the fluid to dissipate the kinetic energy into heat [86]. In other words, an air flow becomes more turbulent for higher values of the dimensionless Reynolds number and vice versa. It should be noted that the occurrence of turbulence is far from binary, there actually exists a large transient range of 2500 < Re < 10,000. The Reynolds number Re is defined as the ratio of kinetic energy to viscous damping in a fluid flow described by Equation 2.4:

$$Re = \frac{\rho uL}{\mu} \tag{2.4}$$

where ρ is the density of the fluid, u is the characteristic velocity of the fluid, L is a characteristic linear dimension and μ is the dynamic viscosity of the fluid. Although the onset of turbulence can be predicted by the Reynolds number, turbulence is considered a very complex and not-totally analytically solved physical phenomenon [29]. A rough classification of turbulence aligns with the classification of atmospheric stability, as can be seen in Table 2.1. Where in a stable atmospheric boundary layer (ABL), turbulence is weak and induced mechanically, turbulence is vigorous and thermally induced in an unstable ABL. Turbulence is moderate is a neutral atmosphere.

Turbulence intensity – Turbulence can not be neglected in wind resource assessment. Although its effects are not completely understood, it is known to influence the power generation and fatigue lifetime of wind turbines [21]. For wind resource assessment applications, turbulence is usually quantified using the turbulence intensity (TI). The turbulence intensity is defined as the standard deviation of the wind speed over the mean of the wind speed and is calculated by convention based on the 10 minute average horizontal wind speed. For obtaining the turbulence intensity of a 10 minute interval, the wind speed should be Reynolds averaged to find two components: the mean and the fluctuating part [86].

2.1. Wind characteristics 9

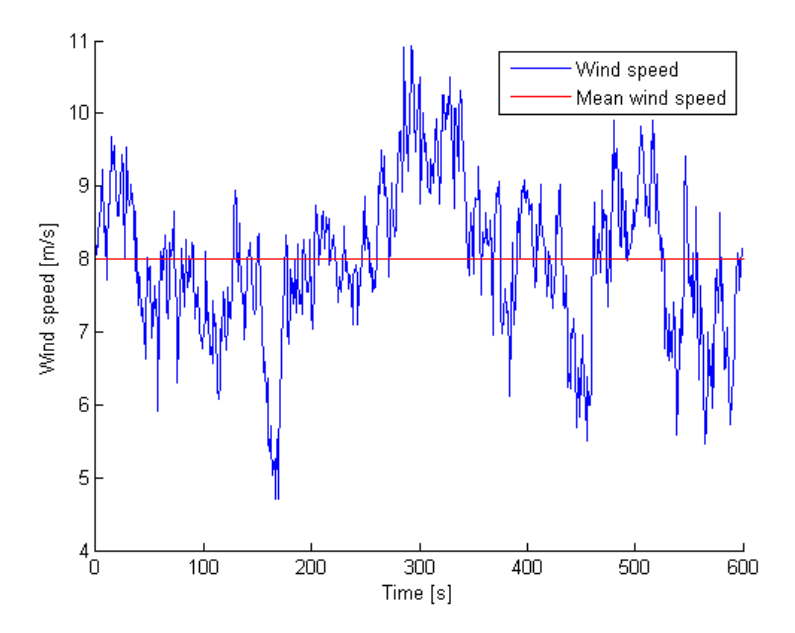


Figure 2.3: Time series of wind speed. The fluctuating part of the wind speed is implicitly visible as the deviation of the blue line around the mean wind speed in red.

Equation 2.5 shows the Reynolds averaging of the wind speed, where the mean part is denoted by \overline{U} and the fluctuating part by u. Both are used to determine the TI, as can be seen in Equation 2.6, where σ_u is the standard deviation of the fluctuating part. This fluctuating part represents the turbulent part of the wind speed and has a mean of 0 by definition. Figure 2.3 depicts both parts, illustrating the principle of superposition allowing the summation of both parts.

$$\overline{U} = \frac{1}{\Delta t} \int_0^{\Delta t} U(t)dt \qquad \overline{U}^3 = \overline{(\overline{U} + u)^3}$$
 (2.5)

$$TI = \frac{\sigma_u}{\overline{II}} \tag{2.6}$$

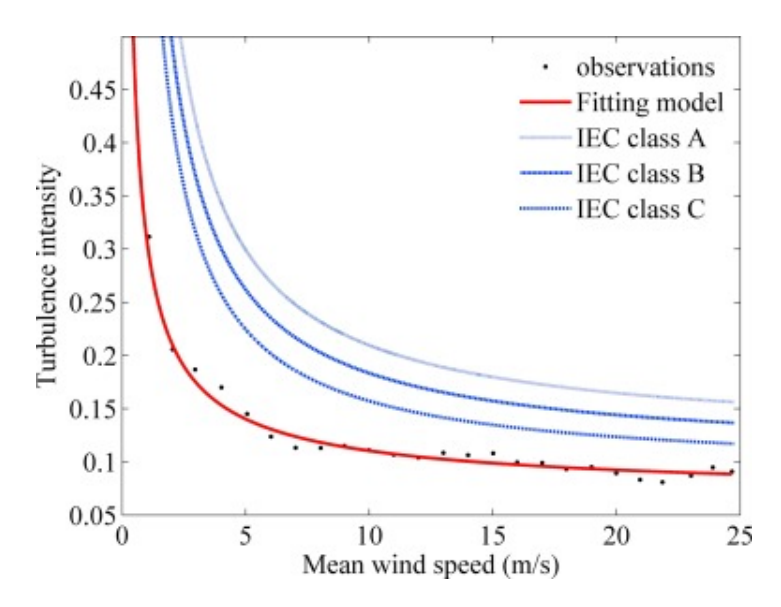


Figure 2.4: IEC turbulence classes for classifying sites [98]

As found out in Section 2.1.1, the turbulence intensity can be related to the atmospheric stability regions as summarized in Table 2.1. Where TI values < 0.1 indicate a stable atmosphere, the ABL can be classified as unstable for TI > 0.13. For values in between both values, neutral conditions apply. TI is also dependent on the aerodynamic surface roughness z_0 of the site, as introduced in Section 2.1.1. A low surface roughness is associated with less obstacles on site, causing low TI values, and high surface roughness implies a higher turbulence intensity. The International Electrochemical Organization maintains three classes for TI, illustrated in Figure 2.4. These rather conservative classes, basically serve as a recommended ceiling for TI distributions of onshore wind sites.

2.2. Measuring wind characteristics

Measuring wind characteristics like horizontal wind speed, vertical wind speed, wind direction and turbulence intensity (TI) as well as other meteorological parameters like temperature, pressure and humidity in site measurement campaigns was conventionally done by the use of so-called met masts. These tall construction towers are usually installed close to future wind turbine locations, where they perform several kinds of measurements at different heights with the help of meteorological instruments like anemometers, wind vanes, barometers and thermometers, amongst others. Section 2.2.1 describes the general principle of meteorological masts and anemometry in particular, highlighting the types, working principle and (dis-)advantages of anemometers. Special attention is given to cup anemometry, since this type of anemometer is used throughout this thesis.

Together with the continuous growth in size of multi-megawatt turbines goes the development of remote sensing techniques for measuring the same wind characteristics as by conventional met masts. LiDAR (Light Detection And Ranging) and SoDAR (Sonic Detection And Ranging) are surveying methods used in site measurement campaigns, on the roll to partly of even fully replace conventional anemometry. Section 2.2.2 firstly gives an overview to the remote sensing devices used in wind industry in general, after which there will be focused specifically on continuous wave (CW) LiDARs. The latter is the type of LiDAR used for the measurements in this thesis and there will be touched upon its working principle and (dis-)advantages.

2.2.1. Conventional anemometry

Met masts – Meteorological masts often appear as steel tubular or lattice masts with meteorological instruments mounted on the masts at different heights, usually up to hub height. These instruments measure wind- and meteorological characteristics at e.g. 10, 40, 60, 80, 100 and 120 m, after which inter- and extrapolation are used to retrieve data for all desired heights. With the help of a concrete construction base and guy-wires that are attached to the steel tubes or lattice of the mast and concrete anchors in the field around the met mast, the usually between 50 and 150 m high masts are held safely in place. As said, met masts are equipped with various sensors and instruments. These include barometers to measure pressure, thermometers to measure temperature, wind or weather vanes to determine wind direction and most important of all, anemometers to measure wind speed. The latter is also used to calculate the turbulence intensity. Since the anemometer is by far the most important instrument on a met mast, this device is, usually in contrast to the other instruments, mounted at different heights.

Possibilities and limitations - A huge advantage of met masts in general is their reliability and the acquaintance with the construction and utilization of these tall towers. The large and long-term experience with retrieving accurate and precise data from met masts and their instruments induces the current condition of met masts and conventional anemometry as state-of-the-art in industry and science. However, the increasing size of modern wind turbines enlarges several disadvantages of met masts. Firstly, the amount of time and costs arising from requesting permits for the commissioning of the whole construction tends to increase even more. Secondly, the construction time and costs of the mast and extra instru-

ments mounted on the mast itself will also rise further. The third disadvantage lies in the ascending inaccuracy of the data retrieved from met masts that is used for modern onshore multi-megawatt turbines. Since extrapolation of met mast data to desired heights is used more and more nowadays at sites with turbine rotor area heights between 100 and 200 m, data from met masts becomes less accurate and precise. This highlights also the fourth, already present disadvantage of met masts: they only measure wind characteristics at heights where sensors or instruments are installed. To conclude with the most important disadvantage: met masts are always distorting the air flow around it to some extent and thereby induce a measurement bias in the mounted anemometers.



Figure 2.5: Top of a typical lattice met mast with mounted meteorological instruments and auxiliary devices

Anemometers – Measuring wind speed via an anemometer dates back from the 15th century, but only in 1926 Canadian meteorologist John Patterson invented the most wellknown, three-cup anemometer that is widely used today in disciplines like meteorology, aircraft and wind energy. Others supplemented this device with minor improvements and the possibility to measure wind direction as well [92]. Although the three-cup anemometer is considered as the standard anemometer in industry, several other types of anemometers were developed throughout the years. Vane, hot wire and sonic anemometers are other types in use, but won't be considered in this research. Following this introductory explanation, a deeper elaboration on the characteristics and working principle of cup anemometers will be given. A small notion should be made on the fact that a met mast-mounted anemometer (or other meteorological sensors/instruments) is not the only possible configuration in wind resource assessment. Several experiments and measurement campaigns with nacellemounted anemometers were conducted. Although they can give a more than reasonable estimate of wind characteristics, several studies found that the operating state of the wind turbines (presumably the turbine wake caused by the blade rotation) influenced the readings received from the nacelle-mounted anemometers to a statistically significant extent [87].

Cup anemometer – The cup anemometer is the oldest and most commonly used anemometer in wind energy science and industry. It usually consists of three equally spaced hemispherical and light weight cups, although sometimes versions with four cups are used too. The cups are attached to a centrally rotating vertical axis through spokes. Flowing wind exerts a drag force on the cups, which is given by Equation 2.7,

$$F_d = \frac{1}{2} c_d A \rho U^2 \tag{2.7}$$

where c_d is the drag coefficient, A is the cup area exposed to the wind, ρ is the air density and U is the wind velocity. As the drag coefficient of the concave surface is higher than on the convex surface, cups facing the wind with their concave side experience more drag force, causing the cups to rotate on its vertical axis. Via the anemometer factor, which is different for size and design, the rotational speed is directly proportional to the horizontal wind speed at the site [68]. The current wind speed is directly sensed and recorded, this usually happens in a data logger. The latter serves as storage space for the measured wind speeds and all other meteorological characteristics measured by all sensors on the met mast. It can be accessed via an internet connection or an on-site digital port like USB.

Possibilities and limitations - Cup anemometers are precise and tend to be cost attractive compared to other types of anemometers. The popularity of this type of anemometer is also strongly based on the fact that it can sustain a variety of harsh environments and they can be very robust. Cup anemometers also come with some generic limitations, of which the following three are the most important ones. Firstly, it experiences a non-ideal sensitivity to angle of attacks out of the horizontal plane. This makes them less appropriate for sloping terrain and unable to measure the vertical component of wind. The second problematic aspect of cup anemometers is the dynamic response. They accelerate quickly with the wind but retard much slower as the wind ceases, causing them to give unreliable measurements in wind gusts. These inertial effect are also called "overspeeding". Lastly, non-linearity and variation in calibration of cup anemometers can be caused by mechanical friction or deviant shape of the cups [37].

2.2.2. Remote sensing techniques

Overview - There are two types of commercially available remote sensing devices available on the market for wind resource assessment: SoDAR and LiDAR. Both find their origin in atmospheric research, but especially LiDAR is nowadays used in a wide variety of disciplines like agriculture, geology, autonomous vehicles, archaeology, car speed control, military and space flight. Since around 15 years, both are becoming more and more popular as a supplement to the traditional met mast in wind industry [70]. There are many similarities between both, but the most important difference is that SoDAR uses sound waves and LiDAR uses light waves (or particles, see duality of light). Since this research deals with (the comparison of) cup anemometer and LiDAR data, SoDAR won't be treated further in this section.

For LiDAR devices, again a dichotomy can be made. There are two types of LiDARs in use for wind resource assessment: pulsed and continuous wave (CW) LiDAR. They differ in their emission of light waves; where pulsed LiDARs give short bursts of light, CW LiDARs do emit continuous beams of light [18]. In the remaining of this section, CW LiDARs will extensively be discussed. This is dictated by the fact that all for this research available LiDAR data originates from CW LiDARs, stationed in the Netherlands. It should be noted that throughout this thesis, the term LiDAR is used interchangeably for the device itself as well as for the principle behind it.

Doppler effect – As being said, remote sensing based devices like LiDARs utilize the wave characteristics of light to measure the wind speed and direction. An in-built laser emits beams of light, which are back-scattered by moving molecules and aerosols in the air above the device. This back-scattered light is collected by a detector, after which the Doppler shift of the light frequency is measured. The Doppler shift (or Doppler effect) is defined as the change in frequency or wavelength of a sound or light wave in relation to an observer who is moving relative to the source of the wave [87]. In our situation, the LiDAR device can be seen as the stationary observer. The Doppler shift is therefore simply calculated as the observed difference in frequency of the reference light beam and the back-scattered light beam, as shown in Equation 2.8.

$$\Delta f_{\text{Doppler}} = f_{\text{bs}} - f_{\text{ref}} \tag{2.8}$$

An everyday example of this Doppler effect, is the hearable frequency shift in the sound waves of the sirens of an ambulance passing by in the streets. An important underlying assumption of this working principle is that the concerning particles in the air are so lightweight that their velocity is equal to the velocity of the surrounding air, which is agreed upon in science via extensive research.

Wind speed from LiDAR – During the scattering by the moving particles, typically dust, water droplets, pollution etc. in the wind, the frequency of the light waves changes. Obtaining the Doppler shift in the frequency of the emitted light beams from moving particles in the air is the first step in calculating the wind speed and other wind characteristics at several heights between 10 and 200 m above the LiDAR device. The obtained Doppler shifted frequency is directly proportional to the so-called Line-of-Sight (LOS) velocity according to Equation 2.9, in which $v_{\rm LOS}$ represents the Line-of-Sight velocity, λ_0 is the wavelength of the laser signal and $\Delta f_{\rm Doppler}$ is the Doppler frequency shift [95]. The LOS velocity or radial velocity is the speed of the moving particles along the light beam direction.

$$v_{\rm LOS}(\phi) = \frac{\lambda_0 \Delta f_{\rm Doppler}(\phi)}{2}$$
 (2.9)

Since the line-of-sight velocity obtained by a single measurement is not very useful on its own, LiDAR devices use several beams to determine the LOS velocity in separate points. The light beams emitted by LiDARs form a conical shaped measurement volume. The cone angle θ , usually 60 degrees, is kept constant, where the azimuthal angle ϕ of the beam is varied to measure multiple LOS velocity vectors to construct the wind speed vectors. Figure 2.6 illustrates the set-up of a ground-based LiDAR, indicating several LOS velocities and the conical shaped measurement volume with minimum and maximum height.

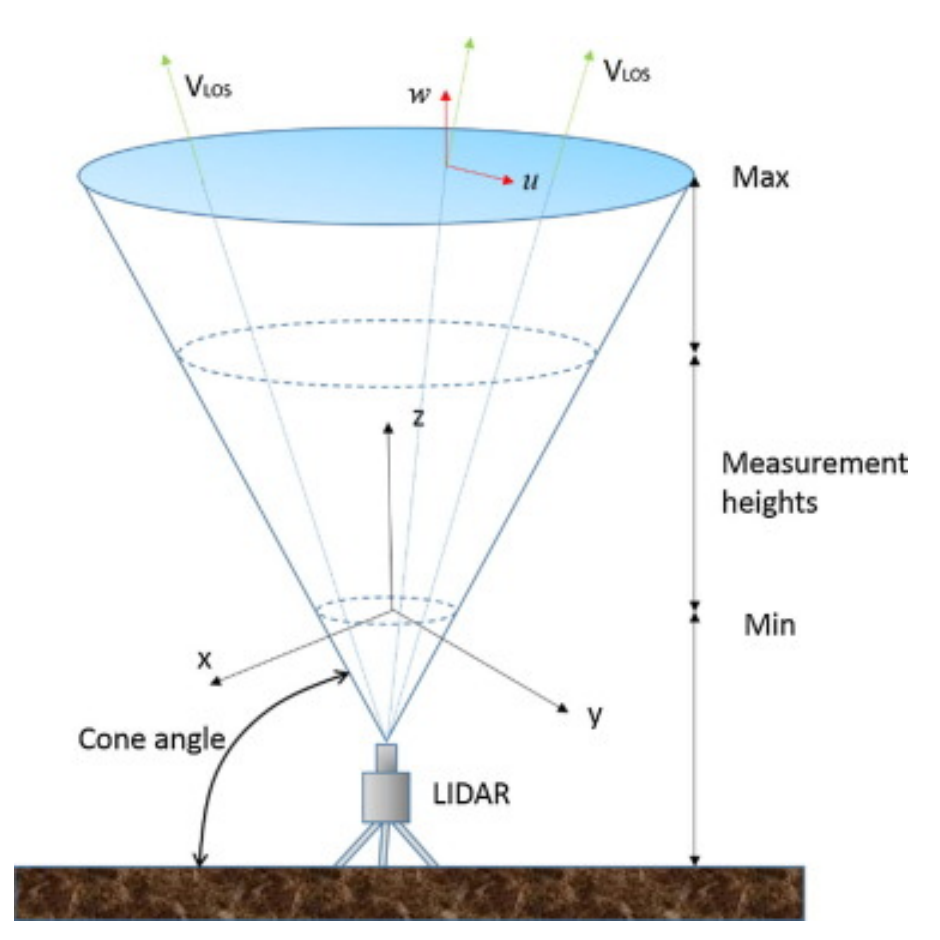


Figure 2.6: LiDAR measurement set-up, indicating the LOS velocity and the conical shaped measurement volume

Under the important assumption of uniform flow, these points can be combined to establish a three-dimensional wind speed vector to estimate the actual wind velocity in the space between those points. Equation 2.10 dictates the relationship between v_{LOS} and several other important variables. Besides the earlier mentioned fixed cone angle θ and the varied azimuth angle ϕ , the three unknown variables of horizontal wind speed U, vertical wind speed W and wind direction ϕ_d in Equation 2.10 can be obtained using a non-linear least squares method applied to the measured data [89].

$$v_{LOS}(\phi) = |U\cos(\phi - \phi_d)\sin(\theta) + W\cos(\theta)|$$
 (2.10)

Characteristics CW LiDARs – As mentioned above, so-called continuous wave (CW) Li-DARs emit continuous beams of light at a fixed elevation focused at a certain height. This measurement height can be changed by adjusting the focal settings of the telescope in the LiDAR. The emitted light beams used in LiDARs are from the infrared part of the spectrum, having a typical wavelength of 1-2 micrometres, and are therefore not dangerous to the human eye. Highly sensitive receivers are used, whereby only one out of every 1012 emitted photons is needed to determine the Doppler shift and the LOS velocity [87].

A measurement limit of 200 to 300 m is common for CW LiDARs, due to the fact that the probe length increases with the square of the height. The probe length of a LiDAR device can be seen as the resolution of its measurements. For CW LiDARs, the probe length varies with height, resulting in a vertical resolution ranging from less than 1 m at 10 m height to around 25 m at 250 m height. The horizontal resolution also decreases with height, since the volume of the measurement disc at higher heights is bigger due to the conical shape of the LiDAR measurement volume [18]. These two factors expose an important limitation of CW LiDARs: a decreasing measurement precision with height and highlight the important difference between volume measurements of LiDARs and point measurements of anemometers.

Advantages - (CW) LiDARs have a wide range of advantages, usually in reference to conventional anemometry like the cup anemometer. One device is able to measure all important wind characteristics at e.g. 10 different heights between 10 and 220 m, making it an highly complete device. LiDARs are easy to install, do not require permits or construction and can be moved when needed due to their lightweight properties. A very important advantages lies in the fact that LiDARs do not interfere with the air flow to be measured. This implies the absence of inertial effects on the measurements (overspeeding problem with anemometers) [95].

Limitations LiDAR measured turbulence - Several generic drawbacks exist too. LiDARs are still quite expensive and ideally have to be installed 2-4 rotor diameters away from wind turbines. This requirement could induce inconsistencies in the measurements applied to the nearby turbines. Next to that, LiDAR devices are not yet able to measure stability related properties in the ABL, since these rely on heat fluxes in the atmosphere. Three other factors dominate the ongoing discussion regarding LiDAR measured turbulence. Firstly, they can suffer from instrument noise. This is mainly due to a limited amount of aerosol scatterers in the probe volume and can cause overestimations of *TI* [80]. However, this happens quite rarely and most LiDARs are equipped with algorithms to deal with this problem.

Secondly and as mentioned earlier, LiDARs make use of volume measurements. The Li-DAR receives back-scattered radiation from an air volume and not from a point. Although averaging over a volume can give several benefits for wind resource assessment, the conversion of these volume measurements to point-based data can lead to inconsistencies, so-called volume or volumetric averaging. The earlier introduced probe length plays an important role in this. What the LiDAR measures at 100 m height is actually a weighted average of the velocities of all aerosols in the volume between 90 and 110 m. Here, the probe volume resembles a low-pass filter [81]. Since this means that particle motion at high frequencies on a spatial scale smaller than the probe volume cannot be resolved, this is important for the judgement of LiDAR measured turbulence.

Thirdly, especially CW LiDARs heavily rely on the assumption of homogeneous flow conditions, which makes them less accurate for rough or sloped terrain. These conditions can also cause problems involving the interference of non-horizontal components of the wind speed with the mean horizontal wind speed. [38]. Most importantly, the above assumption causes a bias known as variance contamination. Most importantly in the light of this research, it happens that changes in the wind in the probe volume introduce additional variance components, causing σ^2 to be overestimated by LiDAR. The above assumption does not prevail for turbulent flow, which is by definition small-scale, and therefore especially applies for turbulence measurements as well. The resulting bias that is often found in LiDAR measured TI is known as variance contamination.

2.3. Statistics for wind resource assessment

Analyzing and especially comparing wind resource data from different sources comes inevitably with some statistical notions and techniques. Subsection 2.3.1 elaborates on uncertainty and how this is quantified in a normal distribution. This includes standard deviation σ , which is important for calculations regarding TI. Regression, which is used to asses the mutual relation of two data sets, is then introduced in Subsection 2.3.2. Finally, Subsection 2.3.3 explains the exact difference in definition between accuracy and precision.

2.3.1. Uncertainty

Gaussian distribution – In statistics, uncertainty is often defined as the lack of certainty about sets of measured physical values or data, e.g. wind speed. The degree of uncertainty can be dependant on a lot of factors and always adds up when multiple sources of uncertainty are brought together in one variable. Usually, there exists a need to quantify this uncertainty and it is therefore strongly related to measures to indicate the spread of the measured value or data. The Gaussian or normal distribution is a very common continuous probability density distribution, often used in natural and other sciences to represent real-valued random variables whose real distributions are unknown [101]. A lot of measurements in this research are assumed to have a Gaussian distribution within the 10-minute interval, which is commonly used in wind resource assessment, and can therefore be called normally distributed. It should be noted that the occurrence of wind speeds *U* naturally follows a Weibull distribution, which is elaborated on in Section 5.1.

Central Limit Theorem – The normal or Gaussian distribution derives its function from the Central Limit Theorem. This theorem states that samples of observations of random variables independently drawn from independent distributions always converge in distribution to the normal. In other words, these random variables become normally distributed when the number of observation is sufficiently high. The Central Limit Theorem specifically applies to physical quantities that are expected to be the sum of many independent processes. Such quantities, like wind speed or TI, often have distributions very close to a Gaussian distribution. This allows statistical tests like ordinary least squares (OLS) linear regression, which will abundantly be used throughout this thesis, to have analytic results in explicit form [101].

Function and parameters – The probability density function of the Gaussian or normal distribution has a bell shaped curve and two parameters. The first one is the arithmetic mean or expectation of the distribution. The mean value μ of a sample x_1, x_2, \ldots, x_N is simply calculated by taking the sum of the sampled values divided by the number of items in the sample N. The second parameter is the standard deviation σ , which is a measure used to quantify the level of variation in a data set. A low standard deviation refers to a situation where most of the data points tend to be close to the mean value of the data set, while a high standard deviation refers to a situation where the data points are more spread out in reference to the arithmetic mean or expectation.

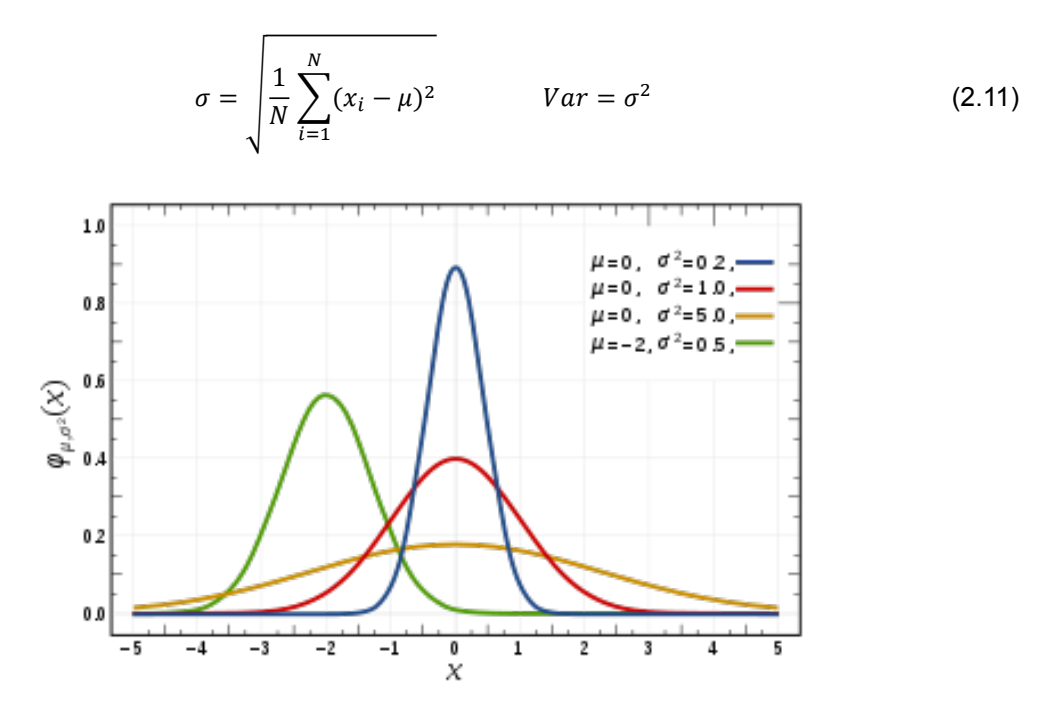


Figure 2.7: Gaussian or normal distribution for different values of μ and σ^2 , indicating population mean and spread [1]

The standard deviation of a data set is calculated by means of Equation 2.11, where N is again the number of data points in the sample, μ is the mean value and x_i is the data point for that i. Another important statistical parameter is the variance, which is simply the square of the standard deviation as stated in Equation 2.11. Figure 2.7 illustrates several Gaussian distribution with different values for μ and σ . It shows a centre around various sample means μ and different levels of variation, indicated by the variance σ^2 .

2.3.2. Regression analysis

Overview – Regression analysis covers a wide range of statistical methods for estimating and quantifying the relationships among variables. In its simplest form it focuses on two variables, but possibilities of including more variables are also present. Regression analysis implies a relationship between a dependent variable and one (or more) independent variables. The dependent variable serves as a criterion variable, whereas the independent variable is seen as a predictor for this dependent variable [106]. More specifically, regression analysis helps one understand how the dependant variable changes when the independent variable is varied. Regarding the comparison of LiDAR and met mast data, the latter can be seen as independent variable. The most logical dichotomy that can be made between all types of regression analysis is the one between linear and non-linear regression. The difference lies in the relationship between both above described variables, which can be linear or non-linear. This thesis focuses on the first type of regression, on which will be elaborated further in this section.

Linear regression – In general, the model specification in linear regression implies that the dependent variable is linearly related to the independent variable. This is illustrated by the formula for linear regression in Equation 2.12, where y is the dependent variable, x is the independent variable, α is the slope and β is the offset [106]. Linear regression has many practical applications, of which most fall into one of the following two categories. Firstly, the goal of linear regression can be prediction or forecasting. The models are then used to fit a predictive function to the observed data set of both dependent and independent variables. After the development of such functions and when additional values of the predictor variable are collected without accompanying responses, they can be used to make a prediction of the response.

Secondly, the goal can be to explain variation in the dependent variable that can be attributed to variation in the independent variable. Since this is the way linear regression will be utilized throughout this thesis, the rest of this section will focus on this type of linear regression.

$$y(x) = \alpha x + \beta \tag{2.12}$$

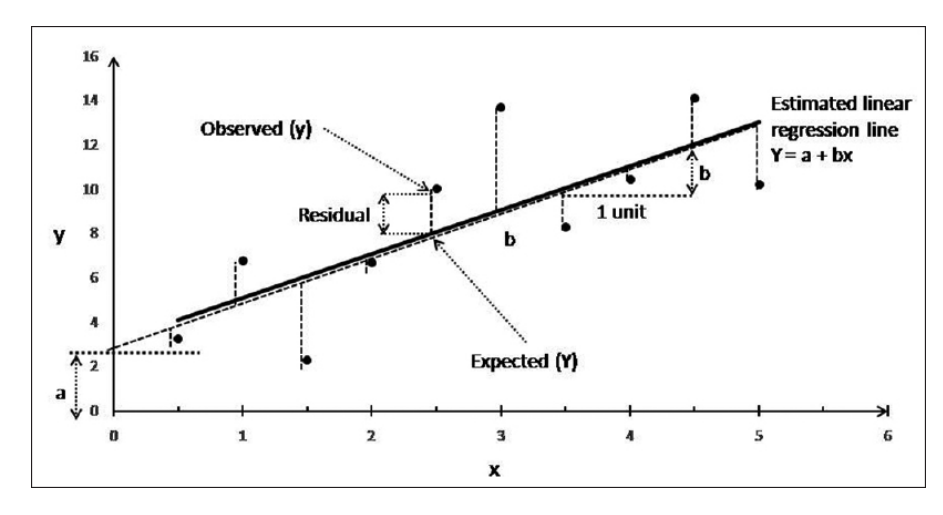


Figure 2.8: The principle of linear regression [15]

Ordinary least squares linear regression – Linear regression models can make use of a whole variety of fits, but they are often fitted using the linear least squares approach. It occurs that there are again several forms of linear least squares estimation approaches, like generalized- and weighted least squares, but that the ordinary least squares (OLS) is by far the most used estimation approach for linear regression, especially in wind resource data analysis. OLS picks the above mentioned parameters α and β of a linear function of the dependent variable by the principle of least squares: it aims to minimize the sum of the squares of the differences between the dependent variable in the given data set and the variable predicted by the linear function [36]. In geometrical terms, this can be seen as the sum of the squared distances, parallel to the axis of the dependent variable, between each data point in the set and the corresponding point on the regression surface. Here applies: the smaller the differences, the better the model fits the data. Figure 2.8 illustrates the above explained principle of OLS, where a line is fitted to a certain data set to minimize the sum of the squares of the differences between the independent variable x and dependent variable y.

Slope and coefficient of determination - In ordinary least squares linear regression, two parameters are of significant importance to assess the following aspects: accuracy of the found linear relationship between both variables and the goodness-of-fit of this relationship. To explain the usefulness of the slope in assessing this accuracy, first another aspect of OLS linear regression should be elucidated. There are two forms of regression that play a role in this thesis: unforced and forced regression. Where the first is basically what is discussed above and follows Equation 2.12, the latter uses the assumption that an offset in the linear regression is absent. Therefore, only the parameter α is to be found. For the purposes in this thesis, the resulting parameter α or the slope of the linear regression approaches the value of 1 for ascending accuracy, which is therefore the target value for α . The second important parameter is the coefficient of determination R^2 and expresses the goodness-of-fit of the found linear relationship between the dependent and independent variable. In other words, it is the proportion of the variance in the dependent variable that is predictable from the independent variable [24]. In the context of this thesis, the coefficient of determination is used to test hypotheses about the goodness-of-fit of LiDAR measured data on met mast measured data.

The coefficient of determination can range from 0 to 1, where 1 serves as the target value. This value implies the best fit of the linear regression on the data in comparison to the use of the arithmetic mean value. This concept is visualized in Figure 2.9, where the red and blue squares represent respectively the denominator and the numerator of the fraction in Equation 2.13, which shows how the coefficient of determination R^2 is calculated.

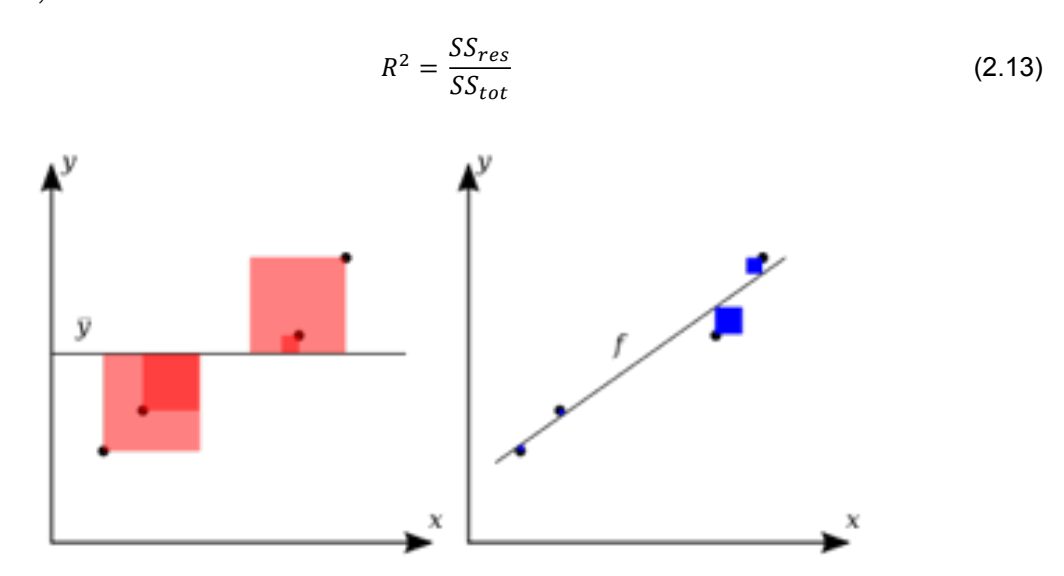


Figure 2.9: The principle of ordinary least squares, used in determining the coefficient of determination R² [5]

2.3.3. Accuracy and precision

Definition – The concepts of accuracy and precision are often mistakenly confused and used interchangeably. However, there is a clear and distinct difference in definition between these two statistical terms. To clarify the use of both in this thesis, both definitions are given as defined by the International Organization for Standardization (ISO). According to ISO 5725-1, 'accuracy' is a term used to describe the closeness of measurements to their true values. Applied to the matter in this thesis, this would e.g. mean that certain LiDAR measurement data has a level of closeness to accompanying anemometer data, which is considered absolute truth in the context of this research. In contrast to that, the term 'precision' can be defined as the degree of closeness of the measurements itself. It can be said that the terms 'accuracy' and 'precision' assess the level of external and internal trueness, respectively [43]. Both concepts are illustrated in Figure 2.10.

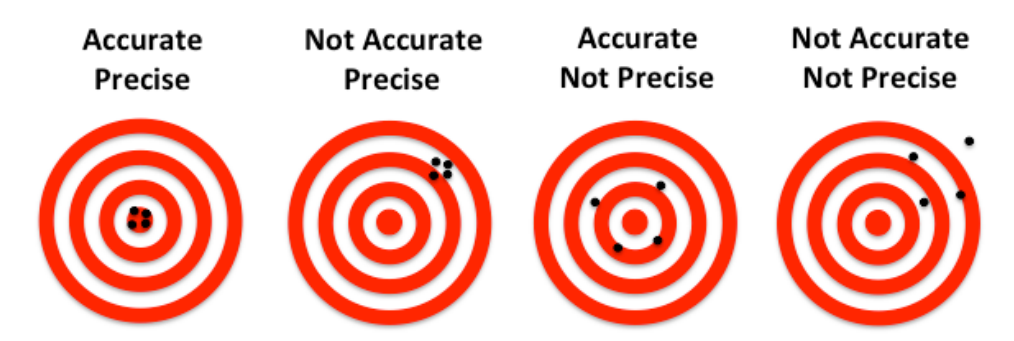


Figure 2.10: Four situations describing the definitions of accuracy and precision [77]

Concerning the above discussed ordinary least squares (OLS) linear regression, both concepts of accuracy and precision can be linked to the two most important outcomes of this statistical test. The slope or parameter α of the OLS linear regression analysis serves as an accuracy indicator, where the R^2 serves as an indicator for precision.

2.3.4. Measure Correlate Predict methodology

Measurement campaigns - To obtain reliable wind data from a certain site, it is usually required to perform long-term measurement campaigns. Most professional campaigns range from at least a full year to 3-5 years. This is inevitably takes a lot of valuable time and the resources needed for measuring itself are also costly, as posed earlier in Section 2.2 on the rising cost of met masts and the costliness of using LiDARs. As a result of these temporal and financial characteristics, wind measurements at wind farm sites are not rarely only available for relatively short periods, ranging from several months to 1 or 2 years. Since these measurements often serve as an input to estimate the energy production of a wind turbine over its whole lifetime, several methods or algorithms are developed to correct for the long term. An overarching term that captures all these methods and algorithms, is the Measure Correlate Predict methodology.

Measure Correlate Predict methodology - The above introduced so called Measure Correlate Predict (MCP) methods or algorithms are often used to predict important wind characteristics at target sites in the long run, based on short-term data from nearby sources [25]. Firstly, a reference site with high quality data for a longer period of time is needed, as well as a target site with data for only a shorter period of time. Thereafter, a correlation between the target site and the reference site should be established. Ultimately, the long-term reference site data and the established correlation can be used to predict the characteristics of the wind at the target site [126]. Figure 2.11 visually explains the concept of the MCP methodology.

Target site (measured) Compared actual to predicted Target site (predicted) Reference site (measured)

Verification of Measure Correlate Predict Methodology

Figure 2.11: Visual conceptualisation of the general idea of the Measure Correlate Predict methodology [126]

Time

Various MCP methods - Several MCP methods are known to establish the correlation between the target site and the reference site. [99] and [126] both give overviews of used MCP methods in literature and together they come to the high number of nine different methods. This includes linear regression, variance ratio, stability difference, Weibull scale, wind direction based, Mortimer, wind index, artificial neural networks (ANN) and support vector regression (SVR). Since the amount of nine techniques is too high to consider all of them, the most frequently used ones are shortly elaborated on below. These are also the ones assessed in this research. It should be noted that the below explanation on MCP methods naturally focuses on wind speed U, while in this research the methods are used for TI.

Linear regression method - The linear regression (LR) MCP method is the most used one throughout other research, mainly because of its simplicity and the general acquaintance with linear regression. It uses linear regression to characterize the relationship between the reference and target site measurements, identically to Equation 2.12 in Subsection 2.3.2. Since linear regression is explained extensively in that section, it won't be discussed further here.

Variance ratio method - The second MCP method that is considered is the variance ratio method (VR). This method was introduced because simple linear regression can lead to an underestimation of the long-term variance of the data. It is suspected that the VR method will lead to better final predictions than the LR method in situations where the R^2 value for the linear regression in the LR method is low. When both LR and VR method are applied to TI data as in Chapter 8, this can certainly be the case and may lead to confusingly disparate obtained linear models. To clarify the sometimes very different results, an example of applying both methods to random data is shown in Appendix A. Equation 2.14 explains the relationship used in this method, in which y and x are the respective wind speeds at the target site and the reference site. Furthermore, μ_x and μ_y are the respective mean wind speeds and σ_x and σ_y are the respective standard deviations at the target site and the reference site.

$$y = \mu_{y} - \frac{\sigma_{y}}{\sigma_{x}} \mu_{x} + \frac{\sigma_{y}}{\sigma_{x}} x \tag{2.14}$$

Mortimer method - Lastly, the Mortimer MCP method is proposed. This is a binning method in which data from both sites are binned by wind direction sector and wind speed at the reference site. Within each bin, the ratios of the target site and the reference site are calculated. This results in a matrix of the average of the calculated ratios and one of the standard deviations of the ratios in each bin. The established relationship between both sites is of the form of Equation 2.15, where r is the average ratio for a certain wind direction sector and wind speed bin and e represent a triangular distributed variable for standard deviation σ of the same bin.

$$y = (r+e)x \tag{2.15}$$

2.4. Loads, moments and stresses on a onshore wind turbine

Structure of modern onshore wind turbines - In the nowadays mature wind industry, most produced and commissioned multi-megawatt onshore wind turbines have a quite similar generic design all around the world. Three-bladed, horizontal-axis wind turbines with conical tubular steel towers and fibre-reinforced plastic blades are considered the standard. This already names the two most important parts of a wind turbine: the supporting tower and the three, usually identical blades. The blades are rooted in the hub of the wind turbine, together forming the so-called rotor of the wind turbine. The hub with its three blade roots is attached to the nacelle, which houses all important generating components of the turbine, namely the gearbox, generator, brake assembly and both high- and low speed shafts. The rotor and nacelle together, also called RNA (Rotor and Nacelle Assembly) are supported by the tower and a foundation both above and in the ground.

Forces or loads on wind turbine components - The wind naturally exerts forces on all parts of the turbine, but due to their big size and shape, the blades and the tower are subject to the most and largest forces. Where the blades are specifically designed to capture as much as wind as possible to increase the energy yield of the turbine, the opposite applies to the tower [110]. The blades are rooted in the hub at joints called the blade roots, a location to which forces on blades naturally converge to. The established wind profile, wind shear and turbulence play a big role in the determination of the resulting loads exerted on the structure [46]. For both rotor and tower, physical models are constructed to calculate these loads.

To calculate the forces on the blades, blade roots and hub of a wind turbine, the by far most used method is the Blade Element Momentum Theory, which is a contraction of the blade element theory and the momentum theory. Without diving into too much detail, this theory uses the fundamental physical law of conservation of momentum on a free stream fluid flow through a actuator disk, representing the rotor plane of a wind turbine, to arrive at an equation to compute the thrust force on the rotor T_R by means of Equation 2.16 [105]. This equation includes well known variables as rotor area A, horizontal wind speed U and air density ρ , as well as the thrust coefficient c_T . The latter is a turbine- and location specific dimensionless coefficient, which follows from the blade geometry and airfoil characteristics.

$$T_{\rm R} = \frac{1}{2} c_{\rm T} \rho A U^2 \tag{2.16}$$

As stated above, another significant part of the aerodynamic loading on a wind turbine are the forces exerted across the length of the supporting tower. These forces are called tower drag and depend heavily on wind shear (see Equation 2.1) [105]. The tower drag F_T is computed via an equation quite similar to the one shown above for the rotor, namely Equation 2.17. The tower diameter is represented by D_T and the tower drag coefficient by c_d , which has to be determined experimentally.

$$F_{\rm T} = \frac{1}{2} c_{\rm d} \rho D_{\rm T} U^2 \tag{2.17}$$

Loads on a wind turbine can be subdivided in seven different categories: static loads which are not associated with rotation, steady loads associated with rotation, cyclic loads due to blade weight or yaw motion, impulsive loads, transient loads due to starting and stopping, resonance induced-loads due to excitations near the structure's natural frequency and stochastic loads due to turbulence [113]. This thesis deals with LiDAR measured turbulence intensity (TI); the focus is therefore on the last type of wind turbine loads: the ones caused by turbulence. The principle of turbulent loads on a wind turbine caused by fluctuating winds is depicted in Figure 2.12.

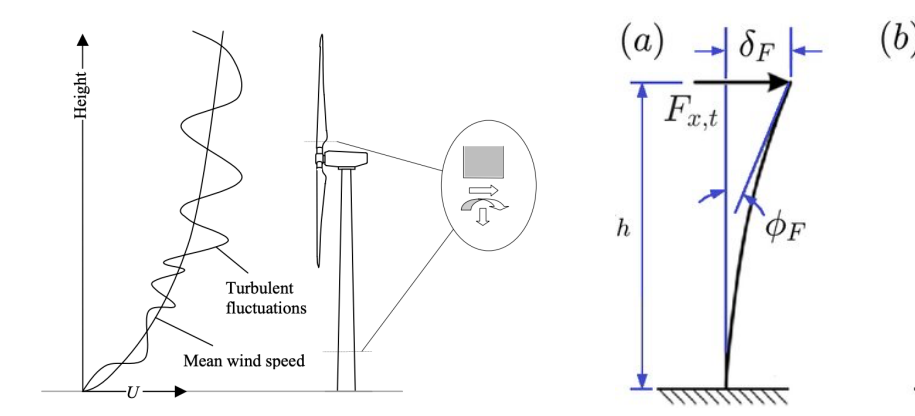


Figure 2.12: Aerodynamic loading on a wind turbine, with wind speed *U* visually decomposed in a mean and fluctuating part [46]

Figure 2.13: Sketch representing a wind turbine tower idealized as a 2D cantilever beam, with indicated forces F and moments M [42]

Cantilever beam model wind turbine - Both tower and blades of a wind turbines can be considered cantilever beams, which are beams that are only clamped on one end [42]. Figure 2.13 contains a schematic representation of such beam for the case of a tower, with height of the tower h and the above discussed force F_T on the left. The latter is expressed by means of $F_{x,t}$ in Figure 2.13 as a function of the x coordinate and time. On the right hand side of Figure 2.13, the bending moment M is obtained with the help of F_T and height h. This is done by means of the famous Equation 2.18, where r expresses the position vector or lever arm. If the obtainment of the bending moment at the top of the tower $M_{towertop}$ is desired, r is equal to h. Several bending moments M can be distinguished, of which two types are introduced here: bending moments (and resulting stresses) over the x-axis and over the y-axis. The x-axis in this frame is defined as the axis perpendicular to the rotor plane of the turbine, whereas the y-axis is the axis parallel to the rotor plane. For the turbine tower, the bending moments over the x-axis and y-axis are called side-to-side and fore-aft bending moment, respectively. For the blades, the expressions edgewise and flapwise bending moment are used.

$$M = rF (2.18) \sigma = \frac{My}{I_x} (2.19)$$

To obtain stresses σ at different nodes along the cantilever beam that can represent the turbine blades or tower, use is made of structural properties depicted in 2.14. The bending moment M caused by the thrust force F_{thrust} on (in the case of this schematic representation) the tower, is obtained with the help of lever arm r, here expressed by h. Two other geometrical aspects of the wind turbine structure are needed to determine σ at the point of the arrow in 2.14: the area moment of inertia I_x and radius of the tower y. Both depend on the geometry of the object under attention and both decrease with increasing height for a wind turbine tower, since the base radius of a tower is greater than its top radius.

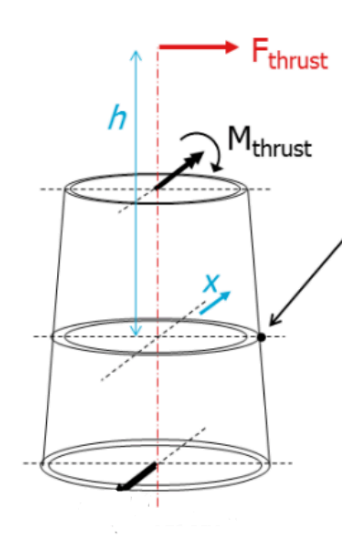


Figure 2.14: Wind turbine tower segment to illustrate determination of stresses at the node indicated by the arrow. A certain bending moment is present caused by an aerodynamic thrust force and a lever arm derived from the cantilever beam model of the wind turbine tower. Together with radius y and area moment of inertia I_x , stresses are calculated by means of Equation 2.19 [125].

Fatigue of wind turbine components - Many materials can withstand a load or stress that is applied once, but they might not survive if that same load or stress is applied numerous times over and over again, forming a cyclic pattern. This inability to withstand loads or stresses applied in a cyclic pattern is called fatigue damage. All components of a wind turbine are made of (composite) materials that sooner or later experience this so-called material fatigue due to the continuous subjection of wind turbines to varying loads [105]. This underlines the importance of fatigue analyses, examining the fatigue properties of e.g. blades and tower, in the design process of wind turbines. Fatigue damage basically starts with the presence of tiny cracks in the material. These tiny cracks can grow further and further under influence of cyclic loading, until the point where the material fails and breaks. In other words, turbulence influences the fatigue of blades, nacelle, hub and tower construction and therefore the lifetime of a turbine. In worst case scenarios, fatigue can even lead to major negative consequences for wind turbines like falling blades, collapsing RNAs or bended towers [86]

As Chapter 5 attempts to judge the accuracy of LiDAR TI measurements, this is potentially a good preliminary research for the influence of turbulence intensity on the fatigue lifetime of wind turbines because it can identify meaningful values for TI. These values can in turn serve as input for a sensitivity analysis assessing the influence of TI on fatigue lifetime in Chapter 6. This research focuses on the fatigue lifetime of a turbine since this factor is of considerable influence on the prediction of the lifetime energy production. The longer a wind turbine is allowed to stay in operation, the better the final lifetime energy yield will be [86]. Since the actual determination of fatigue damage and the lifetime of wind turbine components is incorporated in the working of the MLife software that is used in Chapter 6, this is explained extensively in Subsection 6.1.3.

Literature review

This chapter comprises of a literature review on the subject(s) treated in this thesis. In Section 3.1, the reader is taken through the history and the scientific context around measuring wind characteristics by means of conventional anemometry and the remote sensing based technique of LiDAR. Secondly, section 3.2 treats the present situation concerning the status of LiDAR in wind industry and zooms in on how this applies to the wind characteristic of special attention: turbulence. Section 3.3 elaborates on the effects of turbulence intensity (TI) on the fatigue lifetime of wind turbines. Lastly, in Section 3.4, the use of Measure Correlate Predict (MCP) methods in wind resource assessment is discussed.

3.1. History of wind resource assessment

Historical context cup anemometer - The cup anemometer is without doubt the most common instrument for measuring wind speed and other wind characteristics. Since its invention by the Irish astronomer Thomas Robinson in 1846, the cup anemometer gained enormous trust in science and industry and is, more or less in the same construction and configuration, still used a lot today at airports, construction sites and wind farms, amongst other applications [92]. One of only few and the most important, generally adapted change since then is the number of cups, which was changed from four to three by Canadian meteorologist John Patterson in 1926. Table 3.1 summarizes the reasons for the everlasting use of this relatively simple device in wind resource assessment [68].

Advantages			
Cheap and easy to install Very robust instrument			
High measuring accuracy	Very linear calibration		
Vertical symmetry axis	High temporal resolution		

Table 3.1: Overview advantages cup anemometers

Already before 1930, the three cup anemometer was adopted as a standard for meteorology in the USA and Canada, after which the rest of the world followed not long after that [92]. The behavior of this type of instrument has been widely studied throughout the last 100 years. In the beginning, studies focused on the optimal number of cups, the arm length and cup aerodynamics [75] [102] [49]. Later on, the focus of research shifted more towards the accuracy of wind speed measurements. This included aspects like cup anemometer response in turbulent flow, optimal calibration methods, blockage effects and other kinds of uncertainties [85] [84] [37] [90].

Cup anemometer in wind industry - The above-mentioned shift in focus towards accuracy related subjects was prompted by the rise of modern wind turbines. The rise of a new, nowadays mature industry, led to the inevitable use of cup anemometers for wind resource

24 3. Literature review

assessment in wind energy industry from the 1970s on. For the reasons listed in Table 3.1, the three cup anemometer was a logical choice to be mounted on the earlier discussed meteorological masts installed in the proximity of wind turbines [59]. As visualized in Figure 3.1, turbines did not often reach higher than 50 m until the mid 90s. This enabled met masts with cup anemometers and other instruments mounted on it to easily cover the whole rotor area of the turbine and supply wind researchers with accurate information about the wind at a sufficient number of heights up til tip height. Around that time, research on cup anemometers focused even more on accuracy related topics due to the increasing importance of the preciseness of wind resource assessment. Furthermore, climatic conditions, anemometer aging, classification of anemometers and the impact to the cup's shape came under greater attention [67] [90] [39] [91].

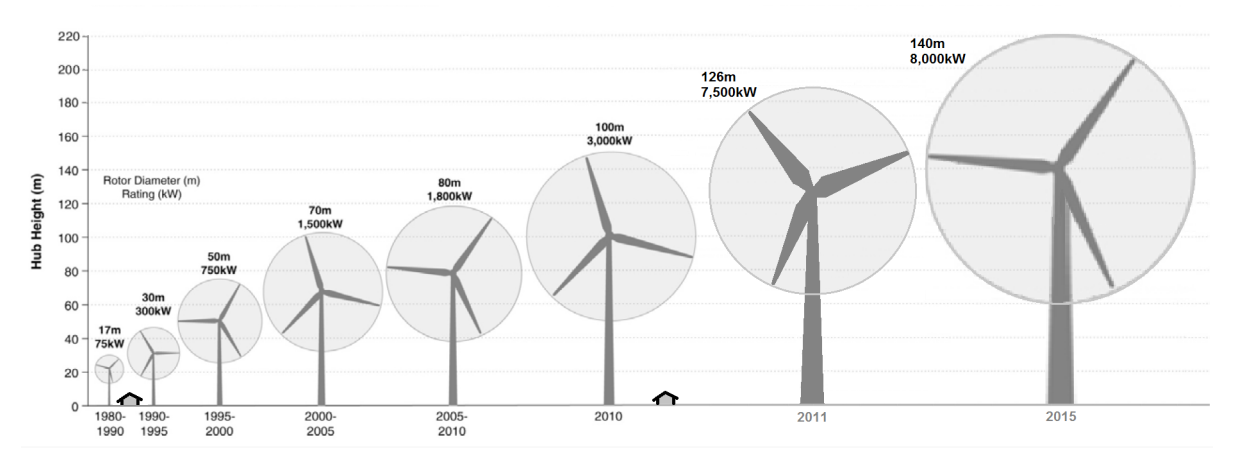


Figure 3.1: The growth of the average size of wind turbines in the period 1980-2015 [14]

The rise of remote sensing techniques in wind industry - Until the early 00s of this century, the conventional cup anemometer was considered as the state-of-the-art and de facto standard in wind industry and science, without serious competitors [38]. Alongside with the rapid increase in height of wind turbines as depicted in Figure 3.1 and the still ongoing quest to higher accuracy, the limitations of met masts became more visible. These developments implied higher costs and increased risk in wind resource assessment due to higher met masts with more anemometers and other instruments mounted on it. Planning impacts, cost and the physical limitations of met masts have resulted in a diverging view to more flexible methods of wind monitoring in stead of blindly continuing to erect masts (far) higher than about 80 to 100 m [38]. The above described developments gave rise to the preliminary research on the use of remote sensing based devices for wind resource assessment [87].

History of remote sensing - Remote sensing (RS) is defined as 'the acquisition of information about an object or phenomenon without making physical contact with the object' and is therefore the opposite of conventional anemometers, which are intrusive in nature: the instruments (can) disturb the air flow they are placed in. Remote sensing finds it origin in the development of flight and comprises of a whole variety of techniques, of which SoDAR and LiDAR are only two [70]. Nevertheless, there will be focused on these two techniques since both are under great attention of wind industry since approximately 2000. For more information, [79] gives a convenient overview of RS techniques and their applications.

The earliest developments of SoDAR and LiDAR were already made between 1950 and 1980, although not being used in wind resource assessment since the wind industry was still in its infancy, as well as both RS techniques [70]. Technological advances in the telecommunication sector over the past decades have paved the way for the commercial development of SoDAR and LiDAR based devices. In the early 00s, they reached a sufficiently high measuring quality to authenticate the growing belief that SoDAR and LiDAR were the way of the future in wind industry. Mainly fibre connected components made both devices more effi-

cient, compact and affordable, which could make them practically usable for wind energy applications [87]. Where SoDAR is considered a more mature and cheaper method, LiDAR is already more accurate and is still getting significantly cheaper and better in the past few years [18]. Since this thesis zooms in on LiDAR measured data, the current position of LiDAR in wind industry and science will be discussed in more detail in the next section.

3.2. Use of LiDAR in wind resource assessment

Entrance of LiDAR in wind energy sector - The discovery of the suitability of the promising LiDAR technique for wind energy applications and the first installation of a LiDAR based device in 2003 marked the start of a new era in wind resource assessment. The first decade of this century can be characterized by a conservative and cautious attitude towards the rise of LiDAR in wind industry [95]. Logically, trust and firmness on the utilization of LiDAR should be gained first before the technique could take its place in industry and science. This trust of the wind industry is mainly dictated by the standards set by the International Electrotechnical Commission (IEC).

Increasing scientific research concerning LiDAR - To expand existing knowledge about LiDAR and gain more support for the use of LiDAR in wind industry, it increasingly became subject of research in the period 2000-2012. The research in this period mainly focused on the two most important parameters in wind resource assessment: mean wind speed and wind direction. Various circumstances and setups have been used to study the accuracy of LiDAR. The most common way is to study the correlation of LiDAR devices with an IEC compliant met-mast, placed within 2-4 diameters from each other. Although it is unfeasible to give a complete overview, some results of such studies are listed below. It should be noted that there is also an extensive list of other research configurations: studies with SoDAR devices, studies with other than cup anemometers, floating LiDAR devices, nacelle-mounted LiDARs, comparisons between pulsed wave and continuous wave LiDARs and more. These are not considered in the list below.

- "On the study of wind energy at great heights using remote sensing techniques" [55] reported an R^2 of 0.97 and slope parameter α of 0.96 for mean wind speed U comparison and finds LiDAR observations of U specially accurate.
- "Offshore wind profiling using LiDAR measurements" [89] finds several slopes α close to unity (>0.99, with small offsets though) and R^2 values between 0.97 and 0.98. It states that continuous wave ZX LiDARs (former ZephIR, the device used in this research) could be a useful tool for wind resource evaluation once the system reliability is improved.
- "Analysis of inflow parameters using lidars" [54] determined a high R^2 of 0.994. Concluding, the wind direction and mean wind speed measured by LiDAR at different heights correlated very well with cup anemometers.
- "Wind Lidar Evaluation at the Danish Wind Test Site in Høvsøre" [109] demonstrates a high level of agreement between LiDAR and calibrated cup, with slopes of 1.00 and R^2 values of around 0.98 for mean wind speed. Wind direction detection is excellent.
- "LiDAR and SoDAR measurements of wind speed and direction in upland terrain for wind energy purposes" [70] come up with LiDAR-cup regression slopes of approximately 0.97, which compare well with slopes of better than 0.99 in similar studies carried out in flat terrain.

Research like the few listed above and the resulting increased familiarity with and accuracy of LiDAR devices finally resulted in an update of the IEC standards in 2017. The new IEC 61400-12-1:2017 standard delivers the technical basis for the acceptance of LiDAR measurements for wind resource assessment. It formally allows the use of LiDAR as a supplementary or alternative measurement technique to mast-mounted cup anemometers for measuring horizontal wind speed and wind direction in flat terrain only.

26 3. Literature review

Increasing attention for LiDAR measured turbulence intensity - The extensive research in the first decade of this century resulted in much progress on the topic of LiDAR devices and measurements. The past 10 years showed a partial shift in attention of LiDAR research towards another wind parameter: turbulence intensity (TI). Since the standard deviation σ_u measured by LiDAR resolves only the turbulence structures larger than a length scale which depends on the circle diameter of the measurement cone and the mean wind speed, the spatial averaging of the volume measurements of CW LiDARs inherently imposes a difference with cup anemometers, as introduced in Subsection 2.2.2 [122]. This explains in short the most important reason why LiDARs are not yet fully trusted for measuring TI (also according the dictating IEC standards) and illustrates why research on LiDAR measured TI increased in the past 10 years.

Almost all research of the past years concerning CW LiDARs measuring turbulence intensity has the common goal of in some way increasing the accuracy and precision of the CW LiDAR devices or investigating the exact progress of this accuracy and precision. The first includes studies on resolving spatial averaging, post-processing LiDAR measurement data, volumetric filtering, improving inner algorithms of CW LiDAR devices, decreasing probe length and more. The latter is mostly done by measurements campaign studies, which show increasingly higher accuracy and precision over the years. Nevertheless, values of slope parameter α and coefficient of determination R^2 do not consistently come close to the desired unity (1.000). Below, a naturally incomplete list presents some studies and their results on comparing LiDAR measured TI with conventional anemometry. Figure 3.2 visualizes a typical outcome of such analysis, comparing LiDAR measured TI with cup anemometer measured TI [81].

- "Evaluation of turbulence measurement techniques from a single Doppler LiDAR" [26] finds low values for R^2 and α of respectively 0.58 and 0.86.
- "LiDAR turbulence measurements for wind turbine selection studies: design turbulence" [23] assessed the σ_u , finding an R^2 of 0.878 and an α of 1.019 and conclude that using the LiDAR TI measurements will not move turbine selection into another classification band unless the results are already at the boundary of the class.
- "Investigation of turbulence measurements with a continuous wave, conically scanning LiDAR" [122] give an example measurement which results in an acceptable R^2 of 0.756 and an α of 0.824.

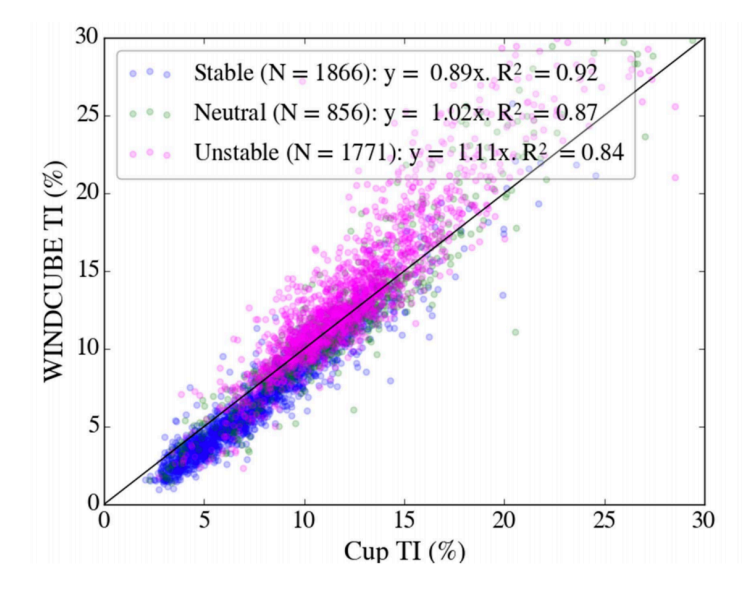


Figure 3.2: Typical example of the results of a forced OLS regression for comparing LiDAR and cup anemometer TI measurements in the three ABL stability regions, indicating data set size, slope parameter α and coefficient of determination R^2 [81]. Note that the TI is given in percentages here, where throughout this thesis TI is given in absolute terms.

- "Can LiDARs measure turbulence? Comparison Between ZephIR 300 and an IEC Compliant Anemometer Mast" [22] tries to answer their own question by stating that the maximum variation between CW LiDAR and met mast mean TI values of less than 15% are observed. Due to big data sets, they achieved values of α ranging from 1.03 1.09 and R^2 values of around 0.80.
- "Can wind LiDARs measure turbulence?" [104] arrives on a promising R^2 of 0.982 and an α of 0.992. However, they answer their main question negatively since they consider the measurements not precise enough.

From the above list and other research can be concluded that this exact research direction has not truly outgrown its infancy. Results are not very consistent, extensive and studies from the past years are often not addressing all kinds of terrain or detailed fundamental limitations of LiDAR TI measurements. This allows this thesis to focus on TI measurements of ZX 300 (formerly ZephIR) continuous wave LiDAR devices at Dutch onshore sites. By comparing such data with nearby met masts, an attempt is made to identify and quantify factors that cause deviations in LiDAR measured TI data compared to neighboring met masts, which can be useful in wind resource assessment in the Netherlands.

3.3. Effects of turbulence on fatigue lifetime

Wind turbine loading and fatigue - The loads and stresses on wind turbines is a scientific topic that is extensively researched ever since the rise of modern wind turbines in the 1970s, it is said to be one of the most important subjects in wind engineering. Without proper understanding of the effects of loads and stresses on a turbine, parts of it might suffer from damage of even failure [104]. The thrust forces of the wind, the gravitational forces and the centrifugal forces acting on several relevant and less relevant parts of a wind turbine are known to cause fatigue damage over the lifetime of wind turbines, as a consequence of two characteristics of modern wind turbines. They are exposed to an enormous amount of load cycles during their lifetime and the variability of these exposures is high due to the stochastic nature of the wind. However, there are also some regular components in fatigue loading [73].

Research on turbulence induced fatigue damage - Accordingly, the variable nature of the wind is an important origin of fatigue damage. This variability is also called turbulence, as extensively elaborated on in Subsection 2.1.2. The qualitative effect of the presence of turbulence in the wind that is loading on wind turbines to cause fatigue lifetime damage is a generally accepted theory, stated and confirmed by many research like [69], [113] and [46]. This is logical taking the rainflow cycle algorithm by Miner and Palmgren for determining fatigue lifetime damage into account, where load cycles are binned by size and added up (See 6.1.3). Since turbulence intensity TI is the widespread used quantitative indicator for turbulence, this factor is often used in research on the quantitative effects of turbulence on fatigue lifetime of wind turbines. In [60] four far apart values for TI are taken in an aeroelastic simulation study, where obviously severe effects by turbulent loading on fatigue lifetime are found. These effects are equally present at the blades and at the turbine tower. With turbulence intensity values of 0.01, 0.1, 0.25 and 0.5, this study is limiting itself to non-realistic differences in turbulence. Another study narrows itself down to a high and low turbulence level, i.e. TI = 0.15 and 0.18. However, a significant higher lifetime for the composite turbine blades is found for the low turbulence level in this research [72]. The results of a recent study on the turbulence added by wakes are also affirmative to the above, although wake added turbulence cannot be compared one to one to regular turbulence [30].

To conclude, the qualitative effect of turbulence on the fatigue lifetime of wind turbines is evident and is taken as given. This effect can be translated to the quantitative turbulence indicator TI too. This has been done by some others, but never in the way it is proposed here. This study touches upon possibly relevant and real-life differences in turbulence intensity and their effects on the fatigue lifetime damage of wind turbine blades and tower.

28 3. Literature review

3.4. Measure Correlate Predict

Use of Measure Correlate Predict in wind resource assessment - Plenty of examples exist of studies that assess the different methods of the Measure Correlate Predict methodology as introduced in Subsection 2.3.4, but they all focus on horizontal wind speed. Throughout the past 15 years, new and hybrid MCP methods or algorithms for the long-term prospection of wind resource have been proposed and tested along different statistical metrics [100] [25] [99] [115] [126]. This thesis aims to apply some of the most common MCP methods on TI data and assess their accuracy and workability by comparing mutual results. As stated in Subsection 2.3.4, more than 10 different methods or algorithms are used throughout research, but again this part will focus on the three most known and used methods: the linear regression method, the variance ratio method and the Mortimer method.

Different methods judged - The linear regression (LR) method is the method most used throughout research and industry in general, mainly because of its simplicity and the general acquaintance with linear regression. At least three possibly important conclusions were drawn in earlier research on this method [100] [99]. Firstly, 8 months of target site time-series data are considered the minimum length to minimize uncertainties in the results. Next to that it is suggested to exclude that part of the data with wind speeds lower than 4 m/s when determining the correlation. This is mainly because wind vane behavior can be erratic at low wind speeds and wind turbines do not operate at these wind speeds. However, other sources say the latter approach resulted in incorrect estimates [115]. Thirdly, the results of the linear regression method can suffer from some inherent characteristics of linear regression: it will always give predictions with smaller variance compared to the observations on which the predictions are based and it goes with a sensitivity towards outliers when estimating the regression parameters.

The second MCP method that is considered is the variance ratio (VR) method. This method was introduced because simple linear regression can lead to an underestimation of the long-term variance of the data, as stated above. This method is considered to better predict standard deviations σ than the linear regression method [100]. Furthermore, it is praised for the facts that it gives such good predictions only having two input parameters and it can be implemented very easily [99].

Lastly, the Mortimer method is proposed. This is a binning method in which data from both sites are binned by wind direction sector and wind speed at the reference site. Within each bin, the ratios of the target site and the reference site are calculated. This results in a matrix of the average of the calculated ratios and one of the standard deviations of the ratios in each bin. For the Mortimer method, it was suggested that it predicts extreme wind speeds better than via the linear regression method and that it gives reliable results compared to both other methods mentioned above [99]. [25] states that according to his findings, the Mortimer method gives consequently better results than linear regression does.

Use of MCP methodology on TI data - Hardly any examples of research into the applicability of Measure Correlate Predict methodology on turbulence intensity TI nor into the comparison of results of the several methods can be found in literature. Only one researcher developed a method based on a multiple correlation analysis, which utilizes a newly developed joint probability distribution function [32]. This function is derived from wind speed, wind direction and turbulence intensity data from two sites. By validation using other met masts, the algorithm showed to estimate the "per sector" and "per speed" long-term TI distribution quite well. In another paper of the same author, a validation test of this algorithm is presented. Among other things, it demonstrated that monthly variation in TI tend to affect the accuracy of the MCP outcome than the yearly variations [33]. Nevertheless, the algorithm performs well in general, with little errors in the results. The approach taken in Chapter 8 is more simple than the above algorithm, which justifies the application of it in this thesis.

4

Research Setup

This chapter gives an overview of the research setup of this thesis, which is divided in two parts. Section 4.1 elaborates on the research objectives mentioned in Chapter 1 and forms the framework of this thesis. Since this research is at least partly based on a measurement campaign, the sites where this campaign is conducted are explained in detail in Section 4.2. This includes a geographical description of the site and local weather conditions, as well as an elaboration on both used instruments: the continuous wave (CW) ZX300 LiDAR devices and cup anemometers.

4.1. Research objectives

Based on the literature review in Chapter 3, three research objectives have been defined. They were already stated in Chapter 1 and are briefly worked out below, mentioning methodological aspects, goals and indicators.

Research objective 1: Assess statistical accuracy and factors influencing this accuracy of ZX 300 Continuous Wave LiDARs at Dutch onshore wind sites by comparing them with proximate met masts, with a special focus on turbulence (TI).

A measurement campaign commissioned by Vattenfall has been conducted from September 2018 till present. This campaign comprises of the deployment of 2 pairs of instruments, both pairs consisting of a ZX 300 CW LiDAR and a met mast with accompanying sensors and anemometers. In the first place, the campaign is performed to assess all wind characteristics important for the future wind farm "Windplan Blauw" at this site. Secondly, the accuracy and precision of LiDAR data compared to the nearby met masts measurements is of interest.

A study into the correlation of the measurements of several wind characteristics of a LiDAR compared to an IEC compliant met mast is conducted. Amongst others, mean horizontal wind speed and wind direction will be treated, but the emphasis is on turbulence intensity (TI). The accuracy and precision are determined by applying ordinary least squares linear regression fits to the scattered measurements of both devices. Ideally, values for the coefficient of determination R^2 close to 1.000 are obtained, as well as a fit as close as possible to y=x.

Additionally, an attempt will be made in identifying factors or scenarios which are possibly influencing the accuracy or precision of ZX 300 CW LiDAR TI data. One can think of, among other factors, height, wind speed, wind direction and internal functioning of the LiDAR device.

Research objective 2: Assess sensitivity of the fatigue lifetime of a commonly used wind turbine at Dutch onshore wind sites as a function of TI to quantify the effect of TI on fatigue.

30 4. Research Setup

Chapter 5 assesses the accuracy of LiDAR TI measurements as discussed under Research objective 1. The outcome of that part of this research is used to serve as an input for a sensitivity analysis of the quantitative effect of turbulence intensity on the fatigue lifetime of a wind turbine relatively similar to ones that are commonly used at Dutch onshore wind sites. Deviations around a mean value for TI μ_{TI} of e.g. $\mu_{\text{TI}} + \sigma$, μ_{TI} itself and $\mu_{\text{TI}} - \sigma$ are adopted and used to create different wind fields by means of TurbSim software, of which an accountability and explanation is provided by the National Renewable Energy Laboratory (NREL) [4].

The TI differentiated wind fields that are simulated serve in turn as input for FAST, a software package also developed by NREL and of which more information can be found here [3], which is commonly used for aeroelastic simulations of horizontal axis wind turbines (HAWT). In FAST, several time series of loads on the wind turbine are generated. This results in forces F per μ_{TI} for several relevant parts of the wind turbine, like blade root and tower base.

The ultimate goal is to calculate the damage equivalent loads and time until failure for different mean values of TI to evaluate the sensitivity of the turbine fatigue lifetime for these different values of $\mu_{\rm TI}$. This is again done with the help of the FAST software package, which gives the possibility to estimate the fatigue lifetime of wind turbines. The code that is used for this encompasses the Palmgren-Miner rule and the rain flow counting technique, which are commonly used to perform such fatigue lifetime calculations.

Research objective 3: Use Measure Correlate Predict (MCP) to extrapolate short-term LiDAR TI data (in reference to long-term met mast data) to investigate possibilities of shortening LiDAR measurement campaigns and identify most accurate and workable MCP method by comparing mutual results.

Data from the earlier introduced measurement campaign can also be used for the attempt to achieve the third research objective. Since time and money are valuable, as short as possible measurement campaigns are desired. MCP has proven to be a possibly valuable method to obtain reliable long-term data for a target site as input for lifetime energy predictions, solely based on short-term data of the target site. This is done with the help of an established relationship between available long-term data from a reference site and the short-term data from the target site. The long-term reference data comprises of TI data over a period of one year, taken from cup anemometer measurements. The short-term target data originates from a nearby LiDAR and covers a period of three to six months.

Three MCP methods to find a relationship between both sites were extracted from literature and proposed in Section 3.4: the linear regression method, the variance ratio method and the Mortimer method. The three methods will be compared based on three statistical criteria. These criteria include normalised versions of the mean μ , standard deviation σ and chi-squared χ^2 . For validation purposes, the results for all MCP methods are compared with the also available long term LiDAR TI data. All the above essentially tries to answer the question whether it is possible to gain accurate long-term TI data from a relatively short LiDAR measurement campaign. Next to that, it will be assessed to what extent the length of such short LiDAR measurement campaigns influences the aforementioned statistical criteria and whether the picked season(s) affects these.

4.2. Site description

Wind farm "Windplan Blauw" - The wind data used in this research are retrieved from two measurement sites, both located within the same wind farm. This is wind farm "Windplan Blauw", formerly known as "IJsselmeerdijk", which is a wind farm planned to be commissioned in 2020 and is spread over the municipalities of Dronten and Lelystad in the north of the province of Flevoland. In 2020, 61 new 4 MW turbines will be installed at this site, replacing the current 74 old wind turbines at the same location. Figure 4.1 depicts in blue the location of wind farm "Windplan Blauw". For more info on the wind farm, see [8] and [6].

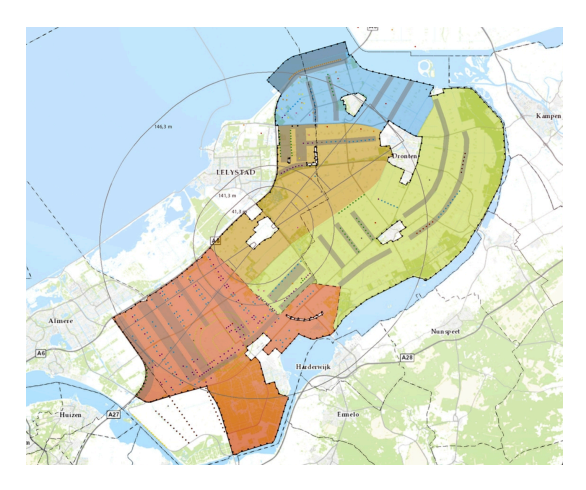




Figure 4.1: Windplan Blauw in northern Flevoland [8]

Figure 4.2: Detailed map of the future wind farm, with LiDARs (orange dots) and met masts (yellow triangles)

LiDAR-met mast pairs - Both measurement sites within the wind farm consist of a LiDAR-met mast pair, which are in close proximity of each other. The location of both LiDARs and met masts are shown in Figure 4.2, where the orange dots and yellow triangles indicate the LiDARs and met masts, respectively. Both LiDARs are identical. Table 4.1 summarizes the specifications of the LiDAR device used in this research, whereas Table 4.3 gives an overview of all instruments mounted on the met masts. The LiDAR also has an inbuilt weather station for ground level measurements, which is not considered in this research.

Name	ZX 300 CW LiDAR
Size	0.9 x 0.9 x 1 m
Weight	55 kg
Power	12 V, 69 W
Range	10 - 220 m
Probe length	±7.7 m at 100 m
Sampling rate	50 Hz
Averaging rate	1 sec & 10 min

Table 4.1: ZX 300 CW LiDAR specifications [9]



Figure 4.3: ZX 300 CW LiDAR device [9]

ZX 300 LiDARs - The ZX 300 continuous wave (CW) onshore wind LiDAR, shown in Figure 4.3, is a state-of-the-art product of the British company ZX Lidars, which launched the first commercially available LiDAR for wind resource assessment in 2004 [9]. This type of LiDAR measures the following quantities at a maximum of 10 heights: packets in average, wind direction, horizontal wind speed U_{hor} , maximum U_{hor} , minimum U_{hor} , vertical wind speed U_{ver} and turbulence intensity TI. Measurement heights of the ZX 300 LiDAR are adjustable, but both LiDAR devices are set to a fixed number of heights, which are listed in Table 4.2. The height of the device itself is 1 m, which is included in the measuring heights. The device averages all the above variables over every 10 minutes, but the 1 second data can also be retrieved for a limited period of time.

Measurement heights [m]			
ZX 300 LiDAR 1 (ZP583)	220, 200, 180, 160, 155, 140, 120, 100, 80, 50, 39		
ZX 300 LiDAR 2 (DM509)	250, 220, 200, 180, 160, 140, 120, 110, 100, 80, 39		

Table 4.2: Different measurement heights of both LiDAR devices

32 4. Research Setup

Meteorological masts - Both met masts were erected in November 2018 and were put into use not long after that. Met mast 1 is 160 m high and met mast 2 is 120 m high. Several instruments are mounted at different heights of the met masts, measuring various quantities. Table 4.3 gives an overview of these instruments, their mounted heights and the quantities they measure. It should be noted that all cup anemometers are mounted twice at the indicated heights, resulting in 10 cup anemometers at met mast 1 and 8 cup anemometers at met mast 2. The measuring frequency f is 1 Hz, where after the 600 measures in a 10-minute interval are averaged over every 10 minutes. As can be observed, the turbulence intensity is not evaluated itself by the instruments, so it should be calculated subsequently by means of Equation 2.6.

Instrument	Heights Mast 1 [m]	Heights Mast 2 [m]	Measurement variables
Cup anemometer	160, 150, 140, 130, 100	120, 110, 100, 50	\overline{U} , U_{min} , U_{max} , σ_{u}
Wind vane	156, 136, 97	114, 90, 70	$\phi_{\sf d}$, $\sigma_{m{\phi}}$
Hygrometer	155, 10	115.5, 10	$q_{\text{avg}}, q_{\text{min}}, q_{\text{max}}, \sigma_{\text{q}}$
Thermometer	155, 10	115.5, 10	T_{avg} , T_{min} , T_{max} , σ_{T}
Barometer	155, 10	115.5, 10	$p_{avg}, p_{min}, p_{max}, \sigma_{p}$

Table 4.3: Specifications of the met masts at wind farm "Windplan Blauw"

Measurement campaign - Both LiDAR met mast pairs have three overlapping measurement heights. Only these heights can be taken into consideration in this research. For LiDAR 1 and met mast 1 these heights are 160, 140 and 100 m and for LiDAR 2 and met mast 2 the heights 120, 110 and 100 m are considered. The measurements from LiDAR 2 at 110 m are discarded in this research, since the height interval would be too narrow otherwise. Table 4.4 provides an overview of the measurement campaign that was conducted for this research at the two sites on the future location of wind farm "Windplan Blauw". Note that Table 4.4 applies to Chapter 5 and that the measurement period used in Chapters 7 and 8 is exactly 1 year (2019).

Instrumentation	Measurement period
Meteorological mast 1	14-12-2018 to 25-06-2019
Meteorological mast 2	14-12-2018 to 25-06-2019
LiDAR 1	14-12-2018 to 25-06-2019
LiDAR 2	14-12-2018 to 25-06-2019

Table 4.4: Overview of conducted measurement campaigns

Intrinsic precision of LiDARs against met mast - When assessing the accuracy and precision of LiDAR measurements compared to met masts, the intrinsic precision of this comparison as described by the manufacturer should be noted upon. ZX LiDARs provides an extensive document addressing a performance verification against a tall met mast. It should be noted that this is done at the following heights: 21, 46, 71 and 92 m and with even more extensive data filtering. The criteria for the linear regression comparison of U were as followed: $R^2 > 0.970$ and slope parameter α in the range of 1.00 ± 2.0%. The ZX 300 LiDAR met both criteria at all four heights and passed the test. Furthermore, a wind direction test was set up, albeit only wind speeds of U < 5 m/s were considered. The ZX 300 LiDAR also passed this test, since it met the only criterion of a direction error < 0.5°. Unfortunately, no tests were held regarding turbulence intensity or at heights of 100 m and higher.

Obstacles around instrumentation - Obstacles and structures surrounding one or more of the met masts or LiDARs, e.g. wind turbines, dykes, buildings or high trees, can potentially distort the incoming wind flow and cause variations in the wind shear at the sites, as explained in Subsection 2.1.1 [87]. An obstacle or structure of 15-20 meters height at a distance of 200-300 meters can already disturb the cup anemometer or LiDAR measurements at the lower heights (e.g. at 39 and 50 m).

4.2. Site description 33

Disturbance effects like the above should be taken into account since they can influence the reliability and therefore usability of wind measurements. For this reason, data exclusion should be performed to make sure unreliable wind sectors are excluded. A detailed description of the measurement sites is prepared and suitable wind direction sectors are defined.

For both measurement sites in wind farm "Windplan Blauw", relevant wind sectors are selected based on a geographical analysis of obstacles surrounding both LiDAR met mast pairs. For LiDAR 2 and met mast 2, this was rather simple. Within a radius of 1 km, no significant obstacles are in place, making all wind sectors suitable for analysis. In proximity of LiDAR 1 and met mast 1, more obstacles are observed within a 300 m to 1 km radius. Since the lowest measurement height of interest for LiDAR met mast pair 1 is 100 m, it is assumed these obstacles do not significantly disturb the measured air flow. The above results in relevant wind sectors of 360° for both locations in the wind farm. Figure 4.4 shows how the wind direction is distributed according to the measurement data of met mast 1 at 160 m height.

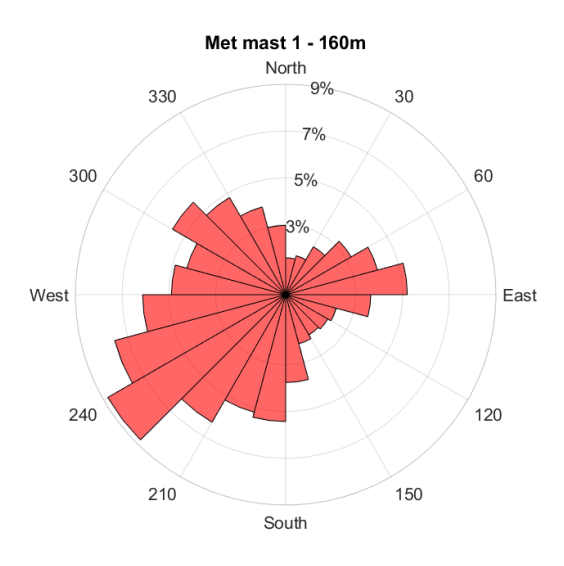


Figure 4.4: Wind rose retrieved from measurement data of met mast 1

Wind turbines "Windplan Blauw" - The current 74 wind turbines at the location of future wind farm "Windplan Blauw", which are all spread and not neatly aligned, will be decommissioned in 2020 and give way to 61 modern wind turbines, of which their location is indicated by the white and red dots in Figure 4.2. The new wind turbines will be operational and deliver energy at the beginning of 2021 and are planned to have a nominal power of 4 MW each. This will ultimately result in almost 250 MW of installed wind power at "Windplan Blauw" and will give an yearly energy yield equal to the needs of 400,000 households. It is not yet known which exact types of wind turbines will be placed, but a maximum tip height is set at 213 m for the wind turbines around LiDAR met mast pair 1 and at 248 m for the wind turbines around LiDAR met mast pair 2. This will mean the hub heights for location 1 and 2 will be around 130 m and 160 m, respectively.

Comparison of LiDAR and met mast

As elaborated on extensively in Chapters 2 and 3, LiDARs and cup anemometers and their measurements are inherently different from each other in measuring principle and therefore partly in their utilization in today's wind industry and science. Where the volume measurements of the relative newcomer LiDAR are more and more seen as reliable and therefore useful, the point measurements of trusted veteran cup anemometer are considered as standard and serve as a benchmark for other competitors like LiDAR.

In this chapter LiDAR measured data from the site introduced in Chapter 4 is compared with measurements from nearby met masts. As stated in Section 1.4, the goal of this comparison is to assess the accuracy of LiDAR measured data, focusing on turbulence, and to identify possible factors influencing this accuracy. Section 5.1 gives an overview of the methods on which this comparison is based, highlighting the metrics of comparison for both data sets. The results in Section 5.2, are subdivided in a basic part containing comparisons of horizontal wind speed $U_{\rm hor}$ and wind direction $\phi_{\rm d}$ and a main part containing comparisons of turbulence intensity TI measures originating from both devices. Final Section 5.3 consists of a discussion of the results with accompanying conclusions.

5.1. Method

Data treatment - The wind data originating from both sources at both sites in the "Windplan Blauw" wind farm are compared at different points. Wind direction ϕ_d , horizontal wind speed $U_{\rm hor}$, standard deviation $\sigma_{\rm u}$ and turbulence intensity TI measured by both cup anemometers and ZX 300 LiDAR devices are of main interest in this research. Before analysis, a pretreatment of the available data is performed. This is done taking the following requirements into account, as prescribed by the International Electrotechnical Commission (IEC) and the producer of the ZX 300 LiDAR devices:

- Relevant wind sectors are chosen. Obstacles and structures surrounding met masts or LiDAR devices can disturb the air flow in which measurements take place. Only wind sectors where the wind can flow freely and without distortions are considered, as explained in Section 4.2.
- A calm filter of U < 3 m/s is applied to the data sets derived from both devices. Because data representing low wind speeds is more prone to errors and offsets and it is of little consequence for wind industry, it is better to exclude this data from analysis.
- Daily LiDAR and weekly met mast files are concatenated to one long period, so two equally long and simultaneous arrays are created without time offset.
- The ordinary least-squares linear regression is performed in the unforced variant. In this way, the fit parameters are subject to a smaller error than when the intercept is forcibly fixed.

Metrics of comparison - Several visualisation techniques and performance metrics are used throughout this chapter. Most of these statistical notions were already deepened to complete extent in Subsection 2.3 and others are more wind resource assessment specific and introduced here.

- **Time series and bias** ϵ Time series are a pure visual manner of presenting data and the difference between the means of LiDAR and cup anemometer measured data is called the bias ϵ .
- **Standard deviation** σ The earlier extensively discussed standard deviation gives an indication of the spread of the data measured by both devices.
- **Histogram** Histograms are used to visualise the distribution of numerical data, which are binned and put in order of occurrence. This data are then plotted against the probability or frequency of occurrence. Data on the occurrence of horizontal wind speeds always approximates a Weibull distribution and lends itself very well to the use of histograms. A Weibull distribution is epitomized by the scale parameter *a* and shape parameter *k*, which are introduced in Equation 5.1.
- **Wind rose** A wind rose is a time honored method which graphically presents the wind direction (and wind speed in more advanced versions) over a period of time at a specific location. The measured data is typically sorted into twelve equal arc segments of 30° and then plotted in a polar graph in which the radius of a segment indicates the percentage of time that the wind blew from that direction.
- **Scatter plot** Scatter plots use Cartesian coordinates to depict values of two variables in a data set, related to each other. Data are visualized as a cloud of points having values according to both the vertical and horizontal axis.
- **Linear regression** Scatter plots are the first step in a linear regression analysis, which fits a line through this cloud of points. It determines the earlier discussed slope parameter α , offset β and coefficient of determination R^2 .

5.2. Results

In this Section, the results of the comparison of the LiDAR met mast pairs are presented. It consists of two parts: a basic and a main part. Subsection 5.2.1 covers the first part and can be seen as a validation for the obtained LiDAR and met mast measurement data, gives an overview of the wind climate on site and focuses on wind speed and wind direction. The latter part in Subsection 5.2.2 includes a detailed analysis of the variable of special attention: turbulence intensity.

5.2.1. Basic analysis: wind speed and wind direction

Data availability - Regarding the measurement periods of both LiDAR met mast pairs, the measurement data availability is different for both sources and heights. As long as the measurement masts do not suffer from power outages or device malfunctions, the data availability is basically 100%. Where power outages are rare, device malfunctions are a bit less uncommon. On the contrary, LiDARs often have a lower data availability, which also decreases with ascending measurement height.

Height	Met mast 1	LiDAR 1	Met mast 2	LiDAR 2
100 m	99.5%	99.2%	91.4%	99.1%
120 m	_	-	91.4%	99.0%
140 m	99.5%	98.7%	-	-
160 m	99.5%	98.4%	-	-

Table 5.1: Data availability of both met masts and ZX 300 LiDARs for different measurement heights

To meet IEC compliance and provide high quality data, the ZX 300 LiDAR removes data it does not consider adequate. This happens for two reasons, both with accompanying filter codes in the data that replace the original value. Firstly, the code '9999' implies that a high quality wind speed measurement is not possible, which is often caused by partial obscuration of the LiDAR window or due to a very low wind speed. Secondly, the code '9998' implies that atmospheric conditions which adversely affect LiDAR wind speed measurement have been detected. Thick fog or heavy precipitation can be causes of missing data of this type. Both filter codes can not be used in data analysis and should be removed from the data sets to avoid unreliable results. Table 5.1 depicts the data availability of both LiDAR met mast pairs for several heights regarding the measurement periods mentioned in Table 4.4. Met mast 1 had some problems with malfunctioning sensors and instruments for a short period of time, resulting in a minor loss of data. Met mast 2 suffered of multiple short-term power outages, resulting in a significant loss of data of over 8%. Both LiDARs deliver incomplete data sets at all heights and show a decline in data availability as a function of height. This can be explained by more severe weather conditions at higher heights, which are known to possibly generate the earlier explained '9998' filter code in the data.

Horizontal wind speed - As elaborated on extensively in Section 3.2, LiDARs are known to be able to accurately measure horizontal wind speed. This is confirmed by several time series and their visualisations derived from measurements from both LiDAR met mast pairs. Figure 5.1 shows an example of such time series for LiDAR met mast pair 1. On the left, Figure 5.1a depicts the 10 minute data of LiDAR 1 and met mast 1 at 100 m height for a period of one week. The resulting 1008 data points per week show a very high consistency; it is hard to spot any deviation between both measurement sources. On the right, Figure 5.1b visualises the 144 data points of the third day of the earlier depicted week. It still shows a very high consistency, albeit slight deviations are a bit better visible due to the increased resolution. Similar results were obtained for LiDAR met mast pair 2, but are not shown here.

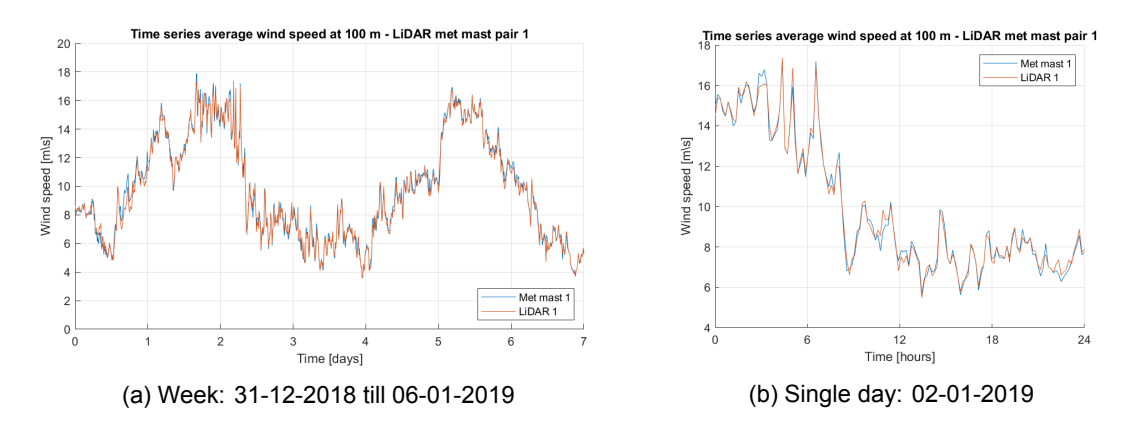


Figure 5.1: Time series average wind speed \overline{U} at 100 m height for visual comparison of LiDAR 1 and met mast 1

Parameter	LiDAR met mast pair 1	LiDAR met mast pair 2
$\overline{\overline{U}}$ LiDAR [m/s]	8.21	7.95
\overline{U} met mast [m/s]	8.21	7.97
Bias $\epsilon_{\sf U}$ [m/s]	-0.003	-0.02
Bias ϵ_{U} [%]	-0.04	-0.30
$\sigma_{\sf u}$ LiDAR [m/s]	0.70	0.67
$\sigma_{\rm u}$ met mast [m/s]	0.68	0.66
Bias ϵ_{σ} [m/s]	0.02	0.01
Bias ϵ_{σ} [%]	3.7	2.1

Table 5.2: Comparison of $\overline{\it U}$ and $\sigma_{\rm u}$ at 100 m of both LiDAR met mast pairs

Table 5.2 shows the results of the comparison of both LiDAR met mast pairs at the same height of 100 m by means of some of in Section 5.1 mentioned metrics. The similarity in mean value of the horizontal wind speed \overline{U} between both LiDARs and cup anemometers is impressively high, with a negligible bias $\epsilon_{\rm u}$ between both sources for both pairs. Such bias would not induce any significant alteration in aspects of wind resource assessment like annual energy production calculation or power curve verification. Another important metric shows less perfect results: although the standard deviation $\sigma_{\rm u}$ of both LiDAR measurements is quite close to the value measured by their accompanying met masts, higher biases ϵ_{σ} are obtained. A less accurately measured $\sigma_{\rm u}$ by the LiDARs is an omen of a known drawback of LiDARs: due to the volumetric averaging in the conical shaped measurement volume it is less capable of capturing short-term and small-scale variations, i.e. turbulence. This is clearly visible in Figure 5.2, showing a time series of $\sigma_{\rm u}$ of one day of LiDAR met mast pair 1. All examined heights together (5 in total for both LiDARs) show a very small range for \overline{U} , namely a consistent overestimation of 0.1 - 0.6%, and a little bit less narrow range for $\sigma_{\rm u}$ consisting of a consequent overestimation of 2 - 5%.

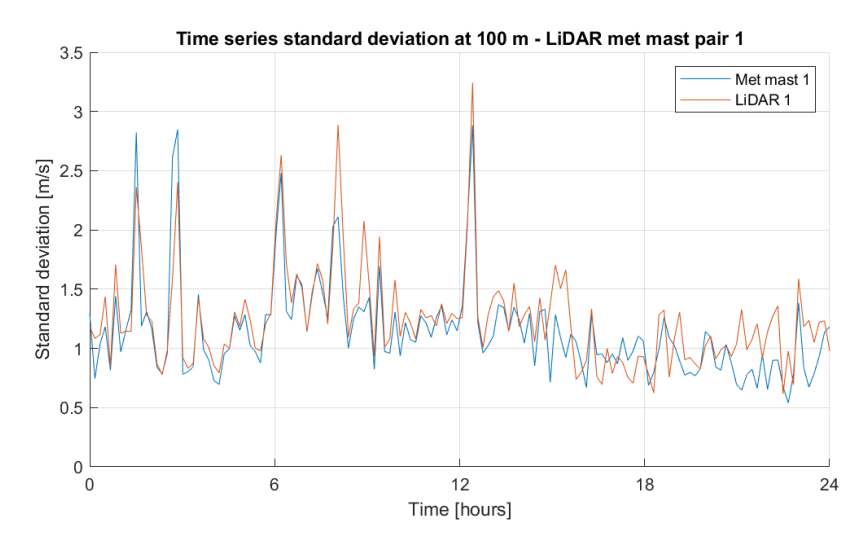


Figure 5.2: Time series standard deviations $\sigma_{\rm u}t$ at 100 m height for LiDAR met mast pair 1 of one day: 25-03-2019

Weibull distribution of wind speed - Horizontal wind speed naturally follows a Weibull curve in the long-term. When all wind speeds in a data set are binned in bins of e.g. 1 m/s, a histogram can be composed. In an attempt to capture the wind speed distribution in a function matching this histogram, the Weibull distribution is very useful. Equation 5.1 shows the probability density function of a Weibull random variable, as which the long-term wind speed can be seen, with average horizontal wind speed \overline{U} , scale parameter a and shape parameter k. Since \overline{U} is known for both LiDARs and met masts (see Table 5.2), this leaves us with two unknown variables: a and k. These can be traced with the help of various algorithms, of which the Wind Atlas method and the least squares fit method are the most known and used ones. For this analysis, the latter one is used and explained in detail in Appendix A. The results are shown in Figure 5.3. Firstly, in Figure 5.3a the consistently accurate results of the least squares fit are shown to determine both Weibull parameters. These are inserted in Equation 5.1 and lead to the red curve in Figure 5.3b, which fits the histogram of the wind speeds in the same figure 5.3b very well. The process of determining the Weibull parameters via the least squares fit algorithm is repeated based on the data of both LiDARs and met masts. This results in fairly equal Weibull parameters for both pairs, as shown in Table 5.3.

$$f(\overline{U}, k, a) = \frac{k}{a} \left(\frac{\overline{U}}{a}\right)^{k-1} e^{\left(-\left(\frac{\overline{U}}{a}\right)^{k}\right)}$$
(5.1)

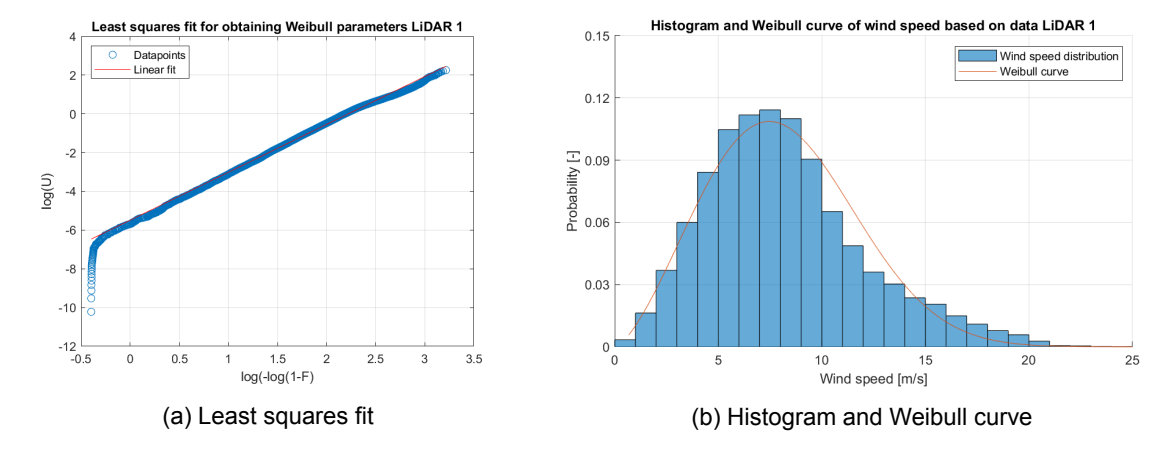


Figure 5.3: Determining scale parameter a and shape parameter k of the Weibull distribution. On the left the first step: a least squares fit to determine both parameters, and on the right the second step: visualizing the wind speed distribution by means of a histogram and the obtained Weibull curve. The above is based on data of LiDAR 1.

	LiDAR 1	Met mast 1	LiDAR 2	Met mast 2
scale parameter a	9.21	9.22	8.94	8.96
shape parameter k	2.47	2.40	2.34	2.30

Table 5.3: Obtained Weibull distribution parameters for both LiDAR met mast pairs by applying least squares fit

Linear regression horizontal wind speed - Unforced ordinary least squares (OLS) linear regression analysis, as introduced in Subsection 2.3.2, is performed on the measurement data of the 10 minute horizontal wind speed U at two different heights for both LiDAR met mast pairs. It starts with composing a scatter plot, with on the x-axis the independent variable or predictor and the dependent variable presented on the y-axis. In this comparison, the met mast measured wind speed is the independent variable and the LiDAR measured wind speed is the dependent variable. Figure 5.4 and Figure 5.5 show the scatter plots of U of LiDAR met mast pair 1 at 100 m and 160 m height, respectively. Where in Figure 5.4 both unfiltered and filtered data and their fitted lines are presented, in Figure 5.5 only the unfiltered data is visualized.

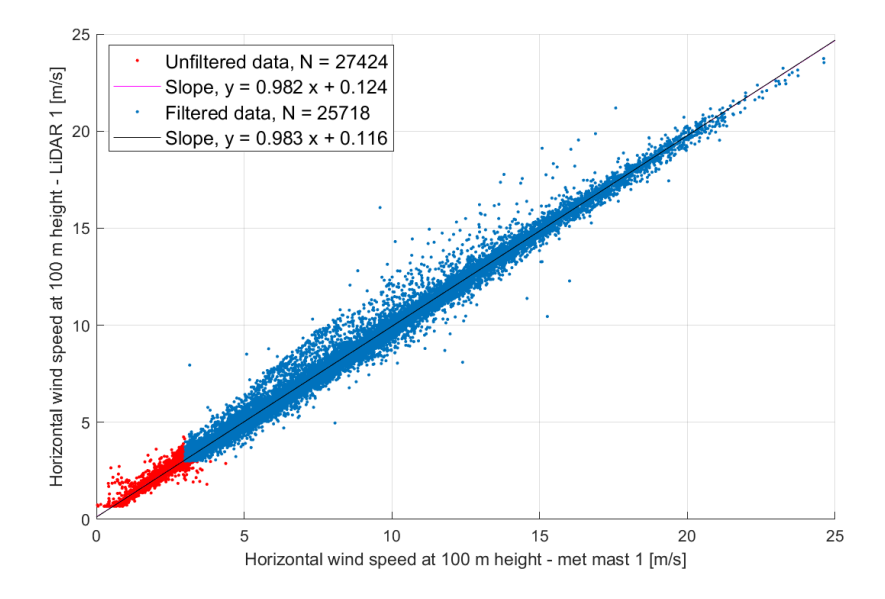


Figure 5.4: Scatter plot of horizontal wind speeds for LiDAR met mast pair 1 at 100 m height. The data in red is excluded in the filtering step since the threshold of U > 3 m/s is not met.

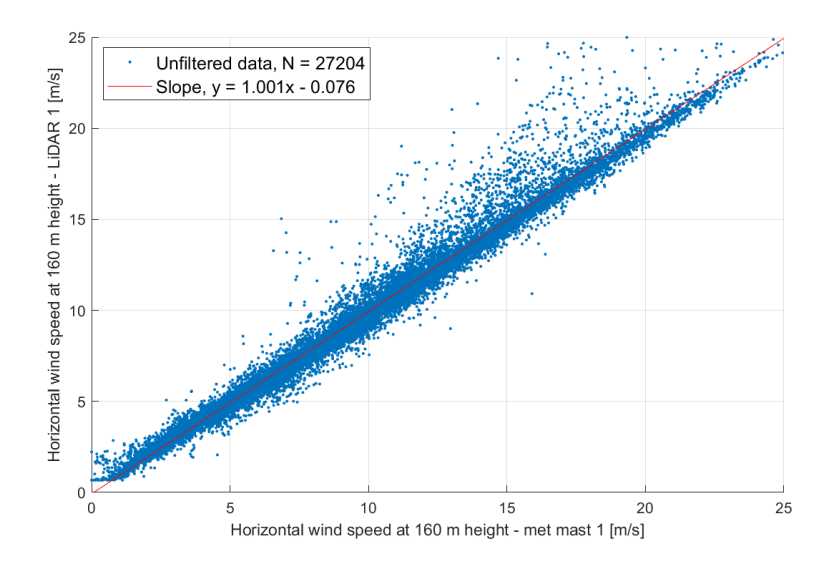


Figure 5.5: Scatter plot of horizontal wind speeds for LiDAR met mast pair 1 at 160 m height

Interestingly, the filtering of wind speeds U < 3 m/s hardly improves or even slightly deteriorates the values of R^2 , α and β . Furthermore, desired values for coefficient of determination R^2 in the range of 0.97 - 0.99 are obtained for all heights and both pairs and a small, naturally decline with height can be observed. The obtained values for slope parameter α range from 0.98 to just above unity (1.000) and are therefore inside the desired radius mentioned as proposed in Section 4.2. Finally, the linear regression analyses result in not too big offsets β , with a maximum of 0.14 for $|\beta|$. Table 5.4 gives an overview of the obtained results by means of the OLS linear regression.

		R^2	α	β
LiDAR met mast pair 1	100 m - Unfiltered	0.99	0.98	0.12
	100 m - Filtered	0.99	0.98	0.11
	160 m - Unfiltered	0.97	1.00	-0.08
	160 m - Filtered	0.97	1.01	-0.13
LiDAR met mast pair 2	100 m - Unfiltered	0.99	0.98	0.14
	100 m - Filtered	0.99	0.98	0.12
	120 m - Unfiltered	0.98	0.99	0.01
	120 m - Filtered	0.98	0.99	-0.03

Table 5.4: Precision and accuracy of horizontal wind speed measurements by both LiDAR met mast pairs compared by means of coefficients of determination R^2 , slope parameter α and offset β for different heights

Wind direction - In Figure 5.6, two scatter plots of wind direction measured by LiDAR met mast pair 1 are presented. The fact that linear regression on this data would be troublesome can be read from both plots, wind direction is therefore only visually evaluated. The thick diagonal indicates a fairly good relation between the wind directions at 100 m and 160 m height measured by LiDAR and by met mast, respectively. In both upper left- and bottom right corners, the transition from 360° to 0° or vice versa that makes linear regression meaningless, is visible. This is inconvenient, but not illogical or very inaccurate and happens when e.g. the LiDAR measures a wind direction of 359.93° and the met mast measures a wind direction of 0.04° at the same time. Another remarkable outcome is the apparent 180° shift between the wind direction between both sources that is sometimes present. Besides the thick middle diagonal and both point clouds in the upper left- and bottom right corner, two more vague diagonal point clouds are present, indicating the measurement bias between both devices.

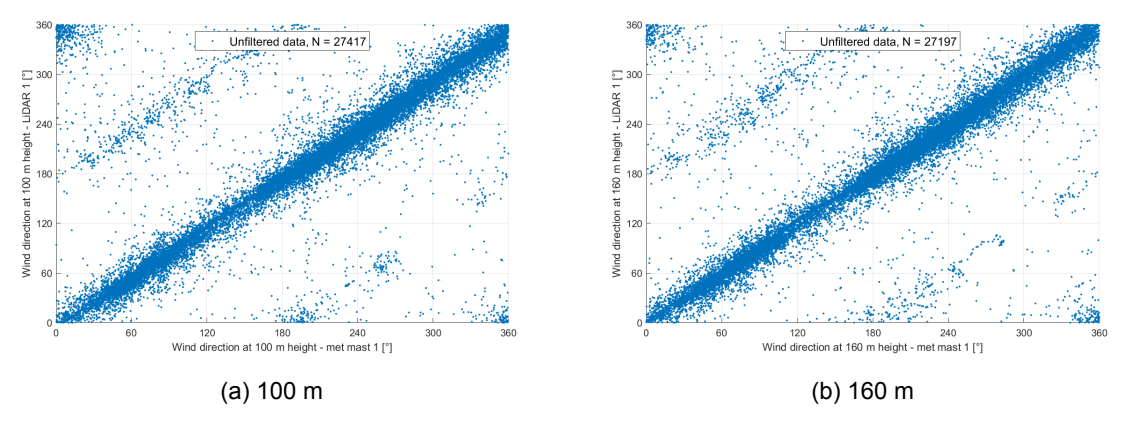


Figure 5.6: Scatter plots of the wind direction measured by LiDAR met mast pair 1 for two different heights

Similar results were obtained for LiDAR met mast pair 2, but are not shown here. The measurement data points that are shifted 180° are filtered out. Figure 5.7 depicts four wind roses, indicating the percentage of occurrence of every wind sector of 15° measured by LiDAR 1 and met mast 1 for heights of 100 m and 160 m. Every wind rose, from Sub-figure 5.7a to 5.7d, confirms wind sector 225-240° as the median; the most commonly measured wind direction. There are some inconsistencies in the retrieved wind roses and these originate from three possible causes: the binning procedure and according bin width of 15°, the in Figure 5.6 observed 180° shift that sometimes occurs between LiDAR and met mast measurements and the limited number of significant digits in the measurements itself.

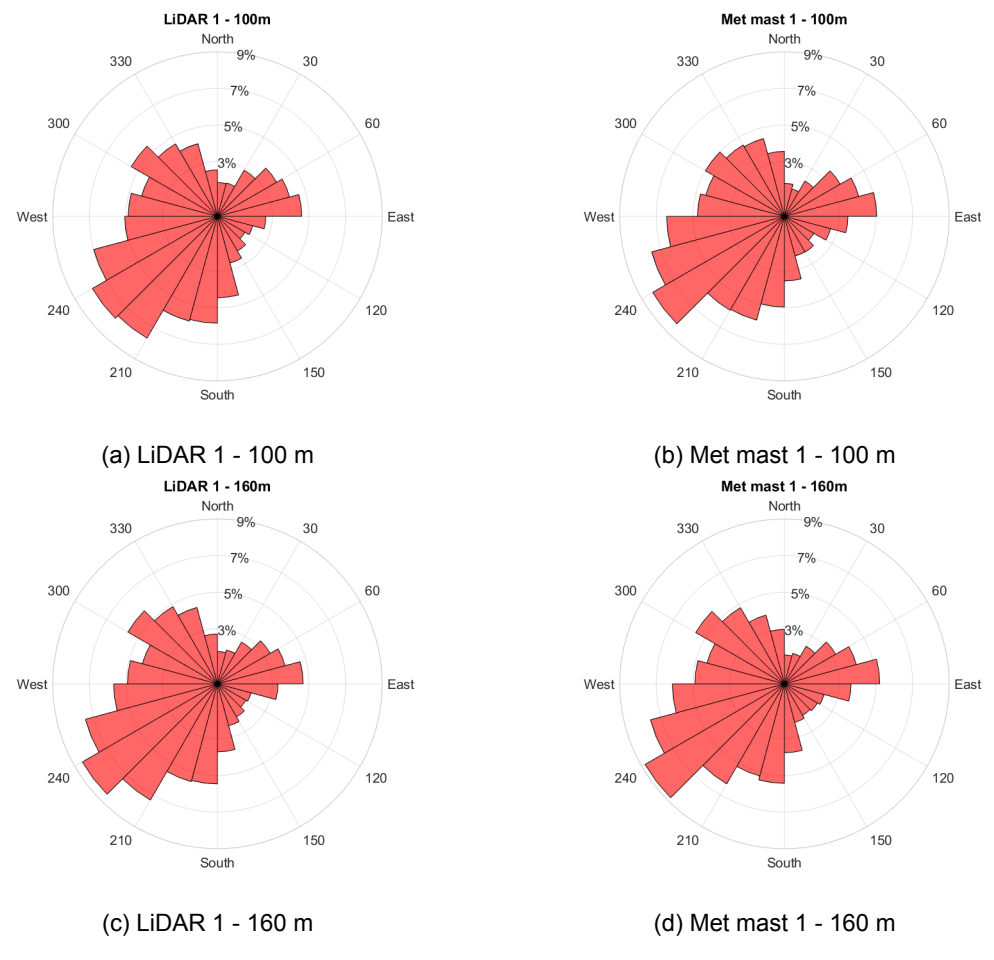


Figure 5.7: Wind roses retrieved from LiDAR met mast pair 1 measurements at two different heights

5.2.2. Main analysis: turbulence intensity

Obtain turbulence intensity from LiDAR and cup anemometer measurements - Where the ZX 300 LiDAR directly calculates the turbulence intensity TI for every 10 minute interval from the 10 minute average horizontal wind speed \overline{U} and the 10 minute standard deviation $\sigma_{\rm u}$, the cup anemometers on the met masts do not give separate TI values. Instead, it should be calculated 'manually' by means of Equation 2.6, which was introduced in Subsection 2.1.2.

$$TI = \left(\frac{\sigma_u}{\overline{U}}\right) \frac{1}{C} \tag{5.2}$$

Despite the fact that the ZX300 LiDAR directly outputs TI values, an operation of the original values has taken place beforehand. The device uses a correction factor C, under the assumption that a correction is needed to convert the scan-averaged LiDAR measurements to measurements comparable with the point-measurements of cup anemometers. Equation 5.2 is an adaptation of the earlier discussed formula for TI, where C is the height-dependent correction factor used by the ZX300 LiDAR. Below 20 m and above 90 m height, C is a constant. In between, C is a function of height C is defines the correction factor exactly. All LiDAR measured C is throughout this chapter (and thesis) includes the correction factor from Equation 5.2.

Measurement height	10 - 20 m	20 - 90 m	> 90 m
Correction factor C	1.037	-0.0017H + 1.071	0.918

Table 5.5: Correction factors used by the ZX300 LiDARs for different ranges of height

General observations in measured TI - Figure 5.8 shows a time series of a week in the beginning of June 2019 including 1008 data points and contains a few typical aspects of LiDAR and met mast measured turbulence intensity. The first aspect is the suddenly occurring short and high peaks in TI observed by both devices. These are due to a relatively intensively varying wind speed during periods of low wind speeds, i.e. 0 < U < 4 m/s. Inconsistent measurement differences between LiDAR and met mast are a common consequence during these wind regimes, in which both devices are often not able to present close to similar measurement results. Sometimes the peak measured by LiDAR is significantly higher than the one measured by the met mast and at other moments vice versa.

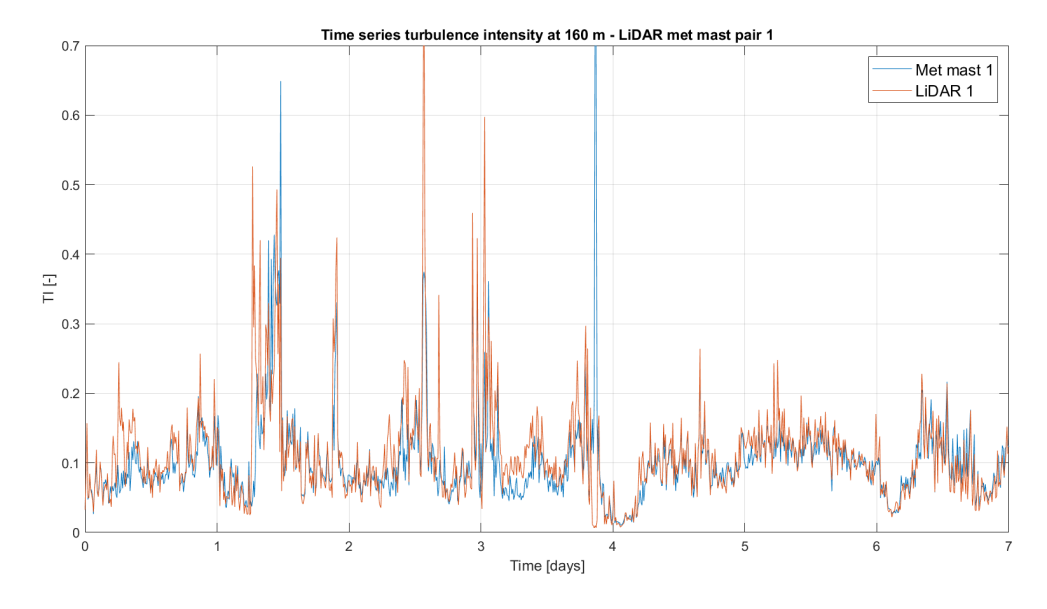


Figure 5.8: Time series of the week of 03-06-2019, showing turbulence intensity TI at 160 m height for LiDAR met mast pair 1.

Secondly, it can be observed that LiDAR often overestimates the value for TI when compared to the met mast measured value. By far most of the time, the LiDAR measured TI is above the met mast measured TI. The third aspect lies in the more volatile behavior of the LiDAR measured TI. It generally shows more intense peaks and troughs throughout the measurement period. Especially the second and third aspect can be observed in more detail in Figure 5.9, where the last two days of the above introduced week in June 2019 are depicted.

Table 5.6 summarizes the comparison of LiDAR met mast pair 1 and 2 at 5 heights in total on several of the earlier introduced metrics of comparison: mean $\mu_{\rm TI}$, bias between the mean $\epsilon_{\rm TI}$, standard deviation of TI $\sigma_{\rm TI}$ and its accompanying bias ϵ_{σ} . Consequently higher $\mu_{\rm TI}$ and $\sigma_{\rm TI}$ values derived from LiDAR measurements when compared to met mast measured values support the above discussed visual observations. Where the higher $\mu_{\rm TI}$ values are in accordance with the second aspect, the higher $\sigma_{\rm TI}$ values are in accordance with the third aspect.

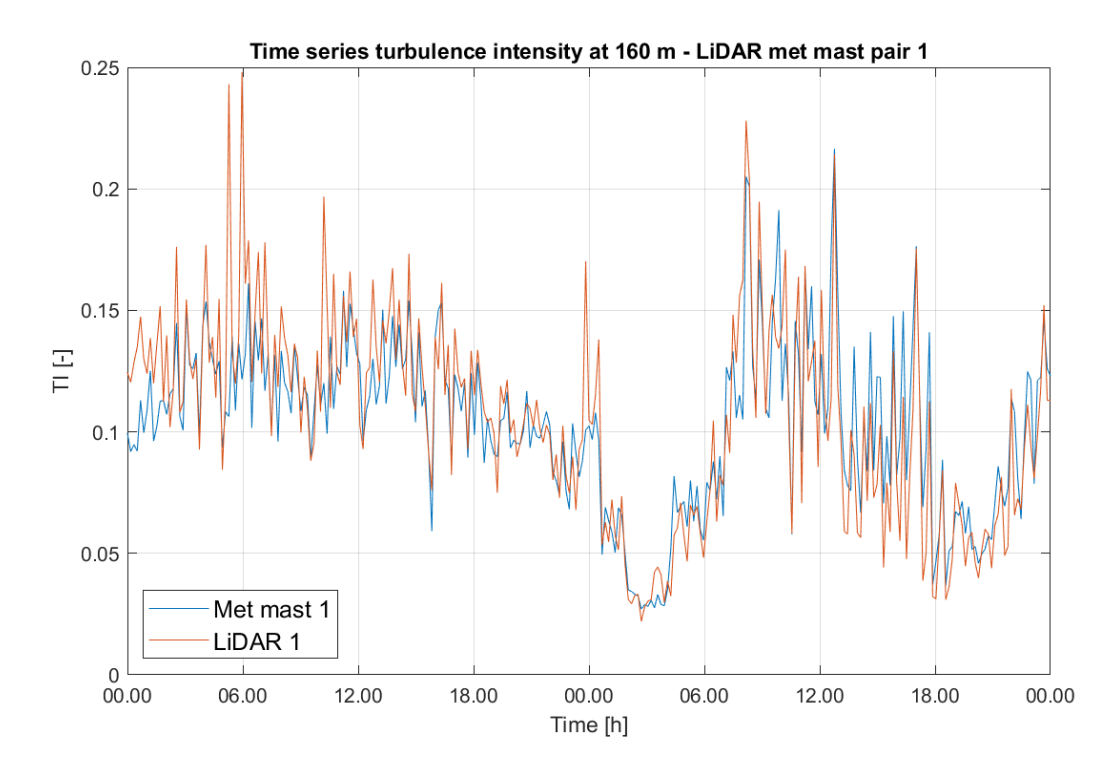


Figure 5.9: Time series turbulence intensity TI at 160 m height for visual comparison of LiDAR 1 and met mast 1. This time series covers two days, 8 and 9 June 2019, and is a zoomed version of the last two days shown in Figure 5.8.

Parameter	1 - 160 m	1 - 140 m	1 - 100 m	2 - 120 m	2 - 100 m
μ_{TI} LiDAR [-]	0.086	0.088	0.097	0.092	0.095
μ_{TI} met mast [-]	0.074	0.079	0.091	0.082	0.089
Bias ϵ_{TI} [-]	0.012	0.009	0.006	0.010	0.006
Bias ϵ_{TI} [%]	13.5	10.3	6.0	10.6	6.5
σ_{TI} LiDAR [-]	0.061	0.060	0.059	0.065	0.064
σ_{TI} met mast [-]	0.055	0.054	0.051	0.062	0.061
Bias ϵ_{σ} [-]	0.005	0.006	0.008	0.003	0.004
Bias ϵ_{σ} [%]	8.8	10.4	13.4	3.9	5.4

Table 5.6: Comparison of measured turbulence intensity at three heights by pair 1 and two heights by pair 2 by means of the earlier explained metrics: bias between mean turbulence intensity ϵ_{TI} , standard deviation σ_{TI} and its accompanying bias ϵ_{σ} .

Turbulence intensity as a function of height - Considering turbulence intensity measurements from LiDAR met mast pair 1 at three different heights and from LiDAR met mast pair 2 at two different heights, several patterns can be observed, mainly based on Table 5.6. General patterns as a function of height are present, as well as differences between LiDAR and met mast as a function of height, which are both listed below.

- As explained in Section 2.1, the origin of turbulence lies in dynamical instability caused by wind shear and in thermal instability induced by warmth of the Sun rising up from the Earth. Both factors decrease with height, as surface drag and thermal activity are less present further away from the Earth's surface. In accordance with this natural atmospheric boundary layer behavior, the mean turbulence intensity μ_{TI} decreases with height. This pattern is consequently observed by both LiDAR and met mast.
- LiDAR tends to overestimate μ_{TI} for all heights. This is also clearly visible in Figure 5.10, which contains two U versus TI plots. When the distribution on the left of met mast 1, in Figure 5.10a, is compared to the one on the right in Figure 5.10b of LiDAR 1, a generic presence of high outliers of TI by LiDAR can be observed, especially for lower wind speeds. LiDAR tends to overestimate TI due to variance contamination, which means that additional variance components contaminate its true value (see Section 2.2.2). It should be noted that the variance σ_u^2 is meant here, which is directly linked to standard deviation σ_u , which is in turn one of the two main building blocks of turbulence intensity via Equation 5.2.
- The bias ϵ_{TI} between both measurement devices increases with height, which is suspected to be a result of the variance contamination by LiDAR. As explained in Subsection 2.2.2, the homogeneous flow assumption inherently cause overestimation in LiDAR TI measurements. This bias naturally increases with height, since the scanning disc is wider at higher heights.
- The spread of TI measurements and accompanying σ_{TI} from both sources increases with height, albeit to a small extent. It is not known what causes the slight increase with height of the standard deviation. It is noticeable that for all heights (σ_{TI} is almost as big as μ_{TI} according to Table 5.6 and σ_{TI} approaches μ_{TI} even further at higher heights.
- The higher spread of LiDAR measurements logically aligns with the higher σ_{TI} values obtained from LiDAR data at each height. This increased spread can again be observed in the comparison in Figure 5.10 too.

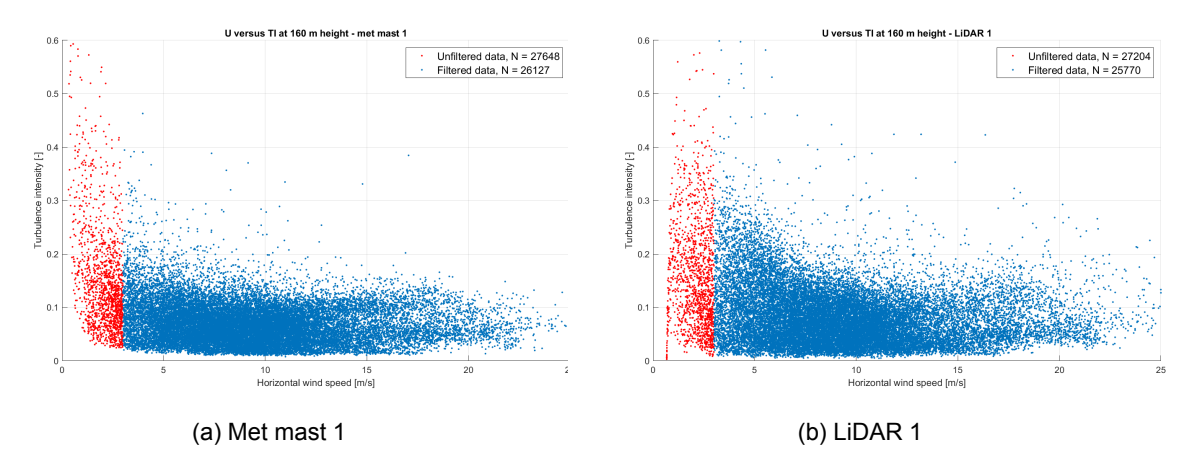


Figure 5.10: Wind speed versus TI at 160 m height from met mast 1 and LiDAR 1. The red dots indicate the excluded wind speeds U < 3 m/s.

• Figure 2.4 introduced the classes A, B and C for the turbulence classification of sites by the IEC. Taking the difference between Figures 5.10a and 5.10b into account, the overestimation of TI and the increased amount of outliers measured by LiDAR can have consequences for this IEC classification. Since the existing classes are quite conservative, the difference between LiDAR and met mast measured TI will not cause a shift in class. In a possible future with a more meticulous classification, these LiDAR met mast differences might cause classification inconsistencies.

Results linear regression - Unforced ordinary least squares (OLS) linear regression is performed on the measurement data of both LiDAR met mast pairs at three heights for pair 1 and 2 heights for pair 2: 100 m, 140 m and 160 m for pair 1 and 100 m and 120 m for pair 2. A distinction is made between unfiltered and filtered data: the latter implies an exclusion of TI measurement data corresponding to wind speeds U < 3 m/s at such moments in time. These data points are excluded for two reasons. Firstly, these low wind speed regimes are not of enormous importance for wind industry since the cut-in wind speed of modern turbines usually lies between 3 and 4 m/s. Secondly, data representing low wind speeds is more prone to errors and offsets and can unnecessarily influence regression results to a significant extent. The results in the form of the earlier introduced and discussed parameters coefficient of determination R^2 , slope parameter α and offset β are summarized in Table 5.7 and visualized with scatter plots and their accompanying linear regression slopes in Figure 5.11.

		R^2	α	β
LiDAR met mast pair 1	100 m - Unfiltered	0.475	0.795	0.024
	100 m - Filtered	0.601	1.041	0.002
	140 m - Unfiltered	0.402	0.732	0.032
	140 m - Filtered	0.560	1.043	0.010
	160 m - Unfiltered	0.373	0.670	0.036
	160 m - Filtered	0.541	1.049	0.009
LiDAR met mast pair 2	100 m - Unfiltered	0.426	0.690	0.034
·	100 m - Filtered	0.637	1.065	0.002
	120 m - Unfiltered	0.616	1.033	0.007
	120 m - Filtered	0.669	1.167	-0.003

Table 5.7: Precision and accuracy of TI measurements from both LiDAR met mast pairs compared by means of coefficients of determination R^2 , slope parameter α and offset β for three different heights

In general, it is striking that the above discussed data filtering makes a lot of sense. Filtering of data poses big differences in the resulting coefficients of determination and regression parameters. The slope parameter α approaches 1.000 to a satisfying extent for all heights after filtering, where certainly less desired values are obtained before filtering. Values around 1.04 for α for all heights confirms the earlier observed consequent overestimation of TI by LiDAR. An offset β < 0.01 for all heights obtained after filtering is fairly acceptable. Relatively low values for R^2 are obtained, albeit the results after filtering are certainly sufficient. These low values might be at least partly due to the high heights under analysis compared to most earlier studies, as discussed in 3.2.

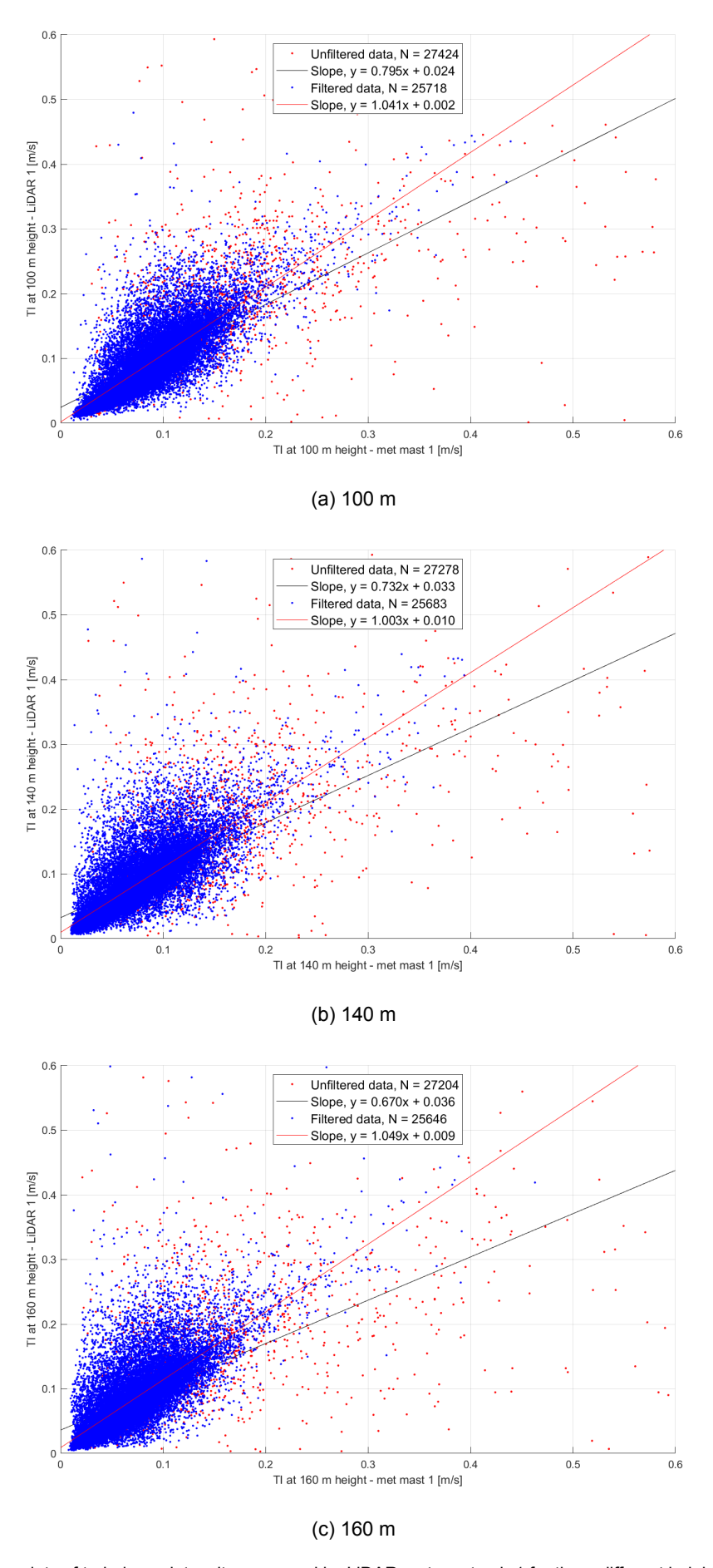


Figure 5.11: Scatter plots of turbulence intensity measured by LiDAR met mast pair 1 for three different heights. Unfiltered and filtered data are shown in red and blue respectively, as well as linear regression fits and their resulting formulas.

Overestimation of standard deviation - Because of the earlier explained suspicion of an consequent overestimation of σ_u by LiDAR compared to a met mast, which in turn leads to an overestimation of the turbulence intensity, some further research is conducted on this issue. Figures 5.12a and 5.12b show the scatter plot of standard deviation σ_u as a function of wind speed U retrieved from met mast 1 and LiDAR 1 data, respectively. A clear, positive deviation for LiDAR measured σ_u is visible on the right, when compared to the left data from the met mast. Out of a total of 27,648 data points, a significant difference in amount of values satisfying $\sigma_u > 1$ m/s are discovered between LiDAR and met mast: 4273 or 15.5% for met mast 1 and 4725 or 17% for LiDAR 1. This considerable surplus of over 2.5% in favour of the LiDAR measurements confirms the suspicion of σ_u overestimation by LiDAR. It can be deduced visually that this happens mainly at lower wind speeds, i.e. U < 7 m/s.

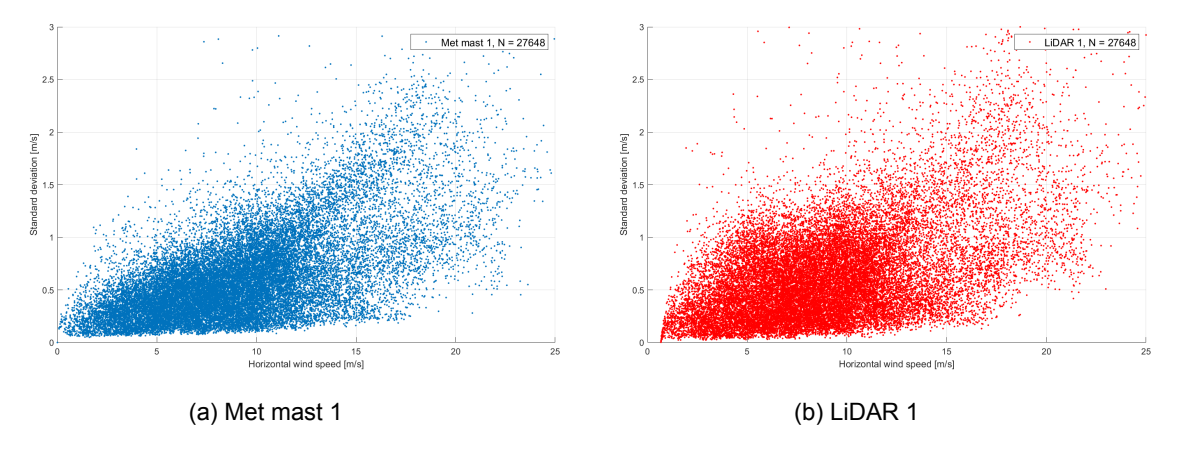


Figure 5.12: Wind speed $\it U$ versus standard deviation $\sigma_{\rm u}$ at 160 m height from met mast 1 and LiDAR 1.

Influence of wind direction on TI - Since no serious obstacles are found in a radius of 300 m around LiDAR 1 and only minor obstacles like trees and other low growth are present at 500 m distance or more, an interesting distinction could be made for LiDAR met mast pair 1. Turbulence intensity *TI* measurements were subdivided in two wind direction sectors. The first sector comprises of all measurements with a wind direction coming from the nearby IJsselmeer lake (sea breeze) and the second sector includes *TI* measurements that include measurements which wind flow originates from the land (land breeze). Both sectors are depicted in Figure 5.13. The lake sector in red and land sector in blue include *TI* measurements with an according wind direction range of 240° - 360° an 90° - 180°, respectively. By defining the wind direction range of both sectors in this way, it is made sure that both sectors include an approximate similar number of data points, to know around 25% for both sectors out of a total of 27,000 data points. Both sectors accurately represent the source of the wind: the lake and the land, respectively.

		140 m	160 m
Wind from land	μ_{TI} from LiDAR	0.089	0.086
	μ_{TI} from met mast	0.079	0.075
	Bias (%)	+10.9	+14.6
Wind from lake	μ_{TI} from LiDAR	0.083	0.081 0.071
	μ_{TI} from met mast	0.075	
	Bias (%)	+9.8	+13.3

Table 5.8: Comparison of μ_{TI} at two heights and for both direction sectors for LiDAR met mast pair 1

Table 5.8 depicts the average turbulence intensity μ_{TI} measured by LiDAR met mast pair 1 at 140 m and 160 m height for both wind sectors defined above. As expected, the turbulence intensity is slightly higher in the wind coming from land compared to the wind coming from the nearby lake. On average, the difference in TI between both sectors is 8% for at 140 m and 6% at 160 m. This drop originates from the inherent fact that turbulence intensity declines with increasing height. Next to that, the bias between both measurement sources is almost the same for both examined heights. The same overestimation of TI by LiDAR is observed at 140 m and 160 m, of approx 10% and 14% respectively. This is in accordance with the findings presented in Table 5.6. The bias for the land sector is however slightly higher than the overall average bias in Table 5.6, where the bias found for the lake sector is somewhat lower than this.

With the nearby presence of a large body of water, an internal boundary layer (IBL) could be formed around location 1 in wind farm "Windplan Blauw". This is a layer that can form within the ABL due to horizontal winds across discontinuous surfaces. The IBL originates at the transition of surface and grows thicker downstream. At some point it vanishes again via ambient mixing within the ABL [51]. A common example thereof is the transition between water and land, something that is happening at the location of LiDAR 1. It is placed near the IJsselmeer lake shore and wind coming from the lake arrives above land just before it is measured by LiDAR 1.

Increased turbulence in the wind coming from land could be an effect of the formation of an internal boundary layer (IBL) [97]. However, since the average slope of an IBL is found to be between 1/10 and 1/100, it is not likely that the *TI* measurements at heights of 140 and 160 m are affected by the formed IBL [2]. The distance from LiDAR 1 to the IJsselmeer lake is around 400 m, which seems to little to find effects of an IBL in the measurements presented in Tables 5.8 and 5.9.



Figure 5.13: Lake and land wind direction sectors for LiDAR 1, indicated by the orange dot

		R ²	α	β
LAND	140 m - Unfiltered	0.42	0.70	0.03
	140 m - Filtered	0.62	1.17	0.00
LAKE	140 m - Unfiltered	0.44	0.74	0.03
	140 m - Filtered	0.46	0.83	0.01
LAND	160 m - Unfiltered	0.36	0.63	0.04
	160 m - Filtered	0.63	1.17	0.00
LAKE	160 m - Unfiltered	0.36	0.72	0.03
	160 m - Filtered	0.44	0.90	0.01

Table 5.9: Precision and accuracy of TI measurements from LiDAR met mast pair 1 compared by means of coefficients of determination R^2 , slope parameter α and offset β for both defined wind direction sectors

In Table 5.9, the results of the unforced linear regression analysis on the TI data of both wind direction sectors are presented. A remarkable observation is the one that filtering low speeds improves the results much more for the land sector than for the lake sector. Apparently, there are a lot a TI measurements in the wind flow coming from land with a low wind speed that are not very precise. These are filtered out and give considerably better results for R^2 and α . Next to this, slope parameter α values of 1.17 and 1.17 for the land sector versus values of 0.83 and 0.90 for the lake sector confirms the perception that the overestimation of TI by LiDAR is bigger for the land sector than for the lake sector, which was also found earlier and is visible in Table 5.8.

Proposition of the use of transience in favor of TI - Alternatively, a totally different approach in measuring turbulence can be considered. Where in wind industry and science, turbulence always has been captured with the help of turbulence intensity TI as in Equation 2.6, this is basically an expression based on a one-point statistic ($\sigma_{\rm u}$) to represent complex three-dimensional structures in the wind blowing past turbines. Exemplary is that a range of wind conditions can correspond to the same value of TI that is measured. This range encompasses uncertainties in all predictions that are based on these TI measurements. Since TI is comprehensively used for the characterization of wind energy sites to assess its suitability and IEC classification, it is a quite important factor altogether. Turbulence intensity seems to be the less favourable option in representing the variability of the wind.

$$\tau_m = \sqrt{\frac{1}{N} \sum_{i=1}^{N} (x_i - x_{i+m})^2}$$
 (5.3)

An alternative measure to statistically capture turbulence is proposed here: transience $\tau_{\rm m}$ is a two-point statistic that does not require an extensive memory nor other data processing steps. Transience shows analogy with the extensively discussed standard deviation $\sigma_{\rm u}$, of which its formula was introduced in Equation 2.11 in Chapter 2 and which is of course also part of the formula for TI in Equation 2.6. Equation 5.3 depicts the formula to calculate the transience $\tau_{\rm m}$ and shows the distinction from the standard deviation. In this equation, N equals the total of measurement data points in a 10 minute interval, which is 600. Next to that, i represents the count that runs through this set of measurements and m is equal to 1 here, since adjacent data points are paired. Where $\sigma_{\rm u}$ is based on the mean square difference between values and the mean, transience is about the mean square difference between pairs of values. As a result, transience varies for all conditions and allows to differentiate otherwise similar situations. In other words, $\tau_{\rm m}$ varies more with degree of scatter than TI. This could mean that $\tau_{\rm m}$ is more useful in representing turbulent structures than $\sigma_{\rm u}$ based TI.

The most relevant advantage of using transience over standard deviation for this research is the fact that wind measurements will be better able to represent turbulence, something at which LiDAR is still struggling. This all could enhance the acceptance and integration of LiDAR in wind industry and science. Because transience $\tau_{\rm m}$ varies with the degree of scatter in wind measurements, it allows the distinction of different measurement sets. This is in contrast to $\sigma_{\rm u}$, which would give approximately the same values for these indeed distinct measurement sets. In addition, this way of handling wind measurement data causes one to be more capable of capturing turbulent length scales and is rather easy to implement to assess site suitability and classification. Next to that, very important for wind turbine design and relevant with regard to Chapter 6, transience is known to be a better predictor of mechanical fatigue loads for both blades and tower [12]. The relationship between an example damage equivalent load and transience $\tau_{\rm m}$ demonstrates a far higher consistency than the same relationship with $\sigma_{\rm u}$. Being a better predictor of damage equivalent loads with respect to turbulence intensity and standard deviation, transience statistics could allow valuable improvement in fatigue load assessment.

An important drawback of the implementation of transience in wind site assessment would be that fact that all current programs, standards, measuring devices, software packages, design tools and more are tailored to the use of turbulence intensity TI and standard deviation $\sigma_{\rm u}$. These turbulence parameters are not only deeply rooted in measuring devices like met masts and LiDARs, but also in lots of software for aerodynamic and aeroelastic simulations and calculations like TurbSim and FAST, which are used in Chapter 6. These simulations and calculations are essential for the design of wind turbines. Changing from one to another would require an intense paradigm shift in wind industry and science, something which can plainly be seen as a crucial impediment.

Questioning the use of 10 minute averaged measurement data - Throughout wind science and industry, the 10 minute averaging period is used almost without exception for site assessment. This means that the mean wind speed \overline{U} of this interval and the spread of 600 1 second measurements around this mean in the form of the standard deviation $\sigma_{\rm u}$ are the instruments to assign a value to the degree of turbulence in that interval, which is the turbulence intensity TI. It has already been researched that the average wind speed \overline{U} is not very sensitive for the length of the averaging period. In [28], it was found that a 2 minute versus 10 minute period does not pose significant changes in the values for the obtained average wind speed. It should be noted that this observation applies to flat open terrain, just as in this research. This could differ for more complex terrain or other locations. According to [76], averaging periods shorter than a few minutes will not sufficiently smooth the natural turbulent structures of the wind to obtain usable average wind speeds.

Since turbulent structures in the wind are often very small scale as explained in Subsection 2.1.2, e.g. 1 or 2 minutes, the question arises if 10 minute averaging period measured TI can interpret this small scale turbulence sufficiently. Being able to account for instantaneous gusts and rapidly changing wind speed is very valuable for loads and stresses analyses, turbine selection and IEC site classification. As touched upon in the paragraph concerning transience too, many situations can occur within 10 minutes for the same value of TI. In fatigue lifetime analysis, this is bypassed with the help of the generation of representative wind fields, as done in Chapter 6. However, for the determination of the IEC turbulence class of a site (see Figure 2.4) and other uses of TI measurement data, this is not. This reveals a weakness in the use of 10 minute averaged TI as an indicator for turbulence.

5.3. Discussion and conclusion

Findings and observations based on basic analysis - The findings in Subsection 5.2.1 show how LiDAR and met mast measurement data can be compared on data availability, horizontal wind speed U and related mean \overline{U} and standard deviation $\sigma_{\rm u}$, determination of Weibull parameters a and k, linear regression of U and visual comparison of wind direction measurements. The following conclusions can be appended to these comparisons.

Firstly, the data availability of both met masts is intrinsically better than the data availability of both ZX 300 LiDARs and the data availability of the LiDAR devices is also declining with height due to the earlier described appearing filter codes '9998' and '9999'. This decline with height is also found in other studies like [103] and [13]. Conversely, LiDAR devices are electronically seen more reliable, since met masts tend to suffer more often from device malfunctions or power outages.

Next to that, values for mean wind speed \overline{U} and standard deviation σ_u are in respectively perfect and good alignment with each other. In line with the studies mentioned in Section 3.2, a negligible difference for the mean wind speed is found. A slightly higher value for the overall mean standard deviation measured by LiDAR is found for both pairs at all heights examined. This is found more often in research, e.g. by [124] and [16], and is expected to be caused by the earlier explained principles of volume averaging and variance contamination.

Thirdly, the determination of both Weibull parameters of the long-term wind speed distribution, scale parameter a and shape parameter k, via the least squares fit method based on both measurement sources is spot on. The use of the least squares fit as method as well as the good results are supported by earlier research like [34] and [71]. LiDAR measured wind speed data are apparently also very useful in accurately determining the Weibull distribution parameters.

Furthermore, the OLS linear regression performed between the met mast and LiDAR data of both pairs shows good results. The rounded coefficients of determination R^2 range between 0.98 and 0.99 for all 4 comparisons and the rounded slope parameters α are between 0.98 and 1.00, which is both comparable to the research results listed in Section 3.2 and other studies regarding this comparison, to know studies like [88], [61] and [44]. Remarkably, the data filtering does not cause significant improvements in precision and accuracy.

Lastly, the wind direction of LiDAR and met mast was compared visually. Both pairs show a good agreement in measured wind direction at different heights. The most noticeable finding is a 180° shift that is observed throughout the data. It occurs not often, but a pattern is certainly visible. This bias is not discussed extensively in literature, but nevertheless also found by other research, such as [70] and [61].

Observations and conclusions regarding turbulence intensity - The different findings from Subsection 5.2.2 concerning LiDAR versus met mast measured TI are summarized and elucidated on below, accompanied with a discussion of the obtained results. To start, LiDAR consequently overestimates the TI mean μ_{TI} compared to its accompanying met mast for both LiDAR met mast pairs and all heights under investigation. This is a common bias, earlier experienced in other research like the ones from [103], [23] and [88]. This bias increases with height for both LiDAR met mast pairs, something which is probably caused by the volumetric averaging that underlies the working principle of measuring wind characteristics by LiDAR.

Secondly, the natural decline of μ_{TI} with increasing height is clearly present in the observed LiDAR and met mast data. Since wind shear and thermal instability are higher closer to the Earth, it can be said that both LiDAR and met mast consequently confirm the expected atmospheric boundary layer behavior. Thereafter, it has been observed that the spread σ_{TI} increases very little with height for both LiDAR and met mast. It is not sure why this effect is present, but it is thought to be related to a declining μ_{TI} with height. As could clearly be

seen in Figure 5.10 too, the spread of LiDAR TI measurements is higher than the spread in the TI measured by the met masts, i.e. LiDAR measurements contain more outliers in the direction of higher TI values.

Subsequently, OLS linear regression was performed between the met mast and LiDAR data of both pairs for five heights in total. The overall results are fairly satisfying, yet there are considerable differences in accuracy and precision for the filtered and unfiltered data. Filtering drastically increases the values for R^2 and α towards unity and decreases the present offset β . Since the data points that are filtered out with the threshold of U > 3 m/s are of no importance for wind resource assessment in general, it is recommended to focus on the results of the filtered data. These give relatively low values for R^2 between 0.54 and 0.67. It should be noted that many other studies, among others the ones mentioned in Section 3.2, assess the TI at lower heights than in this study. In addition to that, the coefficient of determination seems to decline with height, which is in accordance with the earlier discussed volume averaging of LiDAR. Obtained slope parameters α of around 1.05 confirm the earlier observed overestimation of TI by LiDAR and can be seen as an acceptable results. The same applies to the found offsets β , which are all smaller than 0.01.

Lastly, an approach was taken to study the effects of wind direction on the bias in measured TI between LiDAR 1 and met mast 1. A land and lake direction sector were distinguished and it was found that the μ_{TI} was higher for wind from land. Furthermore, the bias in turbulence intensity between both sources was also slightly higher in the land direction sector. These findings were confirmed by the conducted linear regression analysis for both sectors.

Origin of inaccuracy of LiDAR measured TI - Ultimately, there can be three possible causes of inaccuracy of TI measured by LiDAR, when compared to met masts. Following Equation 5.2, these causes can be the 10 minute average wind speed \overline{U} , the 10 minute average standard deviation of the wind speed $\sigma_{\rm u}$ and the internal correction factor C that is used by ZX300 LiDAR devices. The first factor \overline{U} can be excluded, since for a total of five examined heights at two different locations the difference between both sources is consequently negligible. The difference between the average wind speed measured by both LiDARs and met masts ranges between 0.1% and 0.6%. This exclusion is further supported by the findings of the OLS regression analysis on \overline{U} , showing R^2 and α values in the range of 0.98 to 1.01.

The second factor σ_u is of more influence on the found differences in turbulence intensity between LiDAR and met mast. The hypothesis that LiDAR will consequently overestimate the 10 minute standard deviation of the horizontal wind speed due to volumetric averaging and/or variance contamination is confirmed by the analysis of the measurement data at all heights. This is supported by Figure 5.12. This scatter plot also shows that LiDAR σ_u measurement deviate the most in lower wind speed regions. Figure 5.10 confirms that this affects TI in the same fashion, i.e. mostly for U < 7 m/s. On the contrary of \overline{U} , the differences for σ_u between both sources are significant and range between 2% and 5% for both examined LiDAR met mast pairs. An important observation is that this difference remains closer to constant; it does not increase as much with height as \overline{U} . Nevertheless, the overestimation of σ_u cannot be fully responsible for the fact that the TI values are consequently overestimated, since the differences in TI are all considerably higher than those in σ_u .

Alteration of internal correction factor - This leaves the internal LiDAR ZX300 correction factor \mathcal{C} as possible cause for the consequent overestimation of TI. As was touched upon too at the start of Subsection 5.2.2, all measurement in this research include the internal correction factor \mathcal{C} . The positive bias found between LiDAR measured TI and met mast measured TI also increases with height. Figure 5.14 depicts \mathcal{C} as function of height in red, showing a rather simple relationship. The heights from 100 m up are of most interest in this case, since this range of heights covers most of the rotor area of nowadays multi-megawatt wind turbines. The consequent overestimation of TI and the fact that it increases with height, calls for considering an alteration of the correction factor. Above 90 m, \mathcal{C} is now a constant

with a value of 0.918. The reason behind this is that the correction factor is based on a comparison with a only 90 m high met mast. The value of 0.918 should serve as a correction mechanism for the consistent underestimation of $\sigma_{\rm u}$ by LiDAR and it basically works. In fact, it overdoes the correction and does not take into account that turbulence (and TI) decreases with height. Therefore, it would be advised to let C a function of height between 90 and 200 m too. This would do justice to the with height increasing bias between LiDAR and met mast measured TI, which is consistently found throughout this study. An important advantage of an refinement of C is that it is a rather simple measure, which basically only requires a small software update of the ZX300 LiDAR.

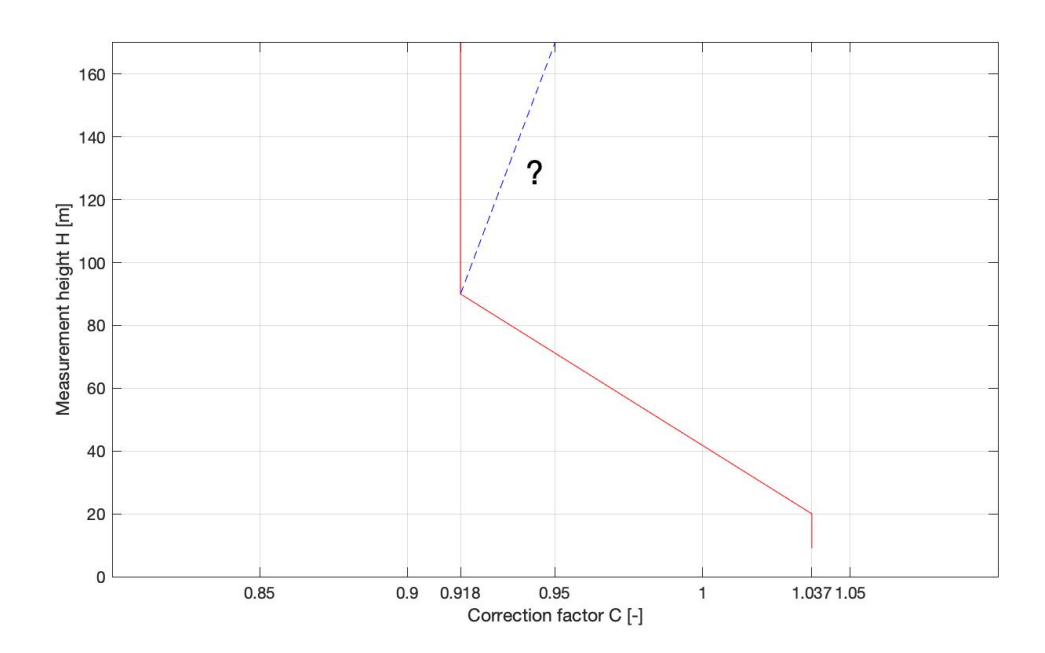


Figure 5.14: Correction factor C as a function of height H in red, proposition for modification in blue

According to the measurement biases between LiDAR and met mast measured TI found in this research, the altered course of C could look like the blue dashed line in Figure 5.14. The here presented alteration is only a rough estimation based on the results of this Chapter. They therefore specifically apply to the locations in wind farm "Windplan Blauw". Anyhow, a height dependant internal correction factor C for turbulence intensity TI should be considered for heights above $100 \, \text{m}$, to properly correct the initial measured values in this important range of heights too. This also highlights a less favourable aspect of this proposition: it would require more atmospheric turbulence research to identify different categories of turbulence shear or TI gradient to give all users of the ZX300 LiDAR a choice for a height-variable correction factor that applies to their location on Earth.

Subsequent to the above conclusions, a proposition for the use of transience in statistically representing turbulence was made. There are several advantages and drawbacks on implementing transience, but it seems to be a promising research topic. An example follow-up study on this is introduced in Appendix C. Furthermore, the ability of representing turbulent structures in the wind of 10-minute intervals was questioned. Research upon the quantitative effects of shorter averaging periods on turbulence intensity has not been conducted yet and might be interesting matter to study. Next to this, a LiDAR met mast comparison including many more locations which differ e.g. in wind speed level, turbulence level and surface roughness (onshore, offshore, rough terrain, hilly landscape) would be an ideal research setup in the light of this chapter. A data study this big could also serve as an input for possible internal correction algorithms for ZX300 LiDARs, following on the proposition for the alternation of *C* discussed above.



Sensitivity analysis on fatigue lifetime of wind turbines

This chapter comprises of a sensitivity analysis of the fatigue lifetime of a common Dutch onshore wind turbine as a function of turbulence intensity TI, which relates to research objective 3. The by means of the statistical assessment of LiDAR and met mast in Chapter 5 obtained values for the (in-)accuracy of LiDAR measured TI serve as an input for this. As elaborated on in Section 4.1, the process to achieve sound results for the last research objective is subdivided in three parts. The relevant methods are explained in Section 6.1. Thereafter, the obtained results are presented in Section 6.2 and discussed in Section 6.3.

6.1. Method

In this section the methods used in this part of the research and explained process-wise. It firstly treats the creation of several turbulent wind fields by means of TurbSim in Subsection 6.1.1. Secondly, performing aeroelastic simulations in FAST to generate time series of loads on the wind turbine is described in Subsection 6.1.2. Finally, the calculation of damage equivalent loads and time until failure to evaluate turbine fatigue lifetime as a function of μ_{TI} with the help of MLife software is elaborated on in Subsection 6.1.3. An overview of the most essential parts of this method is presented in Subsection 6.1.4.

6.1.1. Generating TI differentiated wind fields in TurbSim

About TurbSim and its general working - TurbSim is an open source stochastic inflow turbulence generator tool that has been developed by the National Renewable Energy Laboratory (NREL) of the United States of America, with the goal to provide the possibility to perform numerical simulations of full-field flows containing coherent turbulence structures. It is aimed on that these turbulent structures properly reflect the spatial and temporal turbulent velocity field relationships seen in instabilities associated with air flow in the atmospheric boundary layer. The purpose of the TurbSim software package is to give wind turbine designers the ability to drive design code simulations of advanced turbine designs. This is e.g. possible in the software package FAST, which is used in the following step of the here described research method. The mentioned turbine designs include simulated inflow turbulence wind fields that coalesce many important features of fluid dynamics, especially those aspects known to adversely affect aeroelastic loading of wind turbines, which is of interest here [7].

TurbSim can be seen as an input-output tool that generates wind fields with turbulence structures. A long, predefined list of parameters involving run-time options, turbine or model specifications and meteorological boundary conditions all have to be specified to serve as an input for the tool. In Appendix D, one of the used TurbSim input files can be found. In turn, TurbSim generates several output files that contain wind fields ready for further analysis or simulation in e.g. FAST.

TurbSim input parameters - Table 6.1 gives an overview of a large portion of the TurbSim input parameters, to know the turbine/model specification and all meteorological boundary conditions. These are indispensable to create wind fields that represent the turbulent structures present in the ABL around wind farm "Windplan Blauw" as close as possible to reality. The run-time options for running TurbSim are not displayed here, since these do not comprise of real-world variables but just initialize the pseudo-random number generator behind the working of TurbSim and define what type of output to generate. The other input parameters are elaborated on below, with the emphasis on the meteorological boundary conditions.

Turbine/model specification	Value	Meteorological boundary conditions	Value
Vertical Grid Points [-]	30	Turbulence Model [-]	von Karman
Horizontal Grid Points [-]	30	IEC Standard [-]	IEC 61400-1
Time Step [s]	0.05	IEC Turbulence [%]	7, 9, 11
Length of Analysis [s]	6000	IEC Turbulence Model [-]	NTM
Turbine Hub Height [m]	90	Type of Wind Profile [-]	IEC
Height Grid [m]	160	Reference Height z_{ref} [m]	100
Width Grid [m]	160	Reference Wind Speed u_{ref} [m/s]	8.2
Mean Vertical Flow Angle [°]	0	Power law exponent α [-]	0.2
Mean Horizontal Flow Angle [°]	0	Surface roughness length z_0 [m]	0.03

Table 6.1: Overview of used turbine/model specifications and meteorological boundary conditions in TurbSim, which are required input parameters to simulate turbulent wind fields

Turbine/model specification - With a grid height and width of 160 m, a wind field with sufficiently large dimensions is created to fully fit both tower and swept rotor area of a 5 MW onshore wind turbine with a hub height $U_{\rm hub}$ of 90 m and blades with radius r of 61.5 m. It is internally advised by TurbSim to leave 10% of the wind field blank at each side of the swept rotor area. Having 30 vertical and horizontal grid points, this leaves the wind fields with a resolution of 5.2 m in vertical and horizontal direction. The turbine is assumed to be yawing perfectly aligned with the wind and since flat terrain is considered, both horizontal and vertical mean flow angle are equal to 0°. The time step and length of analysis are default and since it is not advised to change these, these are not changed [63]. The example wind field in Figure 6.1 visualizes the notion of the above described wind field grid and grid points.

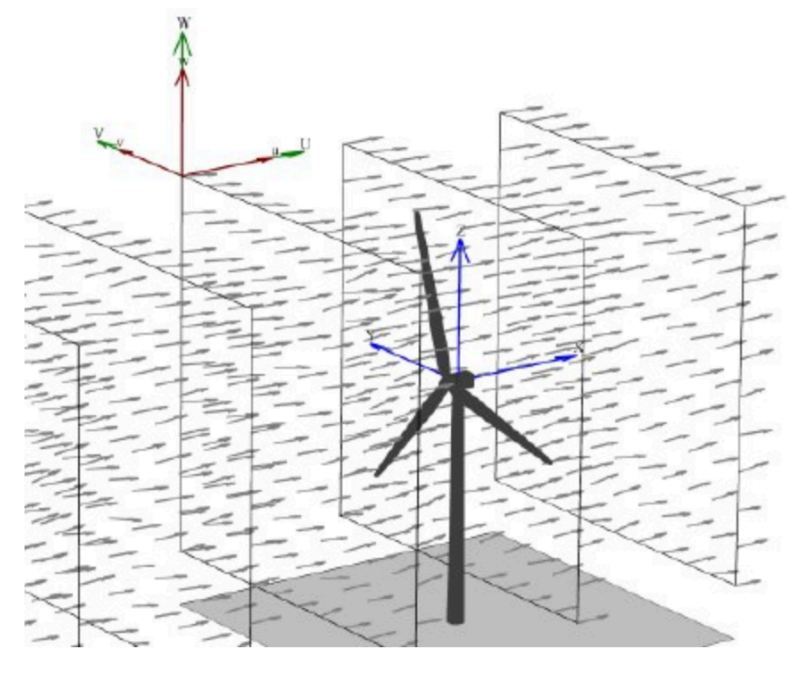


Figure 6.1: Visualization of an example wind field from TurbSim with a low resolution of grid points, wind speed components u, v and w and the element of time in the form of the consecutive square grids [41]

6.1. Method 57

Meteorological boundary conditions - To let TurbSim simulate wind fields as close as possible to reality around wind farm "Windplan Blauw", the predefined meteorological boundary conditions should be chosen with caution. To generate time series based on spectral representation, TurbSim uses a version of the Sandia method, which is a method for generating turbulent wind fields. Firstly, time series of wind speeds can be generated at a set of points on a surface, in this case the wind turbine rotor plane. Then, frequency domain analysis is performed, a domain where turbulence can be described easier quantitatively than in the time domain [7]. Finally, inverse fast Fourier transforms are applied to obtain the desired time series. Several different spectral turbulence models exist, of which the IEC compliant Kaimal and von Karman models are the most widely known and used ones. In full, the IEC Von Karman Isotropic Model is the most used model and is therefore chosen here too. The velocity spectra for the wind components in this model u, v and w are given by Equation 6.1 for u and by Equation 6.2 for w and w are given by Equation 6.1

$$S_{\rm u}(f) = \frac{4\sigma_{\rm u} \frac{L}{\overline{U_{\rm hub}}}}{\left(1 + 71\left(f\frac{L}{\overline{U_{\rm hub}}}\right)^2\right)^{\frac{5}{6}}} \tag{6.1}$$

$$S_{K}(f) = \frac{2\sigma_{K} \frac{L}{\overline{U_{\text{hub}}}}}{\left(1 + 71\left(f\frac{L}{\overline{U_{\text{hub}}}}\right)^{2}\right)^{\frac{11}{6}}} \left(1 + 189\left(f\frac{L}{\overline{U_{\text{hub}}}}\right)^{2}\right)$$
(6.2)

where f is the cyclic frequency in rad/s, $\overline{U_{\text{hub}}}$ is the mean wind speed at hub height and L is an integral scale parameter in meters following from the functions in Equation 6.3. In this set of equations, Λ_{U} is the turbulence scale parameter and z_{hub} is the hub height [63].

$$L = 3.5\Lambda_{\rm U}$$
 $\Lambda_{\rm U} = 0.7 {\rm min} (30, z_{\rm hub})$ (6.3)

The International Electrotechnical Commission has several standards for wind turbine design and analysis. IEC 61400-1 is intended for modern multi-megawatt wind turbines, IEC 61400-2 for small wind turbines and IEC 61400-3 for offshore wind turbines [48]. Straightforwardly, IEC 61400-1 is chosen. The tuning parameter in this part of the research is the now well-known turbulence intensity TI, inputted in TurbSim in percentages. Values for TI are chosen based on the observed inaccuracies originating from the LiDAR met mast comparison in Chapter 5 and the regular range in which the measured μ_{TI} values lie for sites like "Windplan Blauw". The above comprises of the interval between 0.07 and 0.11 for the wind site under attention.

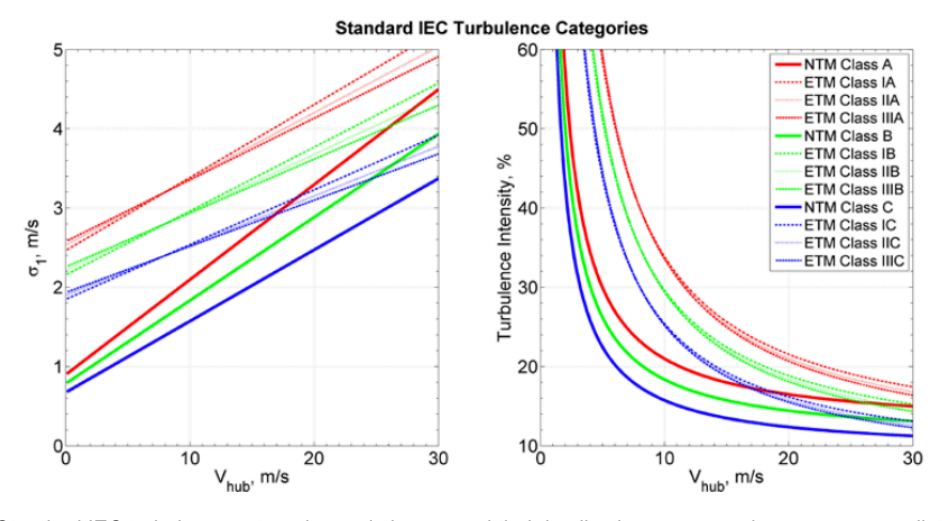


Figure 6.2: Standard IEC turbulence categories and classes and their implications on TI and $\sigma_{\rm u}$ versus $U_{\rm hub}$ distributions [4]

There are several IEC turbulence classes at disposal in TurbSim, which are all depicted in the graph on the right hand side of Figure 6.2. The consequence of the TI versus wind speed at hub height $U_{\rm hub}$ fit for each turbulence class on $\sigma_{\rm u}$ is shown on the left. Since one is obliged to use the Normal Turbulence Model (NTM) when having assigned values to the above-mentioned IEC Turbulence, this model is used. This model would have been chosen anyway, since NTM Class C approaches the situation at "Windplan Blauw" the closest, which can be confirmed by observing Figure 5.10.

The reference height $z_{\rm ref}$ and reference wind speed $u_{\rm ref}$ are taken from LiDAR met mast pair 1 measurements in Subsection 5.2.1, $u_{\rm ref}$ being the average of both devices. Both are input for the chosen wind profile in TurbSim, which can be a power-law profile as posed in Equation 2.1, a logarithmic profile as posed in Equation 2.3 or a wind profile that TurbSim calls IEC. The latter is a combination of both wind profiles, where the power law is applied over the rotor disk and the logarithmic law is applied elsewhere. This is considered the wind profile most accurately representing reality and is therefore chosen. To use both laws, power law or shear exponent α and surface roughness length z_0 have to be chosen in line with the wind conditions at the site. Using the measurements from LiDAR met mast pair 1, both are determined via the earlier mentioned equations introduced in Subsection 2.1.1.

TurbSim output - The run-time options and the above explained turbine/model specifications and meteorological boundary conditions constitute the content of the input file (with extension .inp) for TurbSim to run and output a file in the form of full-field TurbSim binary time-series data with the extension .bts. Other forms and accompanying extensions are possible too, but since FAST requires an input in the form of a binary file, this type is chosen. A visualization of a typical TurbSim output is depicted in Figure 6.3.

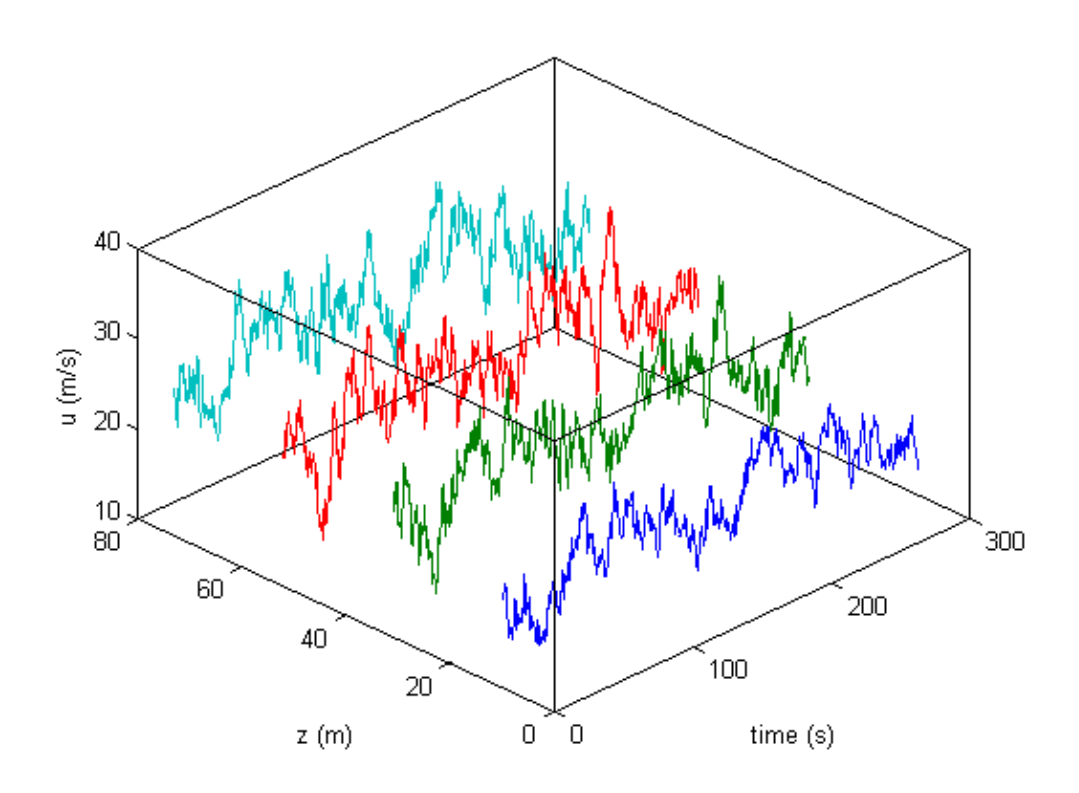


Figure 6.3: Visualization of an example output of full-field binary time-series data derived from TurbSim of the horizontal u component of the wind speed at different heights z [11]

6.1. Method 59

6.1.2. Performing aeroelastic simulations in FAST

About FAST and its general working - FAST, which is an abbreviation for Fatigue, Aerodynamics, Structures and Turbulence, is a comprehensive aeroelastic simulator developed by NREL and is used extensively to predict fatigue loads of three-bladed horizontal-axis wind turbines, among other options like extreme loads and two-bladed wind turbines. Next to that, it gives the possibility to extract ADAMS (Automatic Dynamic Analysis of Mechanical Systems) wind turbine data sets, to use Aerodyn simulation and to connect FAST to the MATLAB and/or Simulink interface. More information on these options and the general working can be found here [65].

FAST has two different modes of operation: simulation and linearization. The time-marching of the nonlinear equations of motion, or simulation, determines the aerodynamic and structural response of a wind turbine in time due to certain wind-inflow conditions. This is the mode of operations that will be used; the linearization option will be neglected. The output of the simulation comprises of time series data on the aerodynamic loads and moments on the relevant parts of the wind turbine, which will be explained in more detail below. These outputs are used to calculate the fatigue loads of the wind turbine with the help of the MLife tool, as described in Subsection 6.1.3. Figure 6.4 gives an overview of the possibilities of the FAST software package and how different parts of the system interact with each other.

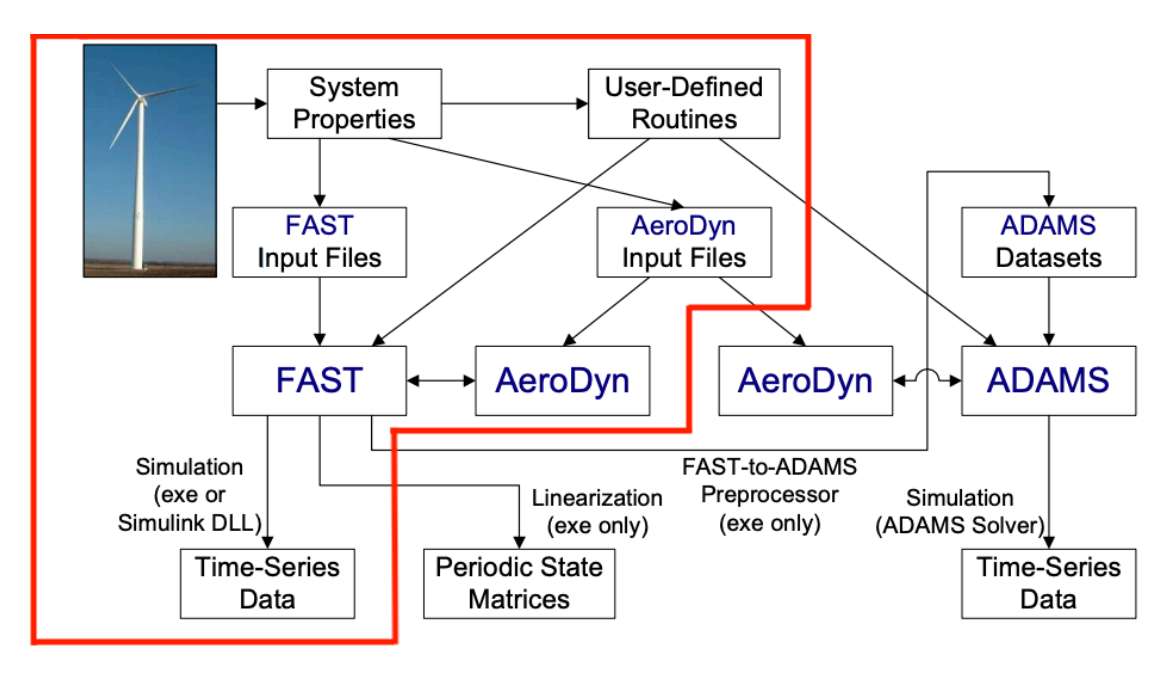


Figure 6.4: General working of FAST, with the relevant parts for use in this research in the red box [65]

FAST primary input - FAST uses several input files originating from the system properties and the user-defined routines, as can also be extracted from Figure 6.4. A primary input file with .fst extension is required to run FAST. This primary input file consists of six sections. The first is the simulation control section, where things like total run time, time step and interpolation order are defined. The second section comprises of the feature switches and flags, where the input files of the third section can be switched on and off via Boolean variables. The input files are elaborated on below. In the fourth section, the output file format and extensions of the FAST simulation is specified. The output comes in the form of binary time-series data of loads with .outb extension, to be read by MLife in the third step of this analysis. In the fifth and sixth section, linearization and visualization variables can be set. These are not used and not further discussed. Appendix E includes one of the FAST input files that is used in this analysis.

Other input files - In section two of the primary input file, the feature switches and flags can be set to include or exclude the other input files. These switches and their accompanying input files from the third section are listed below, along with a description of what the purpose is of this file.

Feature switch	On/Off	Purpose	Input file(s)
CompElast	On	Structural dynamics	ElastoDyn.dat
CompInflow	On	Inflow wind velocities	Turbsim.bts
CompAero	On	Aerodynamic loads	AeroDyn.dat
CompServo	Off	Control and electrical dynamics	-
CompHydro	Off	Hydrodynamic loads	-
CompSub	Off	Sub-structural dynamics	_
CompMooring	Off	Mooring system	-
Complce	Off	Ice loads	-

Table 6.2: Overview input parameters and files for FAST simulation

The inflow wind velocities and conditions are simply the wind fields generated by TurbSim in the form of the earlier discussed .bts file, explained in Subsection 6.1.1. The AeroDyn.dat file contains aerodynamic input properties like the inclusion of stall, aerodynamic pitching moment model, potential wake effects, tip- and hub-loss models and tower shadow, among some other less important properties.

The ElastDyn.dat file firstly includes an extensive list of degrees of freedom and initial conditions of the chosen turbine. The degrees of freedom comprise of flapwise and edgewise blade modes and fore-aft and side-to-side tower bending modes. The initial conditions basically define that the whole turbine is in the default position when the simulation starts. Next to that, the turbine configuration is specified. The basic dimensions of the blades, like number, length and cone angle, and the nacelle, hub and tower are specified here. Thereafter, the mass and inertia section specifies the hub and nacelle mass and inertia. Next to that, the rotor-teeter, drive train and furling section are not used and therefore not discussed. Two important sections are left: the tower and blades section. These simply comprise of other input files defining the pitch twist, mass, stiffness and mode shapes for each of the three blades and the mass, stiffness and mode shapes of the tower. Finally, a summary of the output parameters of the structural dynamics analysis can be predefined. This firstly includes out-of-plane deflections, in-plane deflections, edgewise bending moments, flapwise bending moments and tip twist of the blades. Next to that, axial forces, bending and pitching moments at the blade roots are outputted. Ultimately, bending, shear, and forces at the tower are part of the output.

This analysis does not focus on the electrical components in the drive train of the wind turbine nor on the control elements associated with this part of the turbine. Therefore, this part is not altered in the FAST simulation and not further touched upon. Since an onshore wind turbine is considered, hydrodynamic loads nor a mooring system apply to this analysis. Lastly, icing of the turbine and sub-structural dynamics are out of the scope of this research.

After the input of the primary files containing all the other above described files, time-series data of loads and moments on blades and tower are obtained via simulation, to be used in the next step of this analysis in MLife.

NREL baseline turbine - FAST is equipped with several default wind turbines and accompanying sets of input files. These range from two-bladed turbines with rated power of 175 kW to three-bladed turbines with a rotor diameter of 70 m to several 5 MW onshore, offshore and floating wind turbines [64]. Since the aeroelastic simulations in FAST require extensive amount of blades, hub, nacelle and tower input specifications, it is a precise and time-consuming work to gather and order all input parameters for a certain wind turbine.

6.1. Method 61

Of all possible predefined turbines, the NREL 5 MW baseline onshore wind turbine is chosen to be used in this simulation. The fact that this turbine is used and not another e.g. 4 MW wind turbine is done for two reasons. The first reason is that the NREL 5 MW baseline onshore wind turbine has relatively similar gross specifications compared to the wind turbines that are planned to be commissioned at wind farm "Windplan Blauw". These latter turbines are planned to have a rated power of 4 MW and a hub height of around 100 m. The second reason is the simple fact that it is yet unknown which exact turbines will be commissioned at "Windplan Blauw" and it is therefore impossible to retrieve the required extensive and exact specifications of all turbine components. The gross specifications of the chosen turbine are summarized in Table 6.3. The structural and aerodynamic properties of the blades, the properties of the hub, nacelle, drivetrain, tower and the control system of the turbine are explained in minor detail in [64].

Rated power	5 MW	Cut-out wind speed	25 m/s
Rotor orientation	Upwind	Cut-in rotor speed	7 rpm
Rotor configuration	3 blades	Rated rotor speed	12 rpm
Control	Variable speed	Rated tip speed	80 m/s
Drive train	Multiple-stage gearbox	Overhang	5 m
Rotor diameter	126 m	Shaft tilt	5°
Hub diameter	3 m	Precone	2.5°
Hub height	90 m	Rotor mass	111,000 kg
Cut-in wind speed	3 m/s	Nacelle mass	240,000 kg
Rated wind speed	11.4 m/s	Tower mass	347,500 kg

Table 6.3: General specification of the widely used 5 MW baseline wind turbine developed for research purposes by NREL [64]

Definition of tower and blade gauges - FAST allows users to attach virtual strain gauges at different nodes on the blades and tower of a wind turbine. The placement of these strain gauges mark the spots where time series data of forces and moments are collected. Six nodes with strain gauges were placed along the 87.6 m high turbine tower and five nodes along the 61.5 m long blades. Next to that, strain gauges are present at the tower base and blade root. Table 6.4 depicts the exact location measured from tower base and blade root.

#		1	2	3	4	5	6
Tower	0	11.5	25.4	39.2	53.0	66.9	80.7
Blades	0	11.5	23.1	34.6	46.1	57.7	

Table 6.4: Placement of strain gauges in terms of distance in meters from tower base and blade root

FAST output and processing thereof - Where the desired input for the MLife software package in step three would consist of stresses on several parts of the wind turbine, FAST only outputs time series of (bending) moments M (and forces F) at predefined points on the blades and tower, including blade root and tower base. These bending moments are therefore first translated to stresses σ by means of Equation 2.19, which was introduced and elaborated on in combination with the cantilever beam model of a wind turbine in Subsection 2.4.

For the blade root and the turbine tower, the area moment of inertia or second moment of inertia $I_{\rm x}$ is determined by considering the shape of the blade root and tubular tower as one of an annulus. This is a hollow circular and symmetrical object with inner radius r_1 and outer radius r_2 , as the composite blade root and steel tower are [123]. An underlying assumption for this approach is the one that the material of the annulus is uniform. Where the tower meets this assumption, the blade root violates this assumption since steel joints are present throughout the composite structure. Nevertheless, this is ignored for the sake of simplicity. Keeping this annular circular shape in mind, an expression for $I_{\rm x}$ as depicted in Equation 6.4 can be formulated.

$$I_{x} = I_{y} = \frac{\pi}{4} \left(r_{2}^{4} - r_{1}^{4} \right) \tag{6.4}$$

6.1.3. Fatigue lifetime determination with help of MLife

About MLife and its general working - MLife is a MATLAB based tool developed by NREL to post-process dynamic aeroelastic simulations of the loads and moments on different parts of a wind turbine, like the ones performed in FAST in this research. From an input settings file and one or more files containing time series of loads, MLife computes statistical information and fatigue estimates. Wind engineers usually have to perform loads analysis to gain type certification of a wind turbine, which can involve running thousands of simulations modeling different conditions. Consequently, extreme-event tables and fatigue-life predictions have to be generated from the simulation output, which comprises of a lot of work. This can also be done automatically by MLife, which immediately exposes the big advantage of this tool. Before diving into the more detailed working of the MLife tool, a general outline of the processing steps within MLife is presented below [57].

- 1. Compute aggregate statistics across all processed input files
- 2. Determine the fatigue cycles for each time series by means of rainflow counting
- 3. Compute the short-term damage-rates and damage-equivalent load (DEL) of each timeseries
- 4. Sum the damage contribution of each time-series to determine short-term aggregate damage-rates and DELs
- 5. Extrapolate the damage contribution of each time-series across the design lifetime to determine the lifetime damage
- 6. Determine the lifetime DEL and compute the time until failure

Input parameters MLife - Several inputs are required for the working of MLife. To start, a wind speed binning procedure based on a Weibull distribution as introduced in Section 5.2 is included in the tool, fed by provided inputs for mean horizontal wind speed \overline{U} , Weibull scale parameter a and Weibull scale parameter k. These are all based on the LiDAR measurements from Chapter 5. Secondly, turbine related input parameters are defined: cut-in wind speed $U_{\rm in}$, cut-out wind speed $U_{\rm out}$, availability factor A (The percentage of time a wind turbine is available. A value of A=1 indicates that the turbine is always in operation and producing power for all $U_{\rm in} < U < U_{\rm out}$.) and the design lifetime of the turbine $T_{\rm life}$. Since MLife follows the techniques outlined in Annex G of IEC 61400-1 edition 3, three different Design Load Case (DLC) classifications are included:

- Power Production (IEC DLC 1.2): turbine is in normal operation between U_{in} and U_{out}
- Parked (IEC DLC 6.4): turbine is idling or parked since U is not between $U_{\rm in}$ and $U_{\rm out}$
- Discrete Events (IEC DLCs 2.4, 3.1, and 4.1): events that occur a defined number of times over the turbine design lifetime

So lastly, for each Design Load Case a representative input file exists, which gives a total of three input files in the form of time series of loads on several parts of the turbine as generated in FAST. MLife extrapolates the damage cycle counts in a different way for each DLC classification of the time series. Encompassing the three above mentioned DLCs ensures that all DLCs contributing to fatigue damage are included.

Background theory fatigue lifetime calculations - To understand the working of MLife, one must understand the underlying principles of lifetime damage calculations. MLife accumulates fatigue damage caused by fluctuating loads over the design lifetime of a wind turbine. By matching local minimums with local maximums in the time series, the fluctuating loads are broken down into individual hysteresis cycles. This method is called rainflow counting and assumes damage accumulates linearly with each of these cycles according to the Palmgren-Miner Rule [96]. The total lifetime damage $D_{\rm life}$ of all hysteresis cycles is given by Equation 6.5,

6.1. Method 63

$$D_{\text{life}} = \sum_{i} \frac{n_{i}^{life}}{N_{i}} \tag{6.5}$$

where n_i^{life} is the cycle count and N_i denotes the amount of cycles until failure. In general, approaching the value of D=1 indicates failure of the material. The relationship between the amount of cycles until failure N_i and the loads and accompanying stresses on the wind turbine follows a so-called S-N curve, of which an example is shown in Figure 6.5. It depicts the relationship between N and S of different commonly used materials like steel and fiber reinforced plastic on a logarithmic scale.

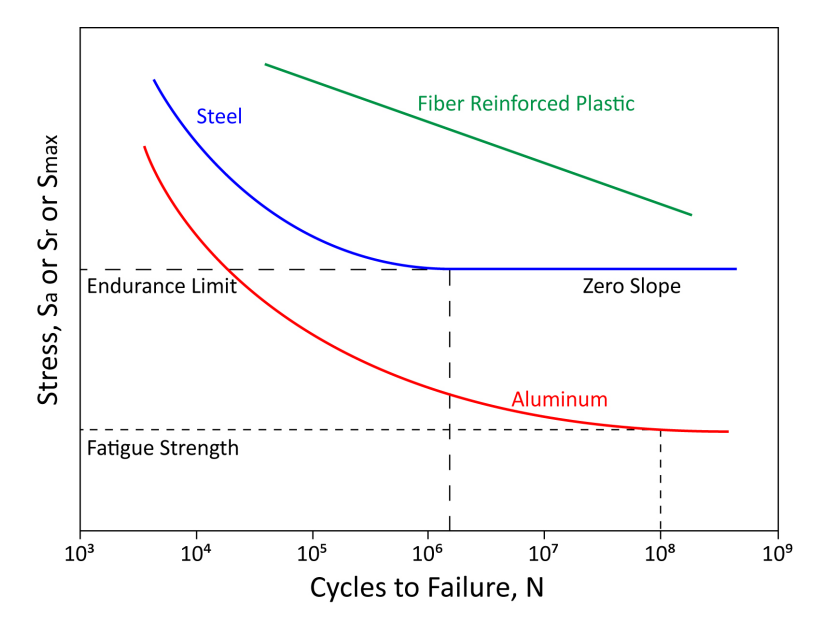


Figure 6.5: S-N or Wöhler curve for three different materials [52]

The S-N curve, also known as a Wöhler curve, is often used to characterize materials performance in high-cycle fatigue situations, e.g. wind loads on a rotating wind turbine [96]. These curves are derived from tests on material samples where constant sinusoidal stresses are applied by testing machines, counting the amount of cycles until failure. The relationship can be modelled by means of Equation 6.6,

$$N_{\rm i} = \left(\frac{L^{\rm ult} - |L^{\rm MF}|}{\frac{1}{2}L_{\rm i}^{\rm RF}}\right)^m \tag{6.6}$$

in which $L^{\rm ult}$ is the ultimate design load of the component under attention, $L^{\rm MF}$ is the fixed mean of the load and m is a material specific parameter called the Wöhler exponent. Equation 6.6 assumes that the fatigue cycles occur over a constant mean of the load, where in reality the fatigue cycles will occur over a range of means. To solve this in-exactitude, a correction named after himself is proposed by Goodman [47]. This is a formula that provides a correction to analyze the data as if each cycle occurs about that fixed mean load, explains the origin of $L^{\rm RF}_{\rm i}$ and is given by Equation 6.7. $L^{\rm RF}_{\rm i}$ itself represents the cycle's load range around the fixed mean of the load and $L^{\rm R}_{\rm i}$ is the $i^{\rm th}$ cycle's range around the fixed load mean $L^{\rm MF}_{\rm i}$. Where $L^{\rm ult}$ is material dependent, $L^{\rm MF}_{\rm i}$ and $L^{\rm RF}_{\rm i}$ are a consequence of the loads and moments that are applied on a certain material.

$$L_{i}^{RF} = L_{i}^{R} \left(\frac{L^{\text{ult}} - |L^{MF}|}{L^{\text{ult}} - |L_{i}^{M}|} \right)$$

$$(6.7)$$

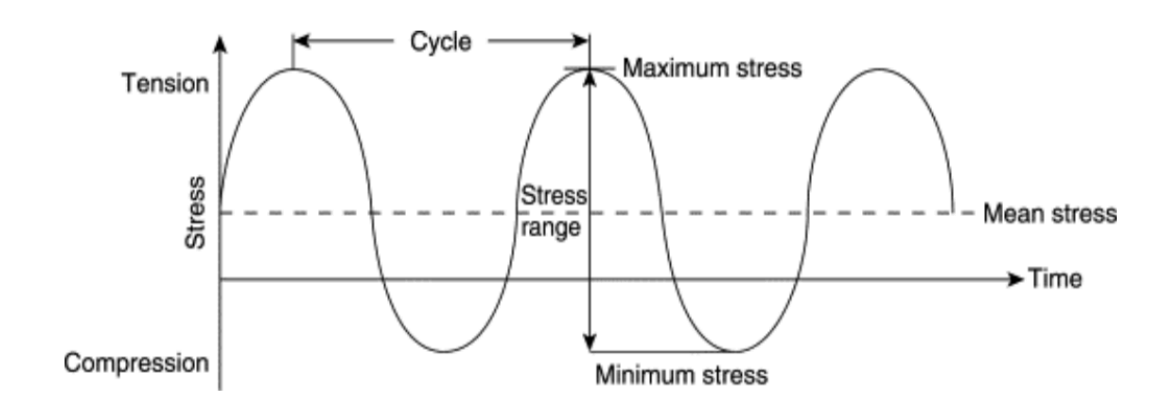


Figure 6.6: Simplified visualization of a load cycle with mean stress and stress range [78]

In Figure 6.6, a simplified load cycle is presented. The mean stress, directly related to $L^{\rm MF}$ and $L^{\rm M}$ in Equations 6.6 and 6.7 is indicated, as well as the stress range, which is in turn related to $L^{\rm RF}$ and $L^{\rm R}$ in Equations 6.6 and 6.7. It should be noted that in reality and from simulation in FAST, several load cycles are retrieved, which in itself do not have a fixed amplitude over time and therefore also not a constant stress range. To clarify the interchangeable use of the terms loads and stresses in this section, one is remembered of the relationship between both. Load L is another word for force, measured in Newton and also often expressed using F, and stress S is simply the load or force per area A in N/m^2 , following Equation 6.8.

$$S = \frac{L}{A} \tag{6.8}$$

As stated earlier in this section, the time series that are used cover a much shorter time period than the design lifetime $T_{\rm life}$ of a turbine. Throughout this analysis, a time period of 600 seconds is used as a basis for further analysis. From a practical point of view, the lifetime damage $D_{\rm life}$ is estimated by extrapolation of these time series over the design lifetime. This will result in a time until failure $T_{\rm fail}$, calculated according to Equation 6.9.

$$T_{\text{fail}} = \frac{T_{\text{life}}}{D_{\text{life}}} \tag{6.9}$$

Last specifications MLife simulations - Certain other input parameters are required for the fatigue lifetime calculations which take place in the MLife simulations. Firstly, the design wind turbine lifetime $T_{\rm life}$ is considered. The lifetime of a modern multi-megawatt turbine is assumed to be 20-25 years in wind energy industry. Although it is often heard that wind turbines can stay in operation and stay profitable up until or even over 30 years, this is relatively unsure since the vast majority of the currently installed multi- megawatt turbines have not reached the age of 30 yet [66]. On the other hand, some research revealed that onshore wind turbines might only generate electricity effectively for 15 years on average. It is chosen to reason from a conservative lifetime $T_{\rm life}$ of 20 years.

As stated above, $L^{\rm MF}$ and $L^{\rm RF}$ are a consequence of the loads and moments that are exerted on different parts of the wind turbine. A certain mean can be found in the cycle of loads and moments, as well as a certain range around that mean.

Lastly, there are two other variables in the process described in this Subsection that are indispensable: the Wöhler exponent m and ultimate load or moment $L^{\rm ult}$. Both are material dependent and commonly hard to define exactly, which results in the fact that often a range of Wöhler exponents (and Wöhler curves) and $L^{\rm ult}$ is used throughout research regarding fatigue determination. For the Wöhler exponent, in contrast to $L^{\rm ult}$, this is adopted in this research.

Three different values are used for the steel in the turbine tower, as well as for the glass-fiber reinforced plastic of which the blades and blade roots consist. Values for m of 3,4 and 5 for steel and 8, 9 and 10 for glass-fiber are widely used in this setting and therefore adopted [45]. The $L^{\rm ult}$ that are used for steel and fiberglass are derived from the yield strength (or yield stress) of both materials, which are 250 MPa and 2 GPa respectively [64]. The yield strength is the point until where the stress-strain relationship of a material shows linear behavior and up to which deformations of the material are completely recoverable upon removal of the force induced stress [108]. Finally, Equation 2.19 is used to convert these stress values into moments.

6.1.4. Method overview

From structural model to fatigue lifetime determination - To conclude this section on the three-step method used for the sensitivity analysis on the fatigue lifetime of a common Dutch onshore wind turbine as a function of turbulence intensity, a flowchart is presented in Figure 6.7. The first two elements depict the structural model of the NREL 5 MW baseline wind turbine and the via aeroelastic simulation obtained time-series data of loads and moments on the wind turbine in FAST, respectively. The next three elements, elaborated on in the above subsection, are carried out in MLife and lead to the ultimate goal of determining the fatigue lifetime for several parts of the wind turbine. They consist of rainflow counting of the to stresses converted moments, histograms containing stress ranges in ascending order and the use of Equations 6.5 to 6.7 to arrive at lifetime damage $D_{\rm life}$ and time until failure $T_{\rm fail}$.

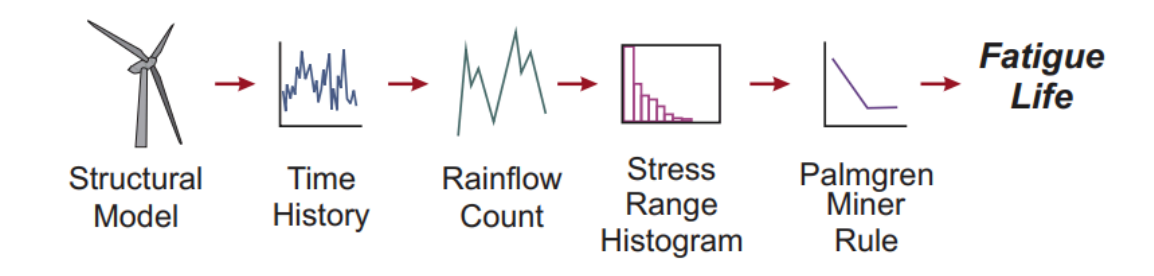


Figure 6.7: Overview conceptual working of FAST and MLife

6.2. Results

The results of the in the preceding section explained three-step procedure are presented in this section. First, a few interim results from the first and second step are shown in Subsection 6.2.1 to increase the acquaintance with and understanding of these parts. Thereafter, the final results derived from MLife are presented in Subsection 6.2.2.

6.2.1. Interim results

TurbSim output - TurbSim software normally outputs full-field time-series data of wind fields in binary form, which can not be read by any program. However, one can also request an output of wind speed component vectors u, v and w as an array in a readable text file. Figure 6.8 depicts an interval of 600 seconds out of the total simulation time of 6000 seconds of the horizontal wind speed component u with turbulence intensity TI values of 0.07 and 0.11 (7% & 11% in TurbSim). TurbSim outputs all three wind speed component vectors at 30 heights and widths according to the wind field grid settings, as discussed in 6.1.1. Wind speeds between 10 and 170 m height are available with these settings. Figure 6.8 represents the horizontal wind speed at a height of 90 m at the centre of the rotor plane. A fluctuating pattern in u can be observed for both TI values, albeit more explicitly for TI = 0.11. The mean wind speed \overline{U} , which is indicated by the dotted line, is the same for each wind field, namely 8.08 m/s at 90 m height, but the spread varies according to the different values for TI.

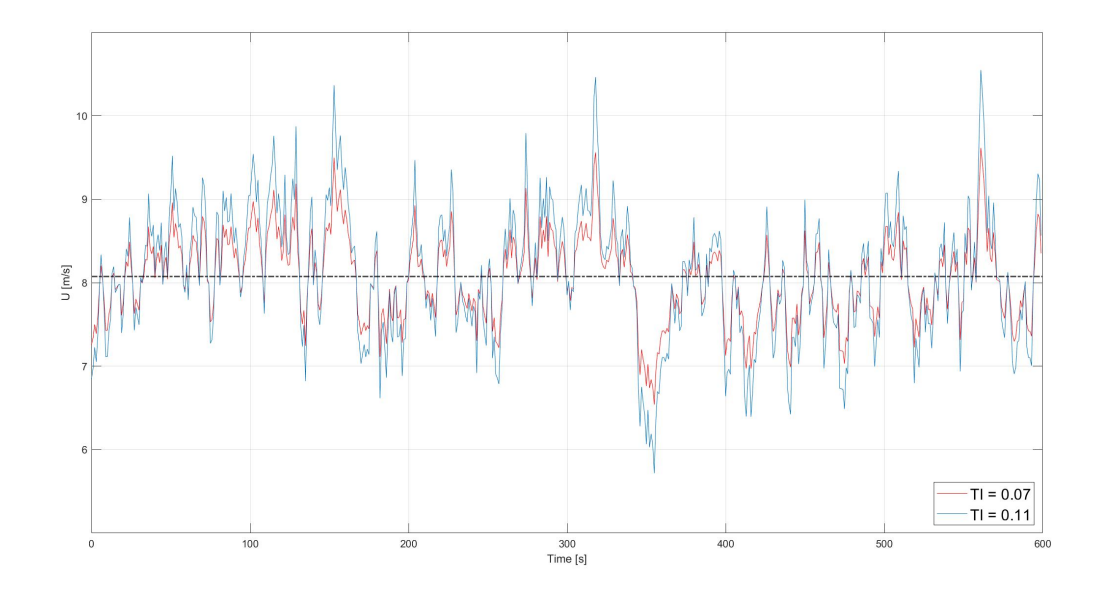


Figure 6.8: Horizontal wind speed component \boldsymbol{u} at the rotor hub of the NREL baseline turbine

FAST output - The aeroelastic simulations performed in FAST result in time-series data of bending moments for different parts of the NREL 5 MW baseline turbine. Different nodes at the turbine tower and blades are considered, including tower base and blade root. Not all results are shown here, but a selection is made. The same time series of 30 seconds between 15 and 45 seconds as for Figure 6.8 is picked from a total simulation time of 600 seconds.

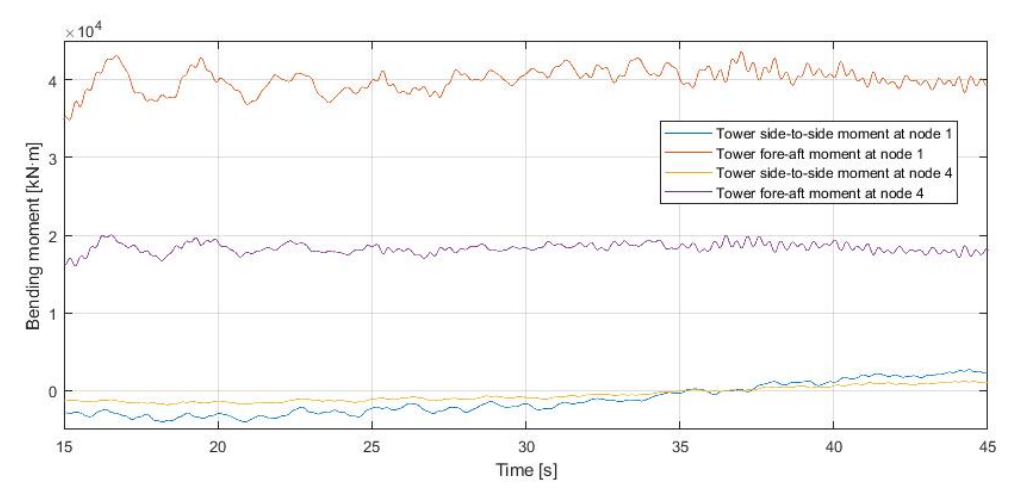


Figure 6.9: Tower bending moments at two different tower nodes for TI = 0.09

Figure 6.9 shows the side-to-side and fore-aft bending moments of the turbine tower at two different heights for TI = 0.09. Node 1 is located quite close to the ground at 11.5 height, where node 4 is placed at 53 m height. The fore-aft bending moments are an order of magnitude higher than the side-to-side bending moments for both nodes. This is logical behavior, since the wind exerts by far more force on the turbine perpendicular to the rotor plane, then it exerts forces on the sides of the turbine. Next to this, it is noteworthy that no clear patterns can be observed in the tower bending moments. The values tend to fluctuate minorly around certain values. Furthermore, it can be observed that the fore-aft bending moment at node 1 is considerably higher than the fore-aft bending moment at node 4, higher up the tower. The lower parts of the turbine tower naturally have higher bending moments compared to higher up the tower.

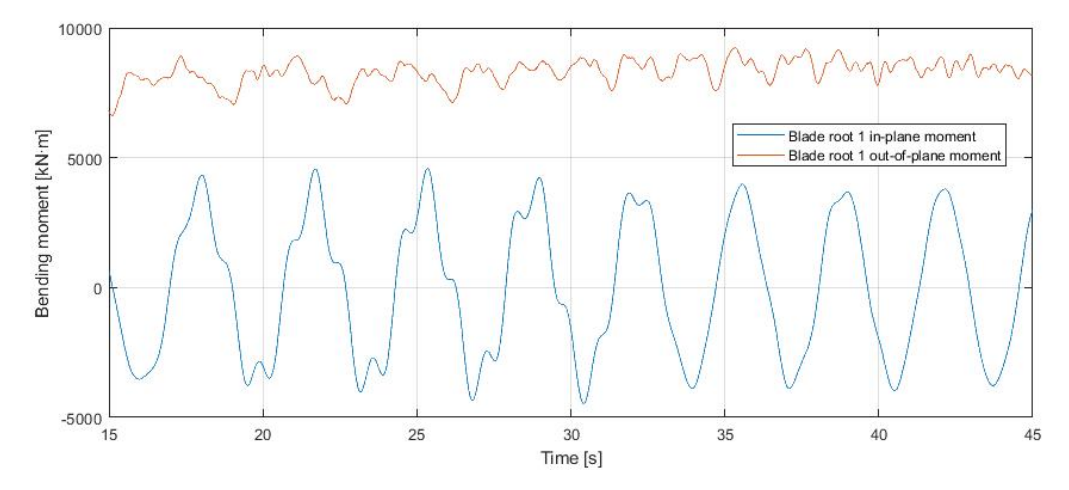


Figure 6.10: Blade root bending moments for TI = 0.09

Figures 6.10 and 6.11 depict the bending moments on two parts of the blades for TI = 0.09. Figure 6.10 shows the measured moments at the blade root, where 6.11 shows the moments 5 m from the tip of the blade at node 5. It can be noticed that the out-of-plane bending moments (called flapwise moments for the blade) are higher than the in-plane moments and their cycles tend to have smaller amplitudes than the in-plane moments. Furthermore, the cycles of the in-plane moments fluctuate around a zero mean, where the cycles of the out-of-plane moment do not show this characteristic. The above described behavior aligns with the fact that the forces that the wind exerts on the rotor plane are mostly coming from a forward direction. The blue lines, representing the in-plane/edgewise bending moments on the blades, reflect the forces of gravity on the wind turbine blades, as the blades are alternately located in the right-hand and left-hand plane. This causes the sign of the in-plane moments to alternate between plus and minus. Finally, it can be observed that the bending moments at the blade root are an order of magnitude higher than those close to the blade tip. The blade roots naturally undergo the highest bending moments since all forces on the blade converge to this point.

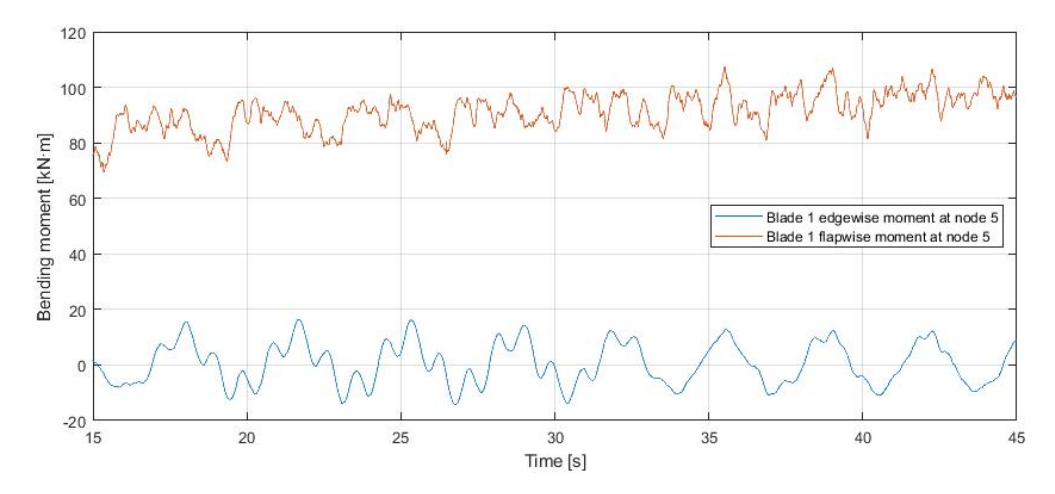


Figure 6.11: Blade bending moments for TI = 0.09

Visualization of the bending moments or forces on other the nodes on the turbine tower and blades are not shown here, nor are these shown for other *TI* values. Nevertheless, the outcome for these variables aligns with the observed behavior that is described above.

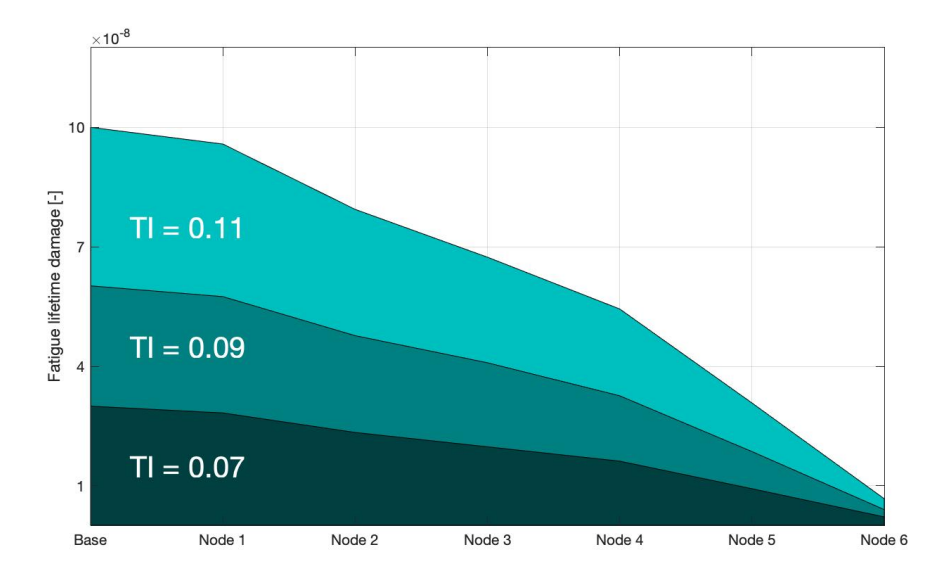
6.2.2. Final results

This subsection presents the results for the fatigue lifetime assessment executed with the help of MLife on different parts of the NREL 5 MW baseline turbine, to know the entire span of the blades and the tower from base to top. Simulations and calculations in FAST and MLife were performed for $TI = [0.07\ 0.08\ 0.09\ 0.10\ 0.11]$, but for reasons of conciseness only the results for the wind fields with $TI = [0.07\ 0.09\ 0.11]$ are presented in the tables in this section. Several graphs visualize the numerical findings for Wöhler exponents $m = [3\ 4]$ for the steel tubular tower and $m = [8\ 9]$ for the glass fibre blades, since these are the most used values for m in literature for the NREL 5 MW wind turbine [64].

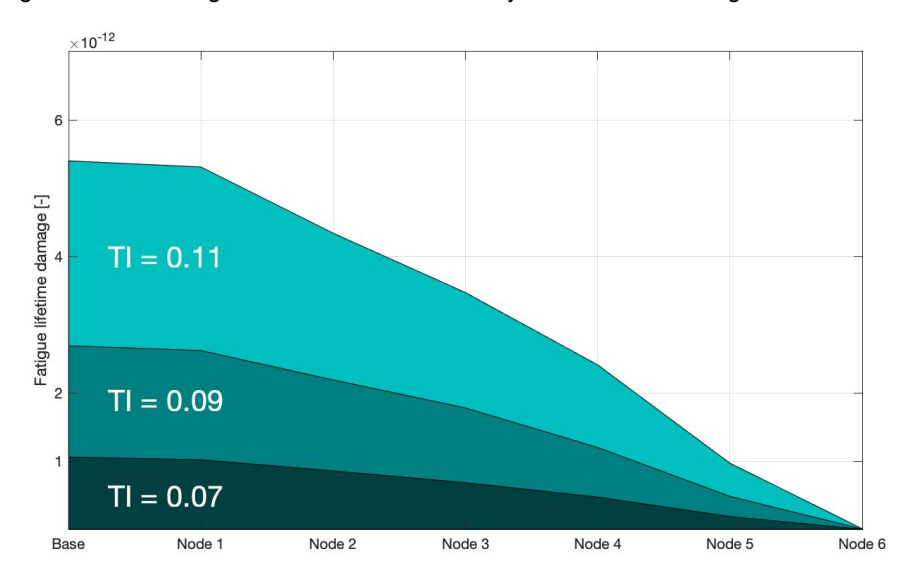
Fatigue lifetime turbine tower - Table 6.5 summarizes the results obtained from MLife for three TI dictated wind fields regarding lifetime fatigue damage of the wind turbine tower calculated according to Equations 6.5, 6.6 and 6.7. This was done for 7 nodes along the tower, including the tower base. The location of these nodes is discussed in Subsection 6.1.2. For lay-out purposes, only 5 nodes are depicted in Table 6.5. Fatigue damage due to stresses from side-to-side bending moments are presented, as well as fatigue damage due to stresses from fore-aft bending moments. As stated before, a set of three Wöhler exponents m is used for each TI dictated wind field. Figures 6.12 and 6.13 visualize the obtained results for m = [3 4] for stresses caused by side-to-side bending moments and fore-aft bending moments, respectively.

Stresses from	$\mid m \mid$	Base	Node 1	Node 3	Node 4	Node 6
Side-to-side bending moments for <i>TI</i> = 0.07	3 4 5	3.00×10^{-8} 1.06×10^{-12} 4.28×10^{-17}	2.83×10^{-8} 1.02×10^{-12} 4.27×10^{-17}	1.98×10^{-8} 6.64×10^{-13} 2.57×10^{-17}	1.62×10^{-8} 4.73×10^{-13} 1.58×10^{-17}	2.20×10^{-9} 1.94×10^{-14} 2.43×10^{-19}
Fore-aft bending moments for <i>TI</i> = 0.07	3 4 5	8.89×10^{-6} 2.61×10^{-9} 8.54×10^{-13}	8.13×10^{-6} 2.41×10^{-9} 7.77×10^{-13}	5.82×10^{-6} 1.59×10^{-9} 4.66×10^{-13}	4.09×10^{-6} 9.29×10^{-10} 2.37×10^{-13}	7.80×10^{-7} 3.83×10^{-11} 2.95×10^{-15}
Side-to-side bending moments for <i>TI</i> = 0.09	3 4 5	6.02×10^{-8} 2.69×10^{-12} 1.39×10^{-16}	5.75×10^{-8} 2.60×10^{-12} 1.37×10^{-16}	4.09×10^{-8} 1.78×10^{-12} 8.36×10^{-17}	3.26×10^{-8} 1.20×10^{-12} 5.02×10^{-17}	4.03×10^{-9} 4.19×10^{-14} 6.29×10^{-19}
Fore-aft bending moments for <i>TI</i> = 0.09	3 4 5	9.72×10^{-6} 2.74×10^{-9} 8.92×10^{-13}	8.64×10^{-6} 2.51×10^{-9} 8.07×10^{-13}	6.12×10^{-6} 1.65×10^{-9} 4.83×10^{-13}	4.52×10^{-6} 9.77×10^{-10} 2.47×10^{-13}	1.24×10^{-6} 6.15×10^{-11} 4.62×10^{-15}
Side-to-side bending moments for <i>TI</i> = 0.11	3 4 5	1.00×10^{-7} 5.40×10^{-12} 3.29×10^{-16}	9.58×10^{-8} 5.37×10^{-12} 3.28×10^{-16}	6.74×10^{-8} 3.47×10^{-12} 1.92×10^{-16}	5.44×10^{-8} 2.41×10^{-12} 1.21×10^{-16}	6.76×10^{-9} 8.55×10^{-13} 1.58×10^{-18}
Fore-aft bending moments for <i>TI</i> = 0.11	3 4 5	1.08×10^{-5} 2.93×10^{-9} 9.44×10^{-13}	9.30×10^{-6} 2.64×10^{-9} 8.45×10^{-13}	6.50×10^{-6} 1.72×10^{-9} 5.04×10^{-13}	5.08×10^{-6} 1.04×10^{-9} 2.60×10^{-13}	1.85×10^{-6} 9.77×10^{-11} 7.51×10^{-15}

Table 6.5: Results obtained for tower lifetime fatigue damage calculations in MLife for three TI values, three Wöhler exponents m and due to stresses from side-to-side bending moments and fore-aft bending moments



(a) Fatigue lifetime damage due to stresses caused by side-to-side bending moments for m = 3

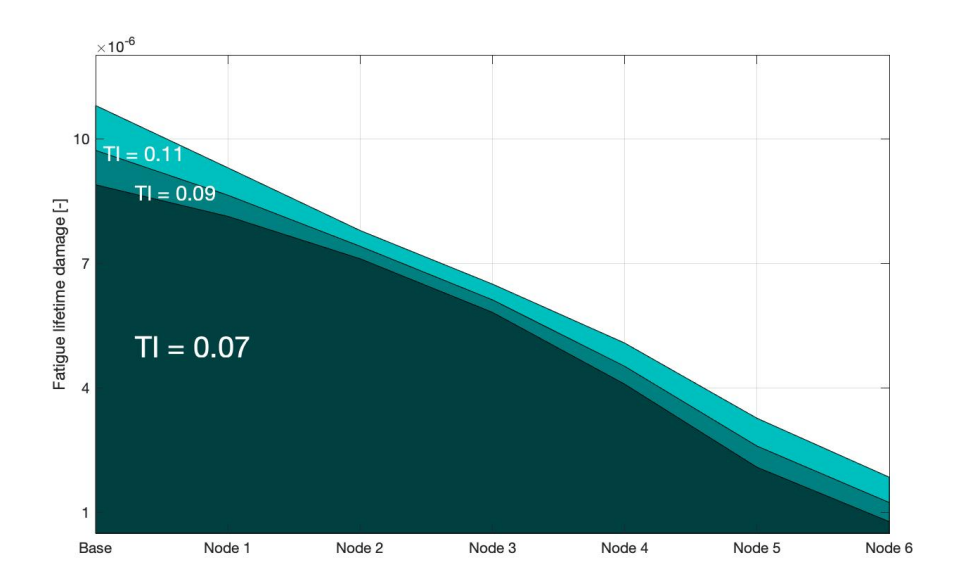


(b) Fatigue lifetime damage due to stresses caused by side-to-side bending moments for m = 4

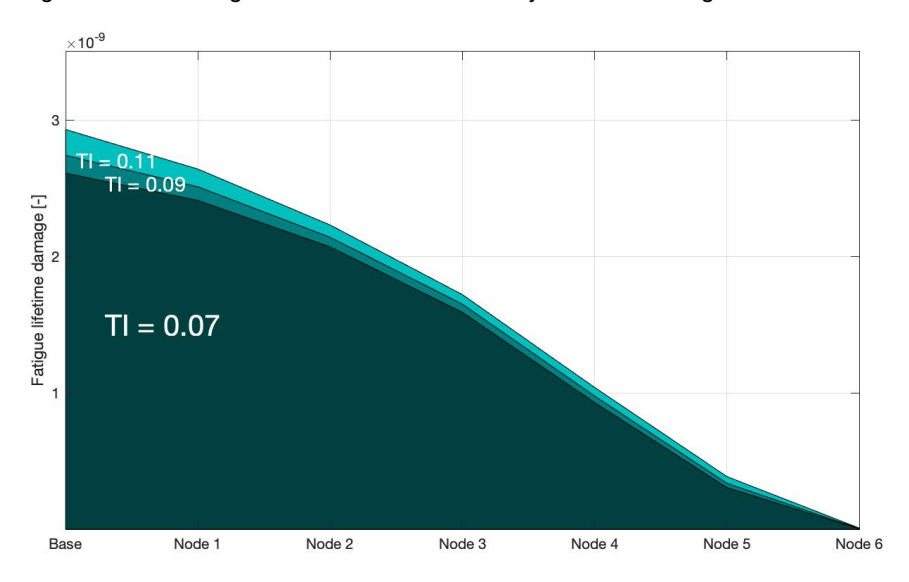
Figure 6.12: Results of MLife calculations for fatigue lifetime damage of the tower for three values of TI

A number of patterns and certain behavior can be extracted from the results in the table above and both graphs. Firstly, the fatigue damage at the turbine tower decreases with increasing height from the tower base towards the top for every TI value and m. This seems logical for two reasons. In the first place because stresses are mainly caused by the variability of wind (speed) and this turbulence decreases with height too. Subsequently, the lower parts of the turbine tower are exposed to more and heavier loads than the upper parts because of two reasons. On the one hand, these lower parts have to carry more weight of the remainder of the turbine above them. On the other hand and most important, their lever arm in the cantilever beam model is longer. Moreover, it seems that this relationship is non-linear. In other words, the fatigue damage decreases faster per meter height higher up the tower.

Thirdly, the fatigue damage due to stresses from fore-aft moments is higher than that due to stresses from side-to-side bending moments. As already mentioned in Subsection 6.2.1, this behavior is expected since aerodynamic loading on a wind turbine caused by the u component of the wind speed is the highest, since the purpose of a horizontal axis wind turbine is to align perfectly with the wind to generate as much thrust as possible via Equation 2.16.



(a) Fatigue lifetime damage due to stresses caused by fore-aft bending moments for m = 3



(b) Fatigue lifetime damage due to stresses caused by fore-aft bending moments for m = 4

Figure 6.13: Results of MLife calculations for fatigue lifetime damage of the tower for three values of TI

Thereafter, varying the Wöhler exponent poses a considerable difference in fatigue damage due to stresses caused by both examined bending moments. For instance, choosing m=3 over m=5 changes the fatigue damage with multiple orders of magnitude. Fifthly, for none of the predefined parameters the total fatigue lifetime damage $D_{\rm life}$ approaches the value of 1, which would indicate failure. This is not uncommon, since fatigue damage is not the primary design driver for wind turbine towers. Additionally, extreme events or gusts are not included in the aeroelastic simulations in FAST to solely focus on the influence of turbulence.

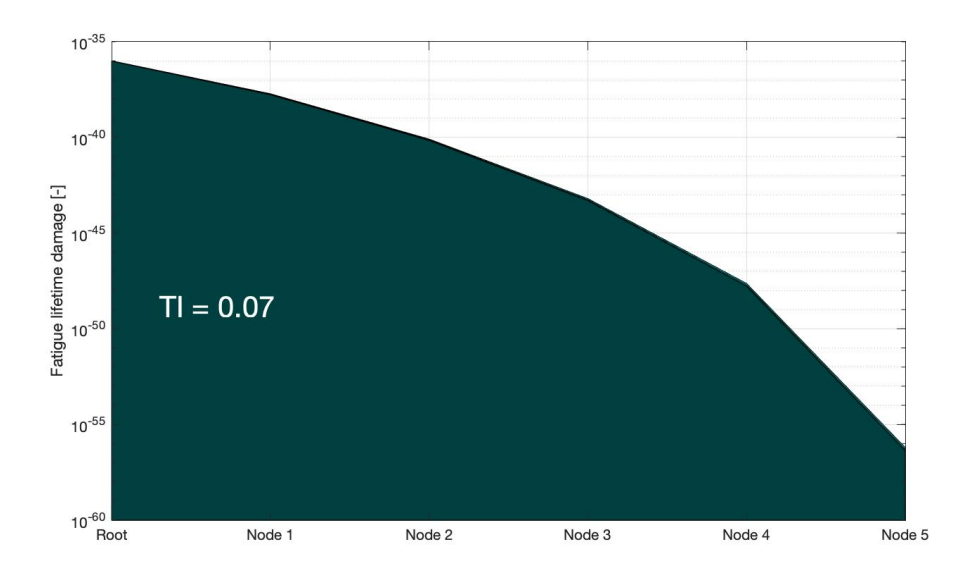
Lastly, it can be observed that for every m and both side-to-side and fore-aft bending moments the fatigue damage increases with TI. This pattern is consequently present throughout the obtained results, but the increases in fatigue damage are relatively small per higher level of turbulence. An important difference is observed between the stresses from both origins, depicted in Figure 6.12 and Figure 6.13. Where latter shows to be not very sensitive to variation in turbulence, the first seems to vary an order of magnitude for the different levels of TI. For the stresses caused by fore-aft bending moments, the fatigue lifetime damage increases on average with 10% going from TI = 0.07 to 0.09 and 0.11. For the stresses caused by side-to-side bending moments, these upsurges are over 100% for the same steps in TI.

Fatigue lifetime blades - Table 6.6 summarizes the results obtained from MLife for three TI dictated wind fields regarding lifetime fatigue damage of the blade calculated according to Equations 6.5, 6.6 and 6.7. Also, fatigue damage due to stresses from edgewise (in-plane) bending moments are presented, as well as fatigue damage due to stresses from flapwise (out-of-plane) bending moments. As stated before, a set of three Wöhler exponents m is used for each TI dictated wind field. Figure 6.14 visualizes the obtained results for m=8 for stresses caused by out-of-plane bending moments and in-plane bending moments, respectively. The reason that only one value of m is visualized is that this is the most critical Wöhler exponent for the blades. It should be noted that the difference in TI level is not very good visible in Figure 6.14, although it is tried to improve this by applying a semi-logarithmic scale. One must not be misled by this representation when interpreting the results from this graph.

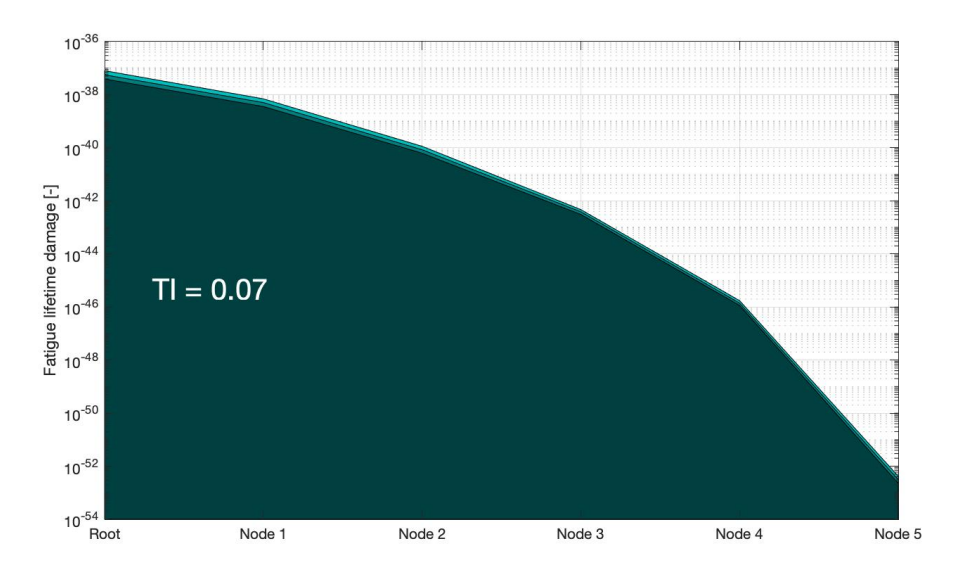
Stresses from	m	Blade root	Node 1	Node 3	Node 5
Edgewise bending moments for $TI = 0.07$	8 9 10 8 9	9.61×10^{-37} 3.68×10^{-42} 1.41×10^{-47} 3.92×10^{-38} 2.07×10^{-43}	1.68×10^{-38} 3.90×10^{-44} 9.07×10^{-50} 3.58×10^{-39} 1.40×10^{-44}	4.93×10^{-44} 2.37×10^{-50} 1.15×10^{-56} 3.09×10^{-43} 3.75×10^{-49}	4.08×10^{-57} 4.61×10^{-65} 5.28×10^{-73} 2.27×10^{-53} 1.49×10^{-60}
bending moments for <i>TI</i> = 0.07	10	1.09×10^{-48}	5.48×10^{-50}	4.57×10^{-55}	9.81×10^{-68}
Edgewise bending moments for <i>TI</i> = 0.09	8 9 10	9.87×10^{-37} 3.80×10^{-42} 1.46×10^{-47}	1.77×10^{-38} 4.15×10^{-44} 9.75×10^{-50}	5.52×10^{-44} 2.73×10^{-50} 1.37×10^{-56}	4.95×10^{-57} 5.85×10^{-65} 7.04×10^{-73}
Flapwise bending moments for <i>TI</i> = 0.09	8 9 10	5.62×10^{-38} 3.10×10^{-43} 1.71×10^{-48}	5.06×10^{-39} 2.07×10^{-44} 8.44×10^{-50}	3.87×10^{-43} 4.83×10^{-49} 6.05×10^{-55}	3.10×10^{-53} 2.11×10^{-60} 1.44×10^{-67}
Edgewise bending moments for <i>TI</i> = 0.11	8 9 10	1.03×10^{-36} 3.92×10^{-42} 1.50×10^{-47}	1.91×10^{-38} 4.44×10^{-44} 1.88×10^{-49}	6.36×10^{-44} 3.13×10^{-50} 1.77×10^{-56}	6.21×10^{-57} 7.65×10^{-65} 9.74×10^{-73}
Flapwise bending moments for <i>TI</i> = 0.11	8 9 10	8.04×10^{-38} 4.59×10^{-43} 2.46×10^{-48}	6.98×10^{-39} 2.99×10^{-44} 1.34×10^{-49}	4.69×10^{-43} 6.43×10^{-49} 8.67×10^{-55}	4.18×10^{-53} 2.93×10^{-60} 2.50×10^{-67}

Table 6.6: Results obtained for blade lifetime fatigue damage calculations in MLife for three TI values, three Wöhler exponents m and due to stresses from edgewise bending moments and flapwise bending moments

Again, it can be observed from Table 6.6 that picking a certain value for m influences the obtained fatigue lifetime damage to a big extent. Next to that, it can be noticed from Figure 6.14 that the fatigue damage of the blades is very small over its lifetime for every m, TI value and origin of stresses. The cause of this is twofold: extreme events or gusts are not included in the aeroelastic simulations in FAST to solely focus on the influence of turbulence and lifetime fatigue damage is not the main design driver for blades of modern multi-megawatt turbines. The blade (tip) deflection is the most important design driver, to avoid collision of the blade with the tower at all costs. Furthermore, it is noticeable from Figure 6.14 that the damage due to stresses from in-plane bending moments is quite similar to that due to stresses from out-of-plane bending moments.



(a) Fatigue lifetime damage due to stresses caused by in-plane or edgewise bending moments for m = 8



(b) Fatigue lifetime damage due to stresses caused by out-of-plane or flapwise bending moments for m = 8

Figure 6.14: Results of MLife calculations for fatigue lifetime damage of the blades for three values of TI

Fourthly, fatigue damage decreases significantly over the length of the blade towards the tip in all situations. It actually makes a difference of multiple orders of magnitude. Subsequently, the fatigue lifetime damage due to stresses from edgewise bending moments is higher than that from flapwise bending moments, since the gravitational forces of the blade itself are a considerable factor in the first and these forces are exerted in-plane. Lastly, the differences between the results of the several used TI values are even smaller than they were for the turbine tower. As can be seen in 6.14a, especially for in-plane bending moments the difference seems to be insignificant. This behavior could have been expected, since the turbulence is by far mostly present in the horizontal component of the wind speed u. This component exerts forces on the blades in the out-of-plane direction. Contributing to that, for the stresses on the blades from edgewise bending moments, the in-plane gravitational loading of the blades itself is very dominant. Where the difference in fatigue lifetime damage is only a few percents for stresses caused by edgewise moments, the differences amounts around 40% for the fatigue lifetime damage from stresses caused by flapwise moments.

6.3. Discussion and conclusion

General remarks - A sequence of three NREL developed software packages was used to execute the analysis of this chapter: TurbSim, FAST and MLife. It required quite some time to get fully acquainted with all three programs and especially with all the involved input and output files with different settings, lay-outs and extensions. But once it all became clear, the whole proved to be a possible valuable tool to analyze fatigue lifetime damage for all relevant parts of a wind turbine. Although sometimes complex, moderately user-friendly and mostly lacking possibilities to visualize input or output, the three software packages offer a broad palette of simulation and calculation options. Last section consequently addressed $D_{\rm life}$ from Equation 6.5 and not $T_{\rm fail}$ from Equation 6.9. The overall small values of the fatigue lifetime damage logically result in very high values for the time until failure.

Observed patterns - Several patterns have been observed throughout the results that were presented in Section 6.2. To start, the results for all wind turbine parts are hugely influenced by the choice of Wöhler exponent m. Determining the exact Wöhler exponent m for the different materials in a wind turbine can lead to a considerable higher certainty in the calculation of fatigue lifetime damages. This is considered a very tough thing to do, hence the convention of using multiple Wöhler exponents in aeroelastic simulations [45]. Next to that, fatigue lifetime damage consequently decreases along the blades towards the tip, as well as it decreases along the wind turbine tower towards the top in all situations. It is known that the blade root and tower base are the parts of a wind turbine's blade and tower, respectively, that undergo the heaviest loading and stresses and therefore it is logical that these parts suffer most from fatigue damage. Other research confirms this behavior [108] [118].

Thereafter, it is confirmed that for the 5 MW NREL baseline turbine, lifetime fatigue damage will not be the major design driver. The values are relatively low, although this is partly caused by the absence of higher wind speeds, that are not included in the aeroelastic simulations in FAST to solely focus on the influence of turbulence level. This especially influences the (now relatively low) values for fatigue damage of the turbine blades. Often, wind speeds Ufrom cut-in to cut-out speed are used to analyse fatigue. In this case there has been chosen to represent only the mean wind speed \overline{U} found in Chapter 5 and the observed variations around this value in the analysis. Fourthly, it is observed that the fatigue damage of the tower due to stresses from fore-aft bending moments is clearly higher than that due to stresses from side-to-side bending moments. As stated in Subsection 6.2.2, this behavior can be explained by the natural alignment to the wind of a horizontal axis wind turbine. Finally, this difference, between damage caused by stresses from flapwise and edgewise bending moments in this case, is far less present at the blades of the turbine. Here, the fatigue damage due to stresses from edgewise bending moments is actually a bit higher than that due to stresses from flapwise bending moments. The in-plane gravitational loading of the blades itself play an important role in this [125].

Influence TI on fatigue lifetime damage - A few conclusions can be drawn regarding the effect on the fatigue lifetime damage of the different TI dictated wind fields that were created with TurbSim. Five different wind fields were created, of which the final results of three were presented in the previous section. These wind fields have the same mean horizontal wind speed of 8.2 m/s at 100 m height over the simulation period, but have a different spread of wind speeds. For the wind turbine tower, it can be said that varying TI made a significant difference in damage caused by stresses from side-to-side bending moments. Stepping from TI = 0.07 to 0.09, as well as from TI = 0.09 to 0.11, approximately doubled the fatigue lifetime damage. For damage caused by stresses from fore-aft bending moments, the damage does not double but increases with about 10% on average. All together, it can be said that the differences between the results of the TI dictated wind fields on the tower fatigue damages are significant, but not earth-shattering. The tower fatigue damage is not very high overall, which is in line with the fact that it usually is not a critical design driver in designing a wind turbine of this proportions. Purely looking at the influence of turbulence parameter TI, the fatigue lifetime damage due to stresses from side-to-side bending moments requires special attention.

For the blades of the wind turbine, all the resulting values for the lifetime fatigue damage are way smaller than for the tower. This immediately confirms that fatigue lifetime damage of the blades is not an important design driver in the overall process of designing a multi-megawatt wind turbine. Blade design often turns out be driven by stiffness; the clearance requirement between tower and blade is more important that fatigue damage [82]. For damage due to stresses from edgewise/in-plane bending moments as well as from flapwise/out-of-plane moments, a higher TI slightly increases the damage. This is about 10% for edgewise moments and around 50% for flapwise moments. Although this difference is considerable, the total amount of damage is not.

It is not straightforward to link the results in this Chapter to existing literature, since research that zooms in on the fatigue lifetime damage cause by stresses from different bending moments in different parts of a wind turbine using simulation, especially using the software packages TurbSim, FAST and MLife, is rare. Nevertheless, the results show similarities with results from [60]. In this study, the same sequence of simulation software is used. It confirms that fatigue lifetime damage from side-to-side bending moments for the tower and flapwise (out-of-plane) bending moments for the blades are more sensitive to varying TI than their respective counterparts. Here too, this effect is stronger for the tower than for the blades. In [119], the influence of turbulence level on the fatigue lifetime damage caused by stresses from in-plane and out-of-plane bending moments of only the blade root and tower base is investigated. Here is confirmed that both are quite insensitive to variations in turbulence and that these parameters show very small values, as in this study.

Room for further research - Firstly, the research in this chapter can be seen as an introduction to the possibilities of using the sequence of the three NREL developed software packages. Further investigation on fine tuning the settings of the created wind fields, the controls in the aeroelastic simulation and the parameters in the fatigue lifetime damage calculations can all possibly contribute to approaching reality even more and draw more conclusions from simulation. This can e.g. involve the comparison of different turbulence models and the use of many more wind fields for every wind speed bin between cut-in and cut-out wind speed (instead of only 1 wind field per *TI* value) in TurbSim. The development of a tool to easily draw up all the required turbine input parameters for FAST could be valuable, since it would then be possible to simulate with the exact preferred virtual turbine, tailored to the needs of a specific wind turbine design and/or location. In this research an available reference 5 MW turbine from NREL was used and not a turbine of 4 MW as will be placed in wind farm "Windplan Blauw".

Next to that, it has been found that knowing the exact material properties of the steel and fiberglass components of the turbine is essential for interpreting results from software such as MLife, as results for fatigue lifetime damage can differ significantly for varying Wöhler coefficients or ultimate design loads. This proposition is shared by [119], which extensively addresses uncertainty factors around the determination of fatigue damage for wind turbine materials. He makes a valuable contribution with a plea for synthetic S-N curves.

In this study only relatively low levels of average turbulence are examined; levels of turbulence closely related to measurement inaccuracies from e.g. LiDAR versus met masts. TI levels in the range of 0.15 - 0.25 or even higher are less common for Dutch onshore sites, but assessing these levels of turbulence might reveal a stronger relationship between turbulence and fatigue lifetime damage of turbines. Next to that, a representative pattern of extreme winds or gusts could be added to the aeroelastic simulation to approach a more realistic situation. Why this is not done in this research was stated earlier. Subsequently, this research uses a model for calculating stresses on both tower and blades as introduced in Section 3.3. This model is a representation close to reality for the turbine tower, but can be seen as a simplification for the turbine blades. It would require more complex blade models to assess the fatigue damage in a more realistic way. There are numerous models there to represent the stresses on the structure of a wind turbine blade in a closer to realistic way than is done here, like in [108] or [31] with the help of different damage models or finite element modeling.

Intra-annual variability of turbulence

As posed in Section 2.1, turbulence at a site originates mainly from two processes: wind shear due to obstacles and radiation from the Earth's surface heated by the Sun. Since both locations under investigation in this research almost completely lack obstacles around them, the attention goes to the latter. As the radiation of the Sun in this part of the Netherlands (as in every part) heavily varies per season and month, turbulence and its most important indicator in wind engineering turbulence intensity TI are expected to do so too. This chapter addresses this intra-annual variability of turbulence in a quantitative way, since this variation can possibly be an important factor in achieving reliable, shorter measurement campaigns. When meaningful intra-annual variability is observed, this can mean two things. Firstly, it can point out which periods of the year in the Netherlands are most useful or reliable for very short measurement campaigns of 3 to 6 months. Secondly, it can confirm the need for a data adjustment method when short measurement periods are the only data available or when the time to conduct a measurement campaign with LiDAR is only very short. As introduced in Subsection 2.3.4, Measure Correlate Predict is the widely known method to fulfill this need. The methods to observe the possible intra-annual variability of turbulence in a quantitative way are presented in Section 7.1. The results are presented in Section 7.2 and discussed in Section 7.3. Note that the data used in this chapter comprises of the full year 2019; a different time frame than in Chapter 5.

7.1. Method

The intra-annual variability of the turbulence intensity TI is examined at both locations in wind farm "Windplan Blauw" for a measurement height of 100 m. There is no distinction made between wind direction sectors, since hardly any obstacles are present around both locations, as elaborated on in 4.2. Firstly, monthly average turbulence intensities $\mu_{TI, month}$ are calculated for different heights, showing the variation of turbulence throughout the year 2019 and possibly indicating patterns over the year and between different heights. Secondly, the turbulence intensity probability distribution $P(TI_i)$ is determined for every month of the year. Differences between months can be exposed and a comparison of each month with the entire year is executed. Since no probability density function is known for the distribution of TI, the yearly and monthly data are binned with the help of histograms, which were already introduced in 5. A probability is assigned to each bin according to Equation 7.1, where n_i is the number of elements that fall into bin i and N_{month} is the total number of elements in a certain month. Analogously, N_{vear} is used for the yearly probability distribution.

$$P(TI_{\rm i}) = \frac{n_{\rm i}}{N_{\rm month}} \tag{7.1}$$

Intra-annual variability of turbulence in Wind farm "Windplan Blauw" - In this section, the results on the intra-annual variability of turbulence intensity TI are presented for location 1 and 2 in wind farm "Windplan Blauw". The results for both locations are expected to be quite similar. Nevertheless, the results from both locations are discussed for the purpose of completeness and mutual comparison. Although the wind roses of both locations are not uniform, as posed and visualized in Section 4.2, TI is not binned per wind sector for the sake of simplicity. Location 1 is discussed first, subsequently location 2 will be treated. Although somewhat more than one year of data was available for both locations, this is reduced to exactly one year: the year of 2019. In this way, the monthly average turbulence intensity μ_{TI} and monthly TI probability distribution $P(TI_i)$ can be compared with the yearly values and distributions.

For both locations, the data that is used in this chapter originates from the ZX300 LiDAR devices installed at these locations, as elaborated on in Section 4.2. This implies the presence of 52,560 data points of 10 minute averaged turbulence intensity measurements for both LiDARs. However, this is not entirely true since the data availability at 100 m height is slightly above 99% for both LiDARs, which was reported in Section 5.2.1. Next to that, the amount of data points can slightly differ between months for the simple reason that not every month has the same number of days. Two causes usually dominate turbulence in the air: obstacles around the measurement station and heat radiation in the air. The first are basically absent around the locations in "Windplan Blauw". The latter is always present and is logically influenced by the seasons. Therefore, this cause of turbulence is expected to be the main driver for possible differences in TI over the year.

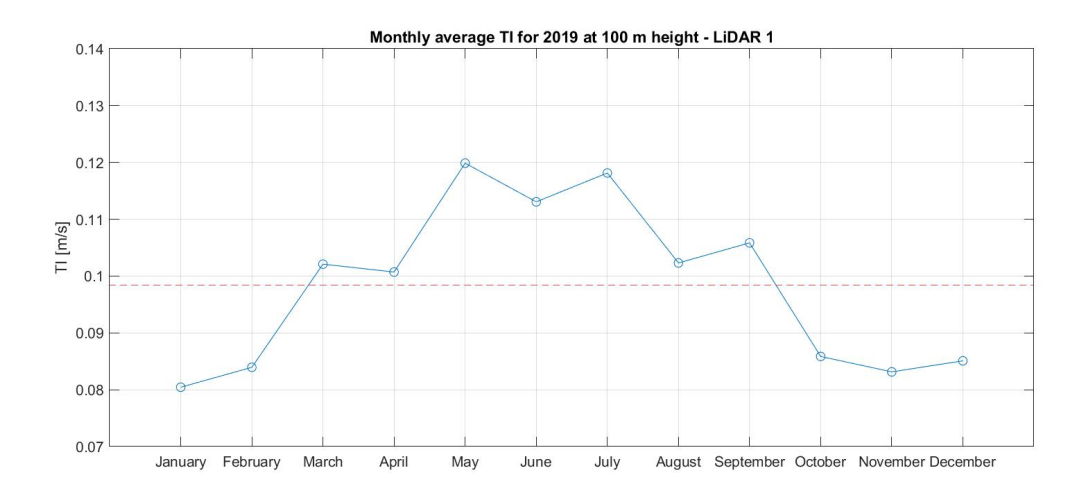


Figure 7.1: Monthly averages μ_{TI} for each month of the year 2019, measured by LiDAR 1 at 100 m height. The red dashed line indicates the yearly average value of the same year.

Wind farm location 1 - Figure 7.1 depicts the monthly averages of the turbulence intensity μ_{TI} measured by LiDAR 1. The data points for every month of 2019 together give a yearly average TI value of 0.098, which is indicated by the horizontal, red dashed line. All monthly averages fall within the range of 0.08 < μ_{TI} < 0.12. January, February, October, November and December are characterised by a relatively low μ_{TI} between 0.08 and 0.09. The averages of March, April, August and September can be categorized as intermediate values, ranging from 0.10 to 0.11. The higher μ_{TI} close to 0.12 are found in summer, in the months May, June and July. A clear pattern over the year can be observed. The pattern actually mostly looks like a sine-wave with an amplitude of 0.02, translated 0.1 upwards. The top seems to lie a bit shifted to the left; towards May/June. The observed behavior is in line with the expectations: a higher degree of turbulence during the summer months, induced by radiation rising up from the Earth and originating from the heating of the Earth's surface by the Sun. Next

to that, the presence of water closeby can influence the level of turbulence. The difference between the temperature of the water in the proximate IJsselmeer and the surrounding air can induce heat transfer and therefore turbulence in the wind. This temperature difference varies with the seasons and can therefore influence the seasonal pattern of TI.

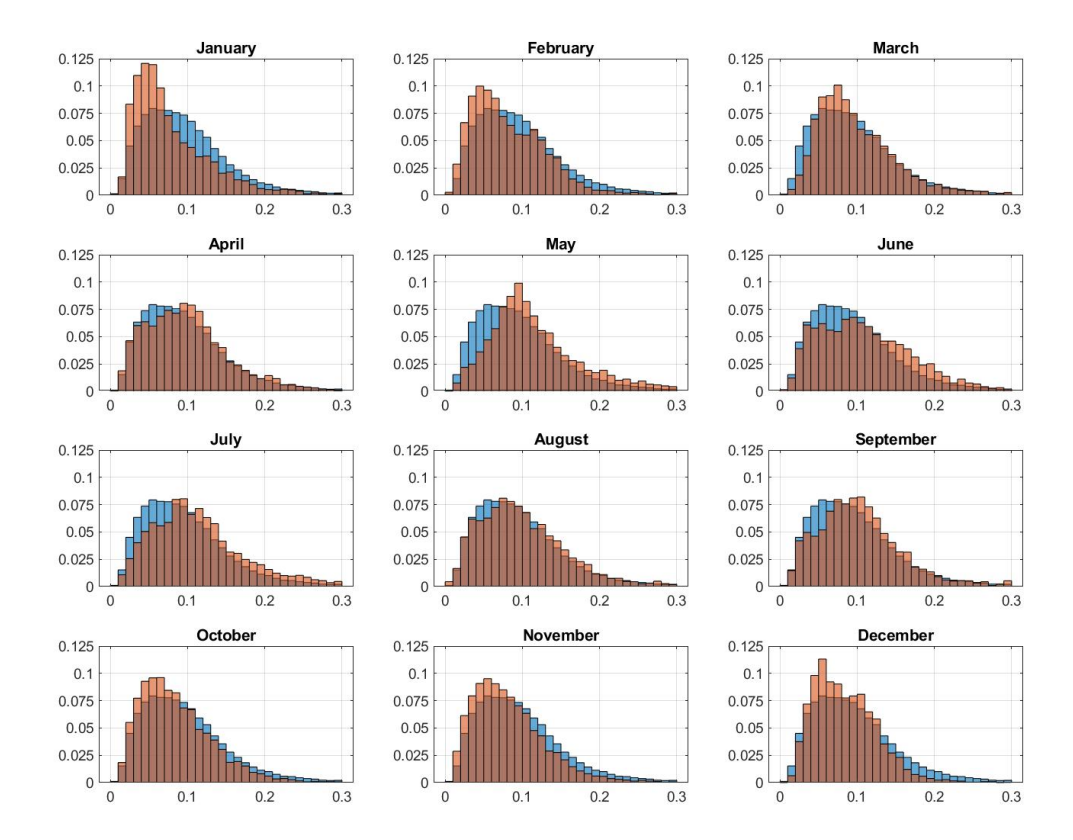


Figure 7.2: The turbulence intensity probability distribution $P(TI_i)$ for every month of 2019 as measured by LiDAR 1, visualized by the orange histograms. The blue histogram in the background is the $P(TI_i)$ for entire 2019.

To further examine the intra-annual variability of turbulence for location 1 at wind farm "Windplan Blauw", there has been looked in the turbulence intensity probability distribution $P(TI_i)$ for every month of 2019. Figure 7.2 shows the distribution of every month by means of a histogram, accompanied by a blue histogram in the background, which is the probability distribution for entire 2019. A bin width of 0.01 is used for the values of TI on the x-axis, thereafter the probability of each bin can be read on the y-axis. It can be observed that the distributions of the months December, January and February form the biggest underestimate of TI, when compared to the yearly probability distribution. The histograms of October and November also show monthly distributions that seem to be more shifted towards the left, whereas the one of March shows to be roughly balanced with the yearly distribution. The monthly histograms of April up to and including September are shifted towards the right with respect to the yearly turbulence intensity probability distribution, indicating a higher degree of turbulence over these months. The latter is expected and confirmed by Figure 7.1.

Wind farm location 2 - Figure 7.3 depicts the monthly averages of the turbulence intensity μ_{TI} measured by LiDAR 2. The data points for every month of 2019 together give a yearly average TI value of 0.094, which is indicated by the horizontal, red dashed line. The monthly averages show a slightly wider range than for LiDAR 1, they show a range of 0.07 < μ_{TI} < 0.12. It can immediately be observed that the degree of turbulence seems to be a bit less at location 2 compared to location 1, considering that the yearly average is somewhat lower

and that there are actually quite some months with an average μ_{TI} below 0.08, namely the winter months from October to February. Furthermore, the same bell-shaped curve can be observed in Figure 7.3 too, albeit the monthly averages measured by LiDAR 2 follow this distribution a bit less meticulous than those from LiDAR 1. Figure 7.4 shows the TI probability distribution of every month by means of the same orange and blue background histograms.

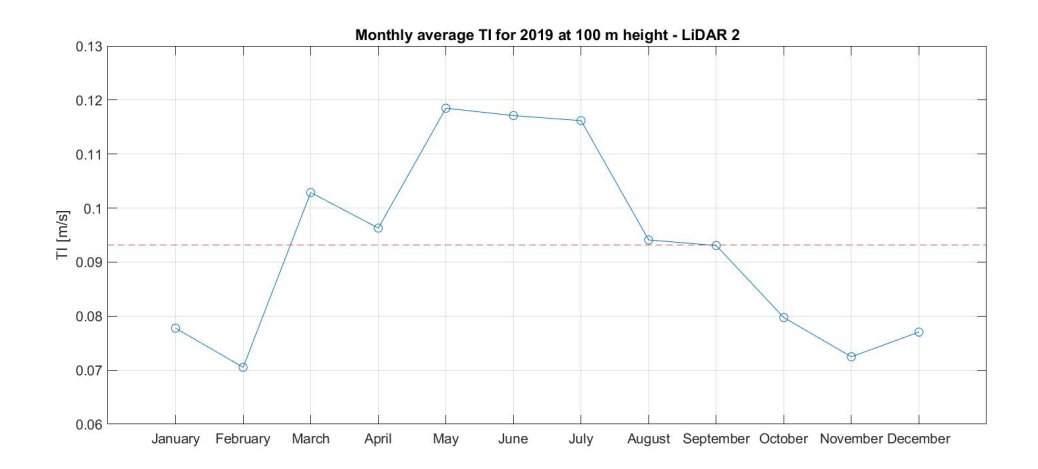


Figure 7.3: Monthly averages μ_{TI} for each month of the year 2019, measured by LiDAR 2 at 100 m height. The red dashed line indicates the yearly average value of the same year.

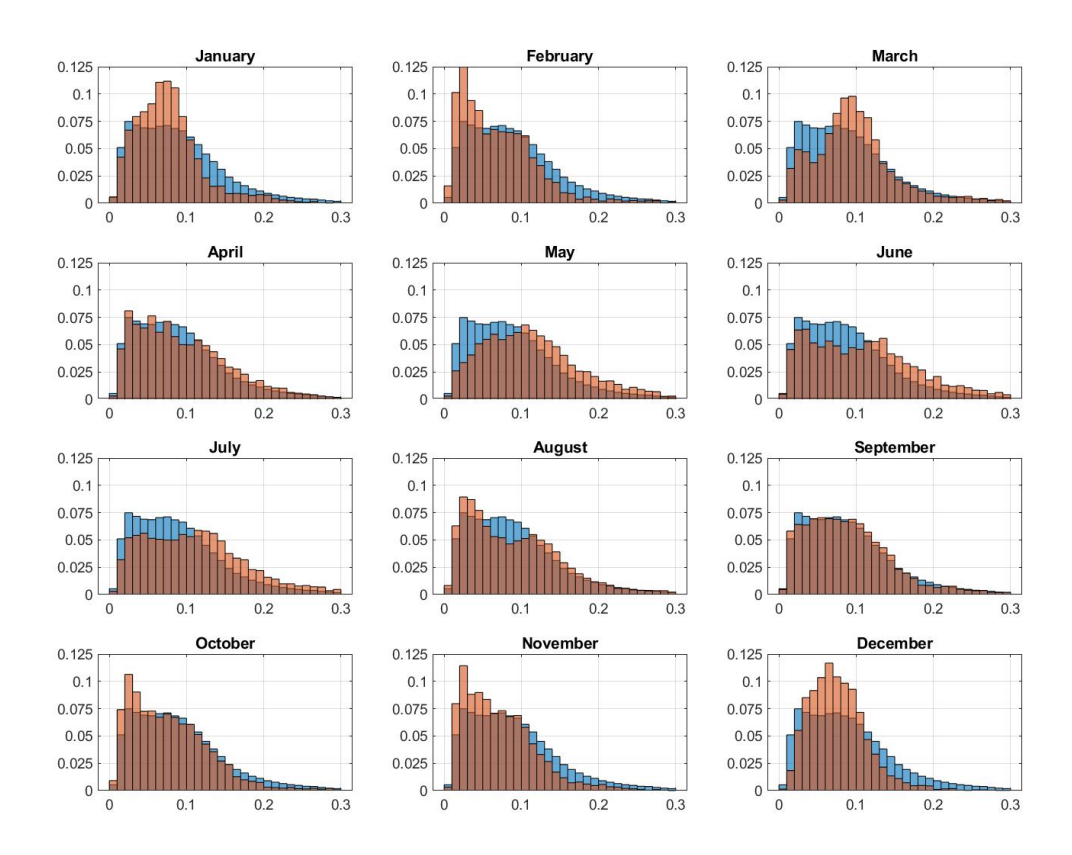
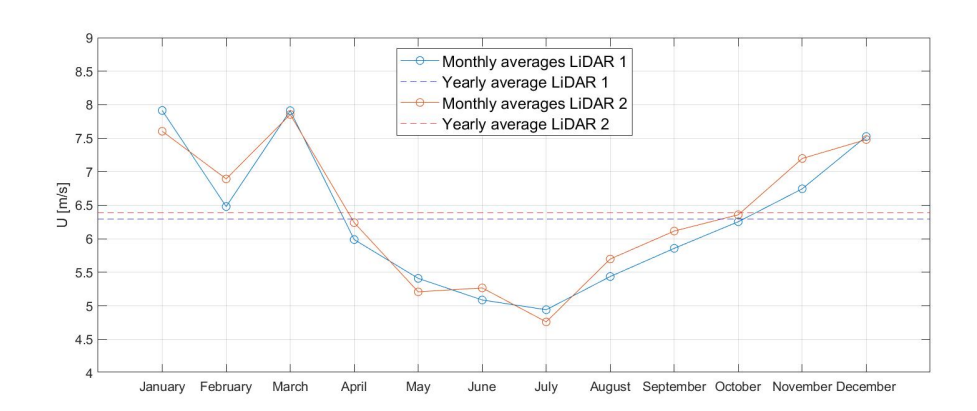


Figure 7.4: The turbulence intensity probability distribution $P(TI_i)$ for every month of 2019 as measured by LiDAR 2, visualized by the orange histograms. The blue histogram in the background is the $P(TI_i)$ for entire 2019.

This yearly distribution is more shifted to the left relative to the $P(TI_i)$ of LiDAR 1, again indicating more low TI values overall. On the contrary of LiDAR 1, the range of months that are fairly below the yearly distribution is wider. Not only November, December and January are, but also February and October are member of this subset. Next to that, the monthly distribution of August and September are quite in balance with the yearly one. The histograms of March until July show the same behavior as observed for LiDAR 1; a higher degree of turbulence rules over these summer months.

Origin of observed seasonal pattern in TI - To find out what drives the found seasonal pattern in turbulence intensity TI in the above part of this section, a closer look is taken to both factors that lie behind the equation for TI via Equation 5.2: wind speed U and standard deviation $\sigma_{\rm u}$. For both, the yearly and monthly averages are depicted in Figure 7.5 and an interesting notion is revealed. The upper half, showing measurements of U over 2019 from both LiDARs, shows a clear seasonal pattern for the horizontal wind speed. Except from apparent deviant behavior of the weather in March, which is explained below, both LiDAR measurement data sets form a trough parabola over the year. This is consistent with the fact that temperature differences between air masses induce pressure differences and produce wind. Winter in northwestern Europe will bring higher temperature gradients, which causes wind speeds to be higher than in summer [27]. During summer and winter months, the average U is around 5 and 7 m/s, respectively. This gives annual averages around 6.5 m/s. To avoid confusion, this is indeed different from Table 5.2. This is caused by the different time span under attention, which is around 7 months in Chapter 5 and is exactly 1 year in this chapter (2019).



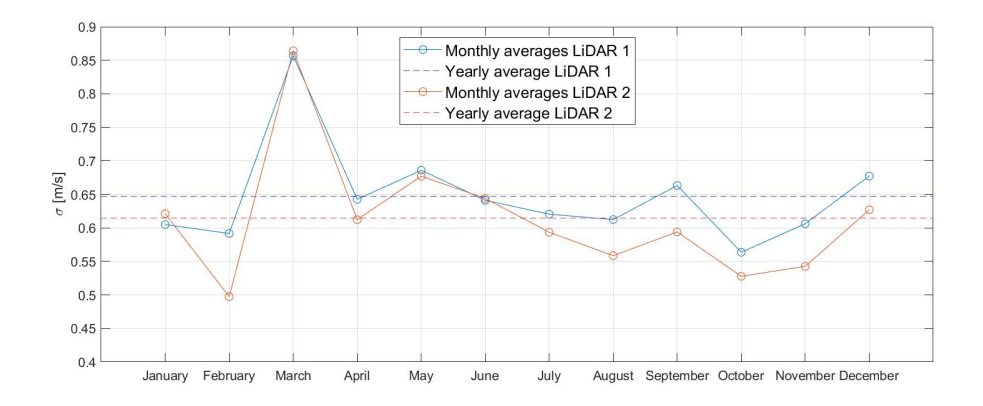


Figure 7.5: Yearly pattern of horizontal wind speed U and standard deviation $\sigma_{\rm U}$ at 100 m height for both LiDARs

On the contrary, the measurements of σ_u from both LiDARs at the bottom of Figure 7.5 hardly show any distinguishable pattern over 2019. This is counter intuitive, taking Figures 7.1 and 7.3 in mind. Again, it can be seen that March 2019 has been an unusual month for location "Windplan Blauw". This is believed to be caused by storms Freya and Eberhard, who both ravaged northwestern Europe during that particular month in 2019 [94]. Taking a look at the data, many very high wind speeds and rapid variations in U are observed on several days in March 2019. Hence the significantly higher monthly average wind speed U and standard deviation σ_u . This is not regularly observed in spring at this location, but for 2019 it is causing the peaks in Figure 7.5. Furthermore, almost all other monthly averages lie in the range of 0.53 < σ_u < 0.68. The yearly means lie just above 0.6. There is no pattern discoverable for the standard deviation; it seems to be more or less constant over the year.

7.3. Discussion and conclusion

The degree of turbulence and therefore turbulence intensity TI varies within a year for every site on Earth, also for both locations in wind farm "Windplan Blauw". The measurements of LiDAR 1 and LiDAR 2 show varying averages per month relative to the entire year 2019. Because of the absence of obstacles around both locations and the measurement height of 100 m, these variations in turbulence over the seasons are believed to be caused by the differences in radiation level of the Earth's surface by the Sun from month to month. Next to that, both locations lie in close proximity of the big IJsselmeer lake (English: Lake IJssel). The difference between the local water temperature and the air temperature can play a role in the presence of turbulence too. The bigger the temperature difference, the bigger the temperature gradient and therefore the heat transfer. The latter can contribute to turbulence in the wind. Since the mentioned temperature gradient is usually bigger in summer, this is a possible contributor to the observed pattern in the last Section too.

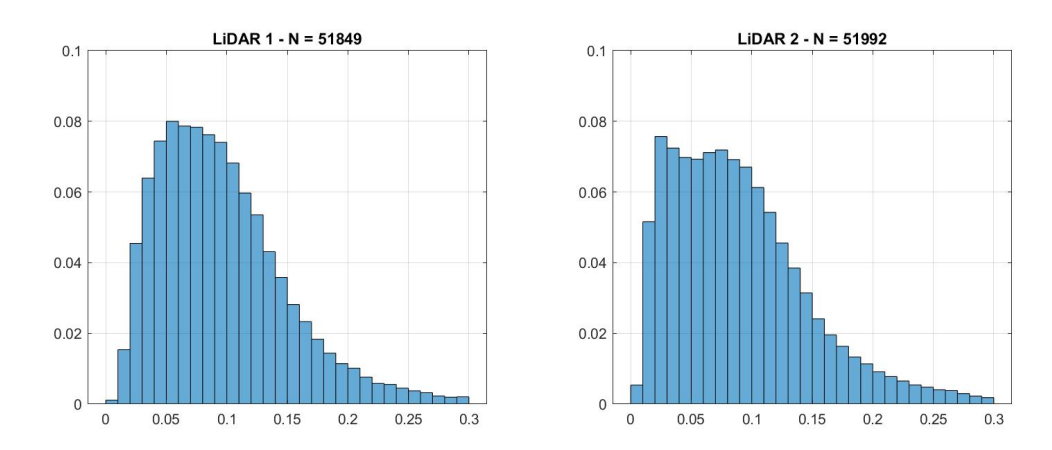


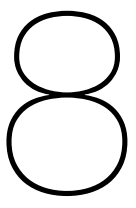
Figure 7.6: The turbulence intensity probability distribution $P(TI_i)$ from both LiDARs for 2019.

The analysis in this chapter confirms the presumption that a lot of subsets of months do not accurately represent the actual yearly distribution of turbulence intensity. Where the periods around March and April and August and September could sometimes and in some way be seen as an appropriate representation of this yearly distribution, most other periods can surely not. Wintry months ranging from October up to and including February represent a distribution that underestimates the degree of turbulence compared to the entire year. Vice versa, measurements from May, June and July show a higher level of turbulence with respect to the yearly distribution. For better visibility and mutual comparison, both yearly distributions are also depicted separately in Figure 7.6. They show a similar pattern, although the measurements from LiDAR 2 display a slightly higher share of lower TI values, i.e. between 0 and 0.05. This is in line with the findings from Chapter 5, where a lower μ_{TI} was found for LiDAR 2 in contrast to LiDAR 1. In conclusion regarding short LiDAR measurement campaigns of around 3 to 4 consecutive months at locations of similar fashion, time frames with

their center around September or March could be able to flatten out seasonal patterns in TI, as observed at two locations in "Windplan Blauw". Next to that, when a slightly longer measurement campaign of around 6 months would be considered, the TI distribution in the time frames June - November and December - May seem to be in reasonable accordance with the yearly distribution according to the findings in this chapter. Measurement data from these time frames should nevertheless handled with care, as generalizing them to yearly data will always be less precise than obtaining yearly data for a certain location. Another and a considered better option, is the use of artificially created yearly data.

The observed variations within a year validate the necessity, or at least the exploration, of extrapolation techniques to account for the intra-annual turbulence variations. The best known way to perform such data extrapolations is the in Subsection 2.3.4 introduced Measure Correlate Predict (MCP) methodology. The next chapter will comprise of research into the use of MCP in short measurement campaigns, which are inherently associated with the flexible but expensive use of LiDAR devices. It will be examined in what way the length of the measurement data of the target site, the season that is picked out of the measurement data of the target site and the chosen MCP method can influence the accuracy of the predicted data.

The last part of the previous section revealed that the found seasonal TI pattern gives misleading thoughts on the variability of the wind speed. The latter is expected to be represented by the part of $\sigma_{\rm u}$ in the formula for TI, but it is actually the average wind speed U that is the cause of the earlier observed seasonal pattern of turbulence intensity. This means that the variability of the wind speed U over the year for this location is only there in absolute terms and that relatively seen the variation is approximately equal over the seasons. In addition to Appendix C on the proposition of using transience $\tau_{\rm m}$, introduced in Chapter 5, over $\sigma_{\rm u}$, this gives rise to an increased questioning of the use of TI in site assessment to represent turbulent variability in the wind. It seems somewhat misleading to let the average wind speed \overline{U} in 10 minute intervals have such big influence on the TI value, keeping in mind that this parameter should be a representative indicator of turbulence. The mean influences $\sigma_{\rm u}$ and therefore TI via Equation 2.11 and TI directly via Equation 2.6.



Application of MCP methodology on short LiDAR measurement campaigns

In this chapter, the earlier introduced Measure Correlate Predict (MCP) methodology is applied in a case study involving both locations in wind farm "Windplan Blauw". In this case study the focus lies on LiDAR measured TI, trying to answer various research questions regarding the application of MCP on turbulence measurement data. These questions range from defining the consequence of the length of the data set from the target site for the level of representation of turbulence in the predicted data to the determination of how well TI data from a certain season can predict the yearly turbulence distribution. Next to that, the results of several MCP algorithms or methods are compared. Section 8.1 elaborates on the framework of this part of the research, consisting of the MCP proceedings, the experimental setup and the performance metrics. The results are presented and explained extensively in Section 8.2, after which these are discussed in the last Section 8.3. Note that the data used in this chapter comprises of the full year 2019, just as in the preceding chapter. This time frame differs from the one used in Chapter 5.

8.1. Method

Measure Correlate Predict is the best known and most used methodology for the extrapolation of short-term wind measurement data to usable long-term data in wind energy science and site assessment [25]. As touched upon in Section 3.4, MCP is usually used for the extrapolation of horizontal wind speed U measurement data. This comprises of 10 minute averaged data for a relatively short period, which are then extrapolated to a data set of 10 minute averaged wind speeds representing one to several years. Since turbulence intensity TI is indirectly derived from 1 Hz measurements in every 10 minute interval (see Equation 2.6), one would need 1 Hz data for 3 to 6 months to properly extrapolate these to a reliable set of TI values over a range of at least 1 year. Because of the fact that wind farms often lie at more remote locations without proper internet connection, LiDARs ordinarily save these 1 Hz values on their internal data logger. It is not desirable to let these inner devices use big parts of their internal memory for saving enormous amounts of 1 Hz signals at the expense of their computing power. Therefore, these data loggers often save 1 Hz measurements for only 1 or 2 months. This is even too short for the application of MCP on 1 Hz U measurement data and exposes the insistence of applying MCP directly on 10 minute averaged TI measurement data. Next to this, 1 Hz U or σ_{11} data can be absent for other reasons.

How this is done exactly will be illustrated in this section, starting with an precise explanation of the followed MCP procedure in Subsection 8.1.1. Subsection 8.1.2 treats the experimental setup of this chapter and the motives behind it. Lastly, the performance metrics on which the results of the MCP will be judged are introduced in Subsection 8.1.3.

8.1.1. Proceeding of applying Measure Correlate Predict methodology

The Measure Correlate Predict methodology is visualized by means of the flowchart in Figure 8.1. The respectively grey, red and blue area(s) represent the three generic steps in the methodology. Next to that, two other processes can be distinguished in the flowchart. Firstly, data selection is executed to arrive at reliable and usable data to establish a correlation via one of the in Subsection 2.3.4 introduced MCP methods. Next to that, the predicted long-term data for the target site is compared to the actual data afterwards on the basis of several performance metrics, which are elaborated on in Subsection 8.1.3. The other four components of the methodology are shortly discussed below.

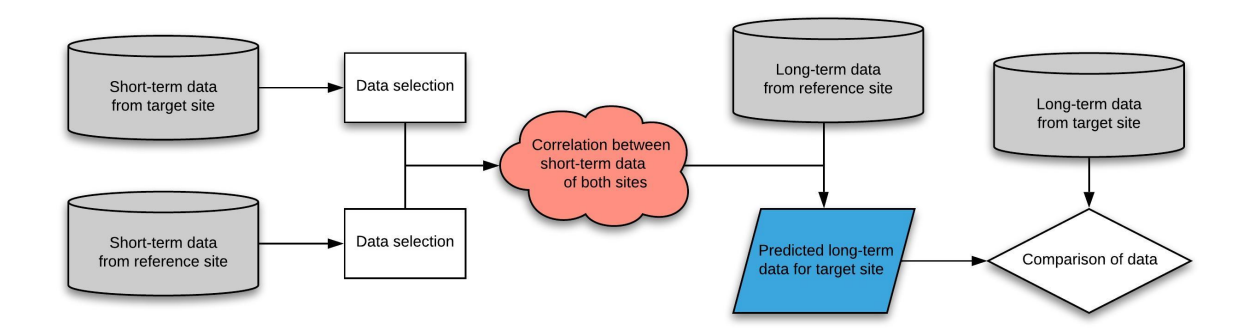


Figure 8.1: Flowchart of the Measure Correlate Predict methodology. The grey areas refer to the measured data, the red area includes the second step wherein a correlation is established and the blue area depicts the last step: the prediction.

Data measurement and selection - The measurement data that is used in this chapter originates from LiDAR 1 and met mast 2, which were introduced in Section 4.2. The location of LiDAR 1 functions as the target site and the location of met mast 2 functions as the reference site. From both instruments, 10 minute averaged data is available for a period of more than 1 year. However, to avoid the proven seasonality effects in *TI* from Chapter 7, the length of the long-term data has been set at one year. The length of the short-term data that is picked from this set varies in this study; the next subsection addresses the experimental setup in more detail. In the data selection, 9998 and 9999 values are removed from the time series from the LiDAR, as well as the their corresponding values in the met mast data.

Both data sets are subdivided into direction sectors of 45°, resulting in 8 direction sectors. The first sector ranges from 0° to 45°, the second sector from 45° to 90° and so forth. Correlations will be established per direction sector, as it is suspected that the correlations between both sites are wind direction dependant. This implies a possible improvement of the prediction by increasing the number of wind direction bins. However, the amount of direction sectors considered is a trade-off between the preciseness of a high amount of bins and the data sampling, which means having enough data to fill each direction bin [115]. This is especially a concern when short time frames are considered, as is the case here.

Establishing correlations - Several MCP methods were touched upon and explained in Section 3.4, of which three have been highlighted: the linear regression method (LR), the variance ratio method (VR) and the Mortimer method (MM). The latter is not used in this chapter, since the amount of data available is not sufficient to fill the matrix of the average of the calculated ratios. The variance ratio method is based on Equation 2.14 and uses the following parameters of target site y and reference site x: mean μ_y , standard deviation σ_y , mean μ_x and standard deviation σ_x . These parameters are calculated with the corresponding MATLAB functions mean and std. The linear regression method uses the most common type of LR: the in Subsection 2.3.2 introduced least-squares fit, which is incorporated in the MATLAB function fitlm. Both sites represent arrays of n observed values x and y given by $(x_1, y_1), (x_2, y_2), ..., (x_n, y_n)$. Using the linear regression relation, the values in these arrays form a system of linear equations, which can be represented in matrix form as in Equation 8.1.

8.1. Method 87

$$\begin{bmatrix} y_1 \\ y_2 \\ \vdots \\ y_n \end{bmatrix} = [\alpha] \begin{bmatrix} x_1 \\ x_2 \\ \vdots \\ x_n \end{bmatrix} + [\beta]$$
(8.1)

Prediction long-term data - The established relationship between the short-term data of the target site and the reference site is used to convert the long-term data of the reference site into a prediction for the long-term for the target site. Every data point for a period of one year is predicted by means of filling in the Equations 2.12 and 2.14, accomplishing the main goal of applying MCP. This is done eight times for each time frame, in accordance with the earlier mentioned eight direction sectors. Afterwards, the wind direction differentiated data is merged again to one prediction to obtain comparable 1-year distributions. The procedure is based upon the assumption that there exists a linear relationship between the target and reference site for every direction sector. The quality of the found relationship can be tested by means of the coefficient of determination R^2 , discussed in Section 2.3.

8.1.2. Experimental setup

This chapter includes several research subgoals. It assesses multiple MCP algorithms, it examines in what way the length of the measurement data of the target site can influence the accuracy of the predicted data and tries to find out what the effect is of picking different seasons as short-term target site data. This results in an experimental setup as depicted in Table 8.1. Considering the length of the short-term measurement time frame, there has been chosen for 3 and 6 months. These time frames are time-wise practical and identified as possible lengths for short LiDAR measurement campaigns by others [117] [58]. Considering the selection of months, it has been chosen to go for a set of months without mutual overlap and which are a logical choice when looking at our Roman calendar.

Number	Length	Months
1	3 months	January - March
2	3 months	April - June
3	3 months	July - September
4	3 months	October - December
5	6 months	January - June
6	6 months	July - December

Table 8.1: Experimental setup of MCP study

8.1.3. Performance metrics

As can be seen in the flowchart of Figure 8.1, the last process step in the Measure Correlate Predict procedure is the comparison of data. This is where the outcome of MCP, the prediction of the long-term data of the target site, is compared with the actual long-term data of the target site. This step is key in determining the performance of the prediction and attempts to measure the accuracy of the prediction compared to the actual measurement data. Other research reveals the use of a diversity of performance metrics to evaluate the accuracy of the data predicted by means of MCP.

To start, metrics are used that are specifically focused on applying MCP on wind speed U, like the Weibull distribution shape parameter k and scale parameter a, the annual energy production (AEP) and the capacity factor c [17]. Naturally, these metrics cannot be used here. Other, more general statistical metrics can be used. The root-mean-square error and coefficient of determination are also used in measuring the performance of MCP, but it is chosen not to use these although R^2 is evaluated for each case [115]. Two metrics are used in almost every study on MCP: mean μ and standard deviation σ [25] [99]. Because of their simplicity and excessive use, both are adopted in this study too. Another often used metric that is adopted is the chi-squared statistic χ^2 , less known under the actual and correct name Pearson's chi-squared test. This test is used to check whether possible statistically

significant differences exist between the expected and observed frequencies of a certain variable. In line with [99], normalized versions of these three performance metrics are used. This normalization facilitates the comparison of different data sets, which is desirable. The three normalized performance metrics are listed below.

Performance metric 1: Normalized mean

$$\mu_{\text{norm}} = \frac{(\mu_{\text{TI}})_{predicted}}{(\mu_{\text{TI}})_{measured}}$$
(8.2)

Performance metric 2: Normalized standard deviation

$$\sigma_{\text{norm}} = \frac{(\sigma_{\text{TI}})_{predicted}}{(\sigma_{\text{TI}})_{measured}}$$
(8.3)

Performance metric 3: Normalized chi-squared statistic

$$\chi_{\text{norm}}^2 = \sum_{i=1}^M \frac{(O_i/N_O - E_i/N_E)^2}{E_i/N_E}$$
 (8.4)

The composition of the first two metrics can be found in Equations 8.2 and 8.3. Both normalized mean μ_{norm} and normalized standard deviation σ_{norm} are composed as a ratio of the value representing the predicted data set over the value representing the corresponding measured data set. The normalized mean and standard deviation indicate how accurate the mean and standard deviation are predicted by the MCP algorithm concerned. Both parameters are extensively discussed in others section of this thesis, so no further explanation is given here.

$$\chi^2 = \sum_{i=1}^{M} \frac{(O_i - E_i)^2}{E_i} \tag{8.5}$$

The normalized chi-squared statistic χ^2_{norm} as shown in Equation 8.4 is derived from the regular formula for the chi-squared statistic χ^2 in Equation 8.5. To be more precise, this chi-squared goodness of fit test is used to compare the predicted TI distribution with the actual TI distribution. In Equation 8.4, M is the total number of bins, i is the bin number, O_i is the number of measurements or observations in bin i according to the prediction and E_i is the expected number of measurements in bin i according to the real data [99]. The difference between both formulas is again the use of ratio in the normalized version of the chi-squared statistic, causing it to be independent of the number of data points in a certain bin i in O_i and E_i . The outcome of χ^2 is a number between 0 and 1. The closer this value approaches zero, the greater the agreement between both data sets is. A significance level is often chosen to imply a threshold for statistical significance, e.g. 0.05 or 0.10 [93]. The bin width used in the chi-squared analysis equals 0.01, making sure that there are enough bins but also enough data point per bin. Appendix F elaborates on the matter of the normalized chi-squared statistic χ^2_{norm} with an easy to understand example.

8.2. Results

The results of the analysis in this chapter are presented in this section. For the first and second step, the intermediate results are presented too. Subsection 8.2.1 shows the data measurements that serve as input for the MCP algorithms and subsection 8.2.2 elaborates on the obtained correlations for all 8 direction sectors and for each experiment number from Table 8.1. Eventually, the results on the performance of the predictions are presented in subsection 8.2.3.

8.2. Results 89

8.2.1. First step: Measure

Figure 5.9 shows the input of the first step in the MCP procedure: data measurement and data selection. The target site is depicted above in red and the reference site is depicted below in blue. The six experiments introduced in Subsection 8.1.2 all comprise of quarters of the year 2019. The limits of these four quarters are indicated by the black dotted lines. It can be observed that the overall level of TI is higher at location 1 than at location 2 and that both locations show the in Chapter 7 discussed intra-annual variability. Note that these graphs are not yet differentiated by wind direction sector and that data selection took place by omitting values equal to '0', '9998' and '9999' out of the original data.

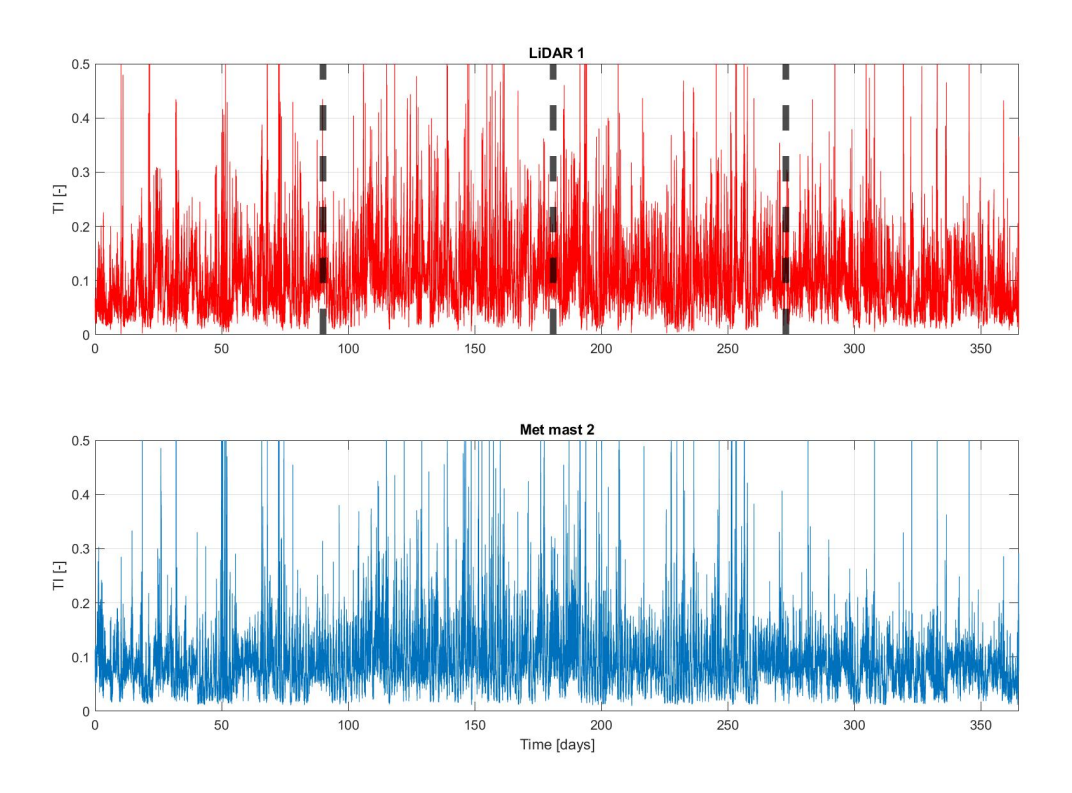


Figure 8.2: *TI* time series of one year for location 1 by LiDAR (above) and location 2 by met mast (below), with the black dotted lines indicating the four quarters of 2019 that serve as input for the MCP procedure

8.2.2. Second step: Correlate

The combination of 2 MCP methods, 8 wind direction sectors and 6 experiments results in a total of 6*2*8=96 obtained linear models. For 2 experiments, these are shown in this subsection. The others are discussed here too, but their details can be found in Tables G.1, G.2, G.3 and G.4 in Appendix G. This appendix also provides two graphs in Figures G.1 and G.2 with the point clouds of two wind direction sectors of experiment 2; one where the linear models obtained from both MCP methods are more alike each other and one where this is certainly not the case. Ideally, both algorithms would give approximately the same linear model as result, but experience learns that this is often not the case. Next to that, different linear models can lead to more closely matching results as one might expect in the first place. As stated in Section 3.4, the variance ratio method is considered an extension and an improvement of the linear regression method. It should be noted that the number of data points per direction sector does not coincide with the wind roses from Chapter 5. This is because the time frames are not the same, as has been highlighted at the very begin of this chapter.

The intermediate results for the 96 obtained linear models show a wide variety. Several patterns can be observed herein. Firstly, the linear models obtained via the linear regression

method (LR) differ significantly from those obtained via the variance ratio method (VR). The LR models are consequently characterized by a low slope parameter α and a high offset β . Values for α are mostly in the range of 0.2 - 0.7 and β ranges from 0.03 to 0.09. On the contrary, the VR models often have a slope parameter α close to 1, mostly in the range 0.8 - 1.3. The results for the last quarter of 2019 in Figure G.3 are an exception to this, since higher values for α are obtained here. The offsets β found via the VR method are almost always equal to or lower than 0.04 and show negative values sometimes. Summarizing the above, the obtained LR models show relatively low α and high β and the obtained VR models vice versa. It is suspected that the correlations established by the LR method are not that accurate on itself and also less accurate than those established by the VR method. The reason behind this suspicion is twofold. Firstly, the α and β values are quite unusual. Secondly, the values for R^2 that accompany the LR models are not in the desired range; towards the value of 1. They range between 0.35 and 0.6, which is relatively low.

Sector	$y = \alpha x + \beta$	$y = \mu_{y} - \frac{\sigma_{y}}{\sigma_{y}} \mu_{x} + \frac{\sigma_{y}}{\sigma_{y}} x$	Data
#	Linear regression method	Variance ratio method	points
1	y = 0.65x + 0.06	y = 1.32x + 0.00	1558
2	y = 0.79x + 0.03	y = 1.40x - 0.02	2853
3	y = 0.70x + 0.04	y = 1.13x + 0.01	1131
4	y = 0.67x + 0.04	y = 1.13x + 0.00	1033
5	y = 0.57x + 0.06	y = 1.08x + 0.02	1607
6	y = 0.28x + 0.08	y = 0.89x + 0.01	1716
7	y = 0.18x + 0.09	y = 0.81x + 0.03	1185
8	y = 0.25x + 0.08	y = 1.05x - 0.02	1845
		Total	12928

Table 8.2: Intermediate results on correlation for both MCP methods for the second experiment: April - June

Next to that, considerable differences in obtained models can be observed for the eight wind direction sectors. This applies to both MCP methods. For the LR method, the sectors 6, 7 and 8 usually have the lowest slope parameters α of around 0.2 - 0.3. The other five sectors have higher slope parameters. For the VR method, it is hard to spot a pattern in the distinctions that can be found over the direction sectors. The subdivision in wind direction sectors has been done for a reason, namely because of the presumption that different linear relationships exist and that wind direction has an influence on this. According to the results in this section and Appendix G, it can be said that this presumption is confirmed. Thirdly, the obtained models from both methods for certain sectors tend to deviate more from the rest of the sectors in that experiment when the concerning wind direction sectors contain a low amount of data points. This is especially the case for the models obtained from data that cover a quarter of a year, so for experiments 1 to 4. In line with this, it can be observed that sector 5 is the prevailing wind direction over the year, especially in the second half of the year. In the first half of 2019, the origin of the wind is more distributed over all sectors.

Sector	$y = \alpha x + \beta$	$y = \mu_{y} - \frac{\sigma_{y}}{\sigma_{x}} \mu_{x} + \frac{\sigma_{y}}{\sigma_{x}} x$	Data
#	Linear regression method	Variance ratio method	points
1	y = 0.39x + 0.08	y = 1.00x + 0.03	1095
2	y = 0.64x + 0.04	y = 1.15x + 0.00	1821
3	y = 0.56x + 0.05	y = 1.13x + 0.01	1987
4	y = 0.51x + 0.04	y = 1.00x + 0.00	3466
5	y = 0.81x + 0.04	y = 1.50x - 0.02	7733
6	y = 0.32x + 0.06	y = 1.18x - 0.01	4112
7	y = 0.22x + 0.09	y = 0.91x + 0.01	2876
8	y = 0.21x + 0.08	y = 0.84x + 0.00	2264
		Total	23354

Table 8.3: Intermediate results on correlation for both MCP methods for the sixth experiment: July - December

8.2. Results 91

8.2.3. Third step: Predict

In the linear models discussed above, the data of the reference site and the final prediction for the target site are represented by x and y, respectively. This prediction is subjected to the earlier introduced performance criteria μ_{norm} , σ_{norm} and χ^2_{norm} . For the first two criteria, a value of 1 is the target value since this indicates perfect alignment of the means or standard deviations compared in that experiment. For the chi-squared statistic, 0 is the desired value. Usually, a threshold is chosen to determine whether the difference between the observed data distribution and expected data distribution is statistically significant or not. Often, 0.05 is chosen to be this threshold, which is adopted here. Values above the threshold are seen to indicate that the difference between the predicted and the actual distribution of LiDAR 1 is too big. In Table 8.4, the results for all six experiments are presented. Next to that, Figures 8.3, 8.4 and 8.5 in this section show the obtained distributions for experiments 1, 4 and 5. The distributions from the other experiments can be found in Appendix H. It was decided to merge the separate wind direction sectors again to one distribution for two reasons: to arrive at representative yearly TI distributions again as were used too in Chapter 7 and for not having too many distributions to show in this chapter.

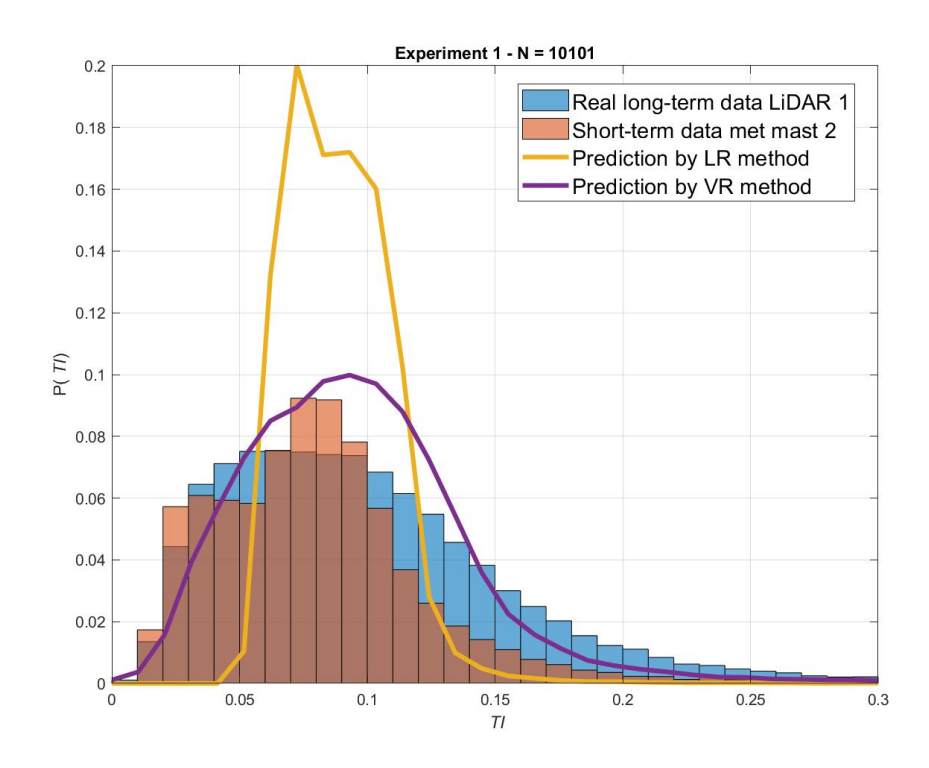


Figure 8.3: Prediction via both MCP algorithms for experiment 1

	Experiment # \rightarrow	1	2	3	4	5	6
LR method	$\mu_{ ext{norm}}$ $\sigma_{ ext{norm}}$ $\chi^2_{ ext{norm}}$	0.90 0.40 0.69	1.03 0.53 0.77	1.00 0.53 0.72	0.97 0.57 0.67	0.98 0.52 0.62	0.98 0.46 0.72
VR method	$\mu_{ ext{norm}}$ $\sigma_{ ext{norm}}$ $\chi^2_{ ext{norm}}$	0.98 1.23 0.06	1.01 1.27 0.07	0.99 1.28 0.08	1.02 1.39 0.04	0.99 1.33 0.04	0.98 1.25 0.08

Table 8.4: Resulting performance metrics of the six experiments for both MCP methods

Several things could be observed from Table 8.4 and the figures in this section. The figures show the short-term data distribution of met mast 2 that was used to establish the linear models in Tables 8.2, 8.3 and the tables in Appendix G in orange. Next to that, two predictions of the long-term data of LiDAR 1 are plotted as a line, as well as the actual long-term data in blue. Firstly, both MCP methods seem to be capable of predicting the mean of the long-term distribution with sufficient accuracy. For both methods and all experiments, the value of the normalized mean μ_{norm} is close to 1. The results are slightly better for the variance ratio method (VR), with values for μ_{norm} between 0.98 and 1.02. The values for the linear regression method (LR) show a bit wider range around 1. At first glance, no differences in results between the experiments with data lengths of 3 and 6 months can be observed for this performance metric.

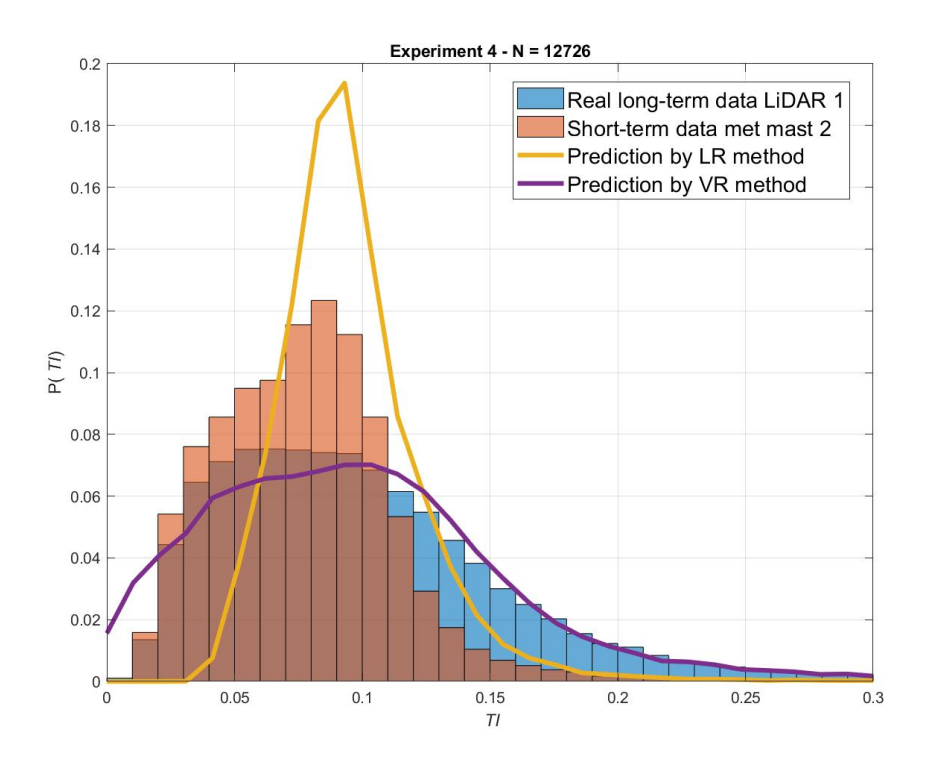


Figure 8.4: Prediction via both MCP algorithms for experiment 4

Next to that, patterns can be observed in the second performance metric too. On one hand, the LR MCP method consequently underestimates the standard deviation σ , leading to a σ_{norm} far below the target value of 1. Values in the range of 0.4 < σ_{norm} < 0.6 can be observed for the six executed experiments. This underestimation is inherent to the linear regression MCP method according to earlier research like [115]. Here is stated that this method tends to suffer from so-called mode reinforcement, which means that the prediction overestimates the distribution at the place of the mode in short-term distribution. This is exactly what can be observed in e.g. Figures 8.3 and 8.4. The mode is indicated by the highest orange histogram bin and falls below the top of the yellow graph. It can also be seen that the LR prediction distribution is much narrower than the actual distribution. The above described phenomenon was also encountered by other research regarding the same MCP methods applied to wind speed U [121], where mode reinforcement was also perceived. In this analysis, the mode reinforcement is even bigger than expected, given the high peaks in Figures H.1, H.2 and H.3. On the other hand, the VR method suffers from a consistent overestimation of standard deviation σ . This leads to σ_{norm} values higher than 1. In contrast to the LR method, the values are not so far from the target value, since the values for all six experiment fall in the range 1.2 - 1.4. In the figures in this section, it can be seen that the distribution predicted by the VR method is often close to the actual distribution.

8.2. Results 93

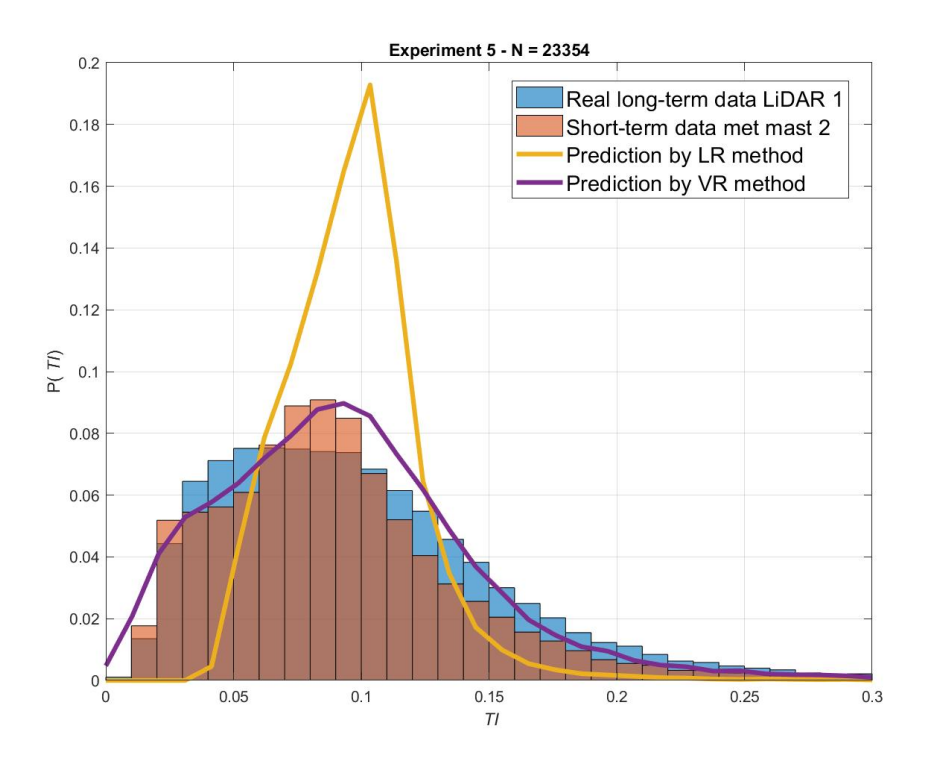


Figure 8.5: Prediction via both MCP algorithms for experiment 5

Furthermore, both predictions are in each experiment judged by how their artificial distribution matches with the actual long-term distribution via the normalized chi-squared statistic χ^2_{norm} . With a significance level of 0.05 or 5%, a threshold is set. This significance level is the probability of wrongly claiming that there is no difference between the observed (the MCP prediction) and expected (actual long-term distribution of the target site) values in the data, when there actually is a difference between both. Significance levels much higher than 0.05 indicate too big differences between both distributions. As already could have been thought of by observing the graphs in this section, the LR method fails to accurately predict the real long-term distribution of the target site. To be precise, it is way off. This is also evident from the results in Table 8.4, where the values for χ^2_{norm} from the LR method are very high. They range from 0.6 to 0.8, which means the predicted distribution is nowhere near like the actual distribution. There is again no clear distinction visible between the first four and the last two experiment, which indicates that the accuracy of the prediction does not prove to be dependant of the time frame length of the short-term data in a certain experiment. The above was expected since the unusual values for α and β in the correlations established by the LR method and the low R^2 values, indicating that the found linear relationships are relatively weak.

For the VR method however, the results are significantly better. Again, it can be observed in Figures 8.3, 8.4, 8.5, H.1, H.2 and H.3 that the purple graph is often quite close to the real long-term distribution indicated by the blue histograms. The fourth and fifth experiment show a value for $\chi^2_{\rm norm}$ lower than the discussed significance level of 0.05 and the results of the prediction for these experiment can therefore be considered statistically significant. The other four experiment show $\chi^2_{\rm norm}$ values between 0.06 and 0.09. This would strictly mean that the results of these experiments can not be accepted as statistically significant. It is however promising that the values approach the significance level of 0.05 to a quite close extent. It can be observed that the VR method also slightly suffers from the earlier explained mode reinforcement.

8.3. Discussion and conclusion

This chapter comprises of an analysis on the application of widely used Measure Correlate Predict (MCP) algorithms or methods on turbulence intensity time series data. Two operable and possibly useful methods were chosen: the linear regression (LR) method and the variance ratio method (VR). The application of MCP is prompted by the observed intra-annual variability of TI, which is elaborated on in Chapter 7 and the potential advantages of short and flexible measurement campaigns by means of LiDAR. A reference and target site were identified, namely the measurements from the met mast at location 2 and those of the LiDAR at location 1, respectively. Next to that, six experiments are constructed: four experiments each including a quarter of the year 2019 as short-term data and two including both halves of 2019 as short-term data. Furthermore, three performance metrics were introduced, namely the normalized mean μ_{norm} , the normalized standard deviation σ_{norm} and the normalized chisquared statistic χ^2_{norm} . Next to these, the resulting distributions are visually examined.

Several conclusions can be drawn from results of the analysis in this chapter. Firstly, the LR MCP method seems not to be suitable for predicting long-term TI distributions based on linear models obtained from correlating short-term data from reference and target site. After obtaining linear models with often odd values for slope parameter α and offset β and coefficient of determination R^2 values that can be considered as relatively low, it was already suspected that the LR method would not be suitable to apply on TI data. A graphical representation of the correlation step is shown in Figures G.1 and G.2 in Appendix G, in where the linear models obtained via both MCP methods are presented for two different wind direction sectors. The suspected unsuitability of the LR method is confirmed by the final results in the prediction step. The prediction of the mean of the distribution by this method was not bad, but the resulting values for μ_{norm} were already not precise enough throughout the six experiments. It could be seen that the second performance metric, σ_{norm} , performed even worse. The linear regression method heavily underestimates the standard deviation of the long-term distribution compared to the actual long-term distribution, resulting in unacceptable low values for σ_{norm} . It has been observed that for all experiments, this MCP method suffers from so-called mode reinforcement. This is a known drawback from this method and applying this method on TI data even worsened this phenomenon. It results in extreme peaks in the predicted distribution above the mode (the highest histogram bin) of the used shortterm distribution. Keeping the above in mind and looking into the figures in Subsection 8.2.3 and Appendix H, it comes as no surprise that the results from the LR method for the last performance metric are disappointing. The resulting values for χ^2_{norm} confirm the failure of the LR method to predict the long-term TI distribution on the basis of the found correlations between short-term data from reference and target site.

Next to that, the variance ratio method (VR) was included in the analysis. The VR MCP method is brought by other research as an improvement of the LR method when applied to average wind speed time series data. Focusing on TI data here, the VR shows reasonable results too, which are much more satisfying than the results obtained with the LR method. Firstly, it is even better in predicting the mean of the actual long-term TI distribution than the LR method is. It is not more than 2% off for each experiment. Although the VR method is better in predicting the standard deviation, the resulting values for σ_{norm} are not as close to 1 as desired. On average, a normalized standard deviation of around 1.25 is found throughout the experiments, which indicates a consistent overestimation over the standard deviation. It is seen that for the application of MCP on U, the VR method often fairly well predicts the standard deviation, but is not as spot on as targeted. This is also the case in this analysis.

To continue to the last and possibly most important performance metric, the normalized chi-squared statistic χ^2_{norm} shows satisfying but not the best results. For experiment 4 and 5, the resulting value is just under the usual significance level of 0.05. However, for the other experiments the value for the chi-squared statistic exceeds this statistical threshold. To conclude, the results for prediction via the variance ratio method are not unsatisfactory. Nevertheless, the overestimation of σ and the varying results in the examination of the ob-

tained distributions via the chi-squared goodness of fit test leave room for optimization of the use of this MCP method on *TI* data.

Thirdly, another interesting notion emerged from this analysis. The experiments are subdivided in groups with a short-term data length of 3 (experiments 1, 2, 3 and 4) and 6 (experiments 4 and 5) consecutive months. One might expect better results for all three performance metrics in experiments 5 and 6, but this is actually not the case. All experiments have comparable results; there is no distinction visible between both groups of experiments. It is suspected that the shape of the short-term distributions is of more influence on the obtained linear models and therefore final predictions than the time series length of the short-term data sets.

Lastly, some reflection on the analysis in this chapter is appropriate. It can be noted that the long-term data for target and reference site has a length of only 1 year, where ideally longer periods are used in MCP. However, the goal of this analysis was mainly to study the prediction power of certain MCP methods on TI data and not to arrive at the most precise long-term turbulence intensity distribution at the location concerned. Next to this, some improvements on the executed analysis can be identified. More years and seasons of the same location could be included and other locations could be considered to draw more firm conclusions. Furthermore, one could opt for an increase in wind direction sectors. The choice for eight sectors is a trade-off between precision and enough data per wind direction sector and can be topic of discussion. Finally, turbulence intensity level differentiated linear models could be a possible addition. Here, different linear models are obtained not only per wind direction sector, but also per turbulence level inside a certain wind direction bin. One could e.g. distinguish low, medium and high turbulence ranges to improve the accuracy of the MCP prediction. Additionally, the opportunity exists to make subdivisions based on wind speed U, the parameter that is coupled to every TI value.



Conclusion and discussion

In this research, attempts were made to address common obstacles that can be in the way of further implementation and acceptation of LiDAR in wind site assessment, with a focus on the turbulence parameter turbulence intensity T1. Firstly, a data analysis approach was taken to evaluate the measurement differences between met masts and continuous wave ZX300 LiDARs. Both techniques use different measurement principles, as elaborated on in Subsection 2.2.2, which can cause biases between both. Two locations in wind farm "Windplan Blauw" were used for this comparison. Secondly, a sensitivity analysis was performed on the influences of turbulence intensity on the fatigue lifetime damage of a representative onshore wind turbine. The order of magnitude of the biases in TI found in the LiDAR met mast comparison were used as an input for the simulations conducted with the help of three NREL developed tools. Thirdly, the intra-annual variability of TI was examined and found and used as driver for a Measure Correlate Predict study, focusing on TI data instead of ordinary U data. This direction is prompted by the inherent flexibility of LiDAR devices. These could yield financial benefits by conducting short measurement campaigns by means of Li-DAR, ultimately totally replacing the current standard of erecting increasingly higher en more expensive met masts. In relation to this, extrapolation of short-term TI data via MCP should be and was examined.

The LiDAR met mast comparison was subdivided in a basic analysis and main analysis, the latter specifically addressing TI. In the first, several parameters regarding measuring wind characteristics by means of LiDAR were treated. To start, it was found that the data availability of both LiDARs was good, i.e. around 98-99%. However, the data availability declines with increasing height, something met masts do not suffer from. Next to this, the horizontal 10-minute averaged wind speed U and standard deviation $\sigma_{\rm u}$ were assessed, as building blocks of turbulence intensity. For U, the deviation in average is negligible for both LiDAR met mast pairs. Also, OLS linear regression shows close to excellent results with R^2 values between 0.98 and 0.99. Together, this confirms the hypothesis that LiDAR is perfectly suitable for measuring 10-minute averaged wind speed.

On the flip side, the biases found for standard deviation σ_u are higher. Small, but not insignificant differences were found here, which could cause deviating TI values later on. Thirdly, both Weibull parameters were estimated via a least squares fit for both LiDAR met mast pairs. It came out that LiDAR measured wind speed data is perfectly suitable for the determination of the Weibull distribution. Lastly, the wind direction of LiDAR and met mast was compared visually. Both pairs showed good agreement in this at several heights. The most noticeable observation was a 180° shift throughout the LiDAR measurements. This happens more often according to other literature and this data should be and is filtered.

Concerning T1, several conclusions can be drawn too. LiDAR seems to consistently overestimate turbulence intensity; the μ_{TI} is significantly higher for LiDAR measurements from all height compared to the accompanying met masts. This bias also increases with height. With the help of OLS linear regression, it was found that filtering data with a threshold U > 03 m/s make a considerable difference in results for α , β and R^2 . The overall overestimation of TI is confirmed by this analysis and tells us that this mainly happens in the low wind speed region. Next to this, the bias between both sources was found to be higher for wind coming from the surrounding land for LiDAR 1 and met mast 1, compared to wind coming from the nearby lake. The origin of the inaccuracy of LiDAR measured TI was found not to be solely caused by U and σ_{11} . Where the first shows almost perfect agreement, the latter factor shows a consistent overestimation of 2 - 5% for all heights and both pairs. However, since the differences in TI are bigger and cannot entirely be attributed to the σ_{11} biases, the internal LiDAR correction factor \mathcal{C} comes into play. Observing the available data, it is concluded that the definition of this factor is suboptimal. Therefore, it is recommended that this factor will be a function of height, which it now is not above 90 m. The current course of C is depicted in Figure 5.14, as well a possible alteration. A simple measure on one hand, but one that needs more verification and adjustment on the other hand.

Furthermore, a proposition was made for the use of transience $\tau_{\rm m}$ in measuring turbulence. Replacing the one-point statistic $\sigma_{\rm u}$ with a two-point statistic that accounts more for variety within a 10 minute interval possibly gives a better representative of turbulent structures. Since LiDAR is struggling with accurately measuring $\sigma_{\rm u}$ and the use of $\tau_{\rm m}$ does not include difficult calculations, it is worth to further investigate the possibilities of transience, e.g. by means of a case study such as in Appendix C.

Different levels of *TI* were used as an input for simulation in TurbSim, FAST and MLife to arrive at fatigue lifetime damage for the representative 5 MW NREL wind turbine, focusing on tower and blades. Firstly, for the turbine tower the stresses concentrate at the tower base. It was also found that choosing the right Wöhler coefficient is of much larger influence than the level of *TI*. Most importantly, it was found that the fatigue lifetime damage due to stresses from side-to-side bending moments is smaller than that due to stresses from fore-aft bending moments. But the first is much more sensitive for *TI* increments than the latter, over 80% versus around 10% respectively. Secondly, for the turbine blades the stresses are even orders of magnitude higher towards the blade root. On the contrary of the tower, the fatigue damages due to stresses from in-plane and out-of-plane bending moments are of the same order and also very low. It was found that the fatigue damage due to stresses from in-plane/edgewise bending moments only increase with a few percents per *TI* increment, where the fatigue damage due to stresses from out-of-plane/flapwise bending moments is way more sensitive to turbulence. Here, 40% more damage is observed per *TI* increment.

The suspected intra-annual variability of TI at both locations of interest was confirmed by analyzing year-long LiDAR measured TI data. The yearly distribution of μ_{TI} seems to follow a bell-shaped curve, with the top around June. Next to this, the monthly TI distributions do differ significantly from the yearly ones. During summer months, the monthly TI distribution is shifted to the right and in winter months vice versa. Somewhat surprisingly, the origin of these patterns does not lie in a standard deviation $\sigma_{\rm u}$ varying over the year, since this parameter does not really show a seasonal pattern. However, the average wind speed U does. This opens the possibility to assess the usability of MCP on TI data, what is done after this.

Six experiments were constructed in this MCP study, each for every quarter and half-year of 2019, forming the short-term data set of the whole. Each experiment further includes a subdivision per wind direction sector of 45° each. In addition, the linear regression (LR) and variance ratio (VR) MCP method were examined. The LiDAR at location 1 in wind farm "Windplan Blauw" is the target site here, where the met mast at location 2 serves as reference site. It was found that the LR method is completely unsuitable for the intended purpose.

The obtained linear models are weak, it performs moderate to poor on the three performance metrics μ_{norm} , σ_{norm} and χ^2_{norm} , indicating the prediction based on this method deviates enormously from the actual long-term data. It is therefore discouraged to apply the LR method on (short-term) TI data.

On the other hand, the VR method performed fair to good on all three performance metrics, something which is confirmed by visual examination of the predicted distribution. This was already suspected after obtaining the linear models for both methods, since the slope parameters α and offsets β from the VR method seemed to make more sense than those from the LR method. Next to this, the LR method suffered from poor R^2 values accompanying the linear regression, something which does not play a role in the VR method. Also for the VR method, there is still some room for improvement. This analysis could be redone with longer data sets and at locations with different circumstances. Next to this, more wind direction sectors and introducing several turbulence and/or wind speed U levels inside each wind direction bin could possibly enhance the results of the VR MCP method on TI data.



Application of LR and VR MCP method on data sets with low coefficient of determination

The below example of the application of both LR and VR Measure Correlate Predict methods on data with different values for coefficient of determination R^2 attempts to clarify the sometimes big differences between obtained linear models from both methods. For this example, two different data sets are randomly generated. In the first data set, a clear relationship is visible in the point cloud in Figure A.1. This data set would yield a R^2 value close to 1. It can be seen that both MCP methods result in a comparable linear model, since the yellow and red line are of similar fashion.

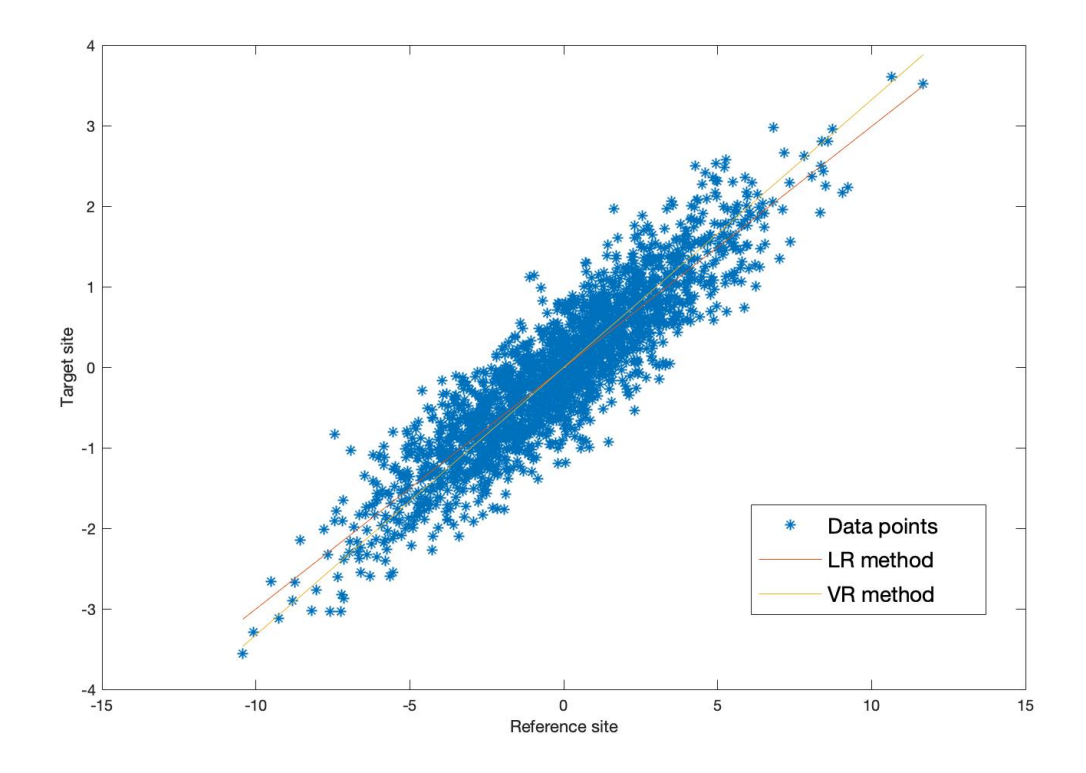


Figure A.1: Data set with high \mathbb{R}^2 in linear regression

On the contrary, the point cloud in Figure A.2 shows far less relation between reference and target site. This implies a relatively low value for R^2 . It can be seen that the difference between both obtained linear models is big. The latter is something that can happen when both methods are applied to data sets that are somewhat alike to the one in Figure A.2, which happens in Chapter 8.

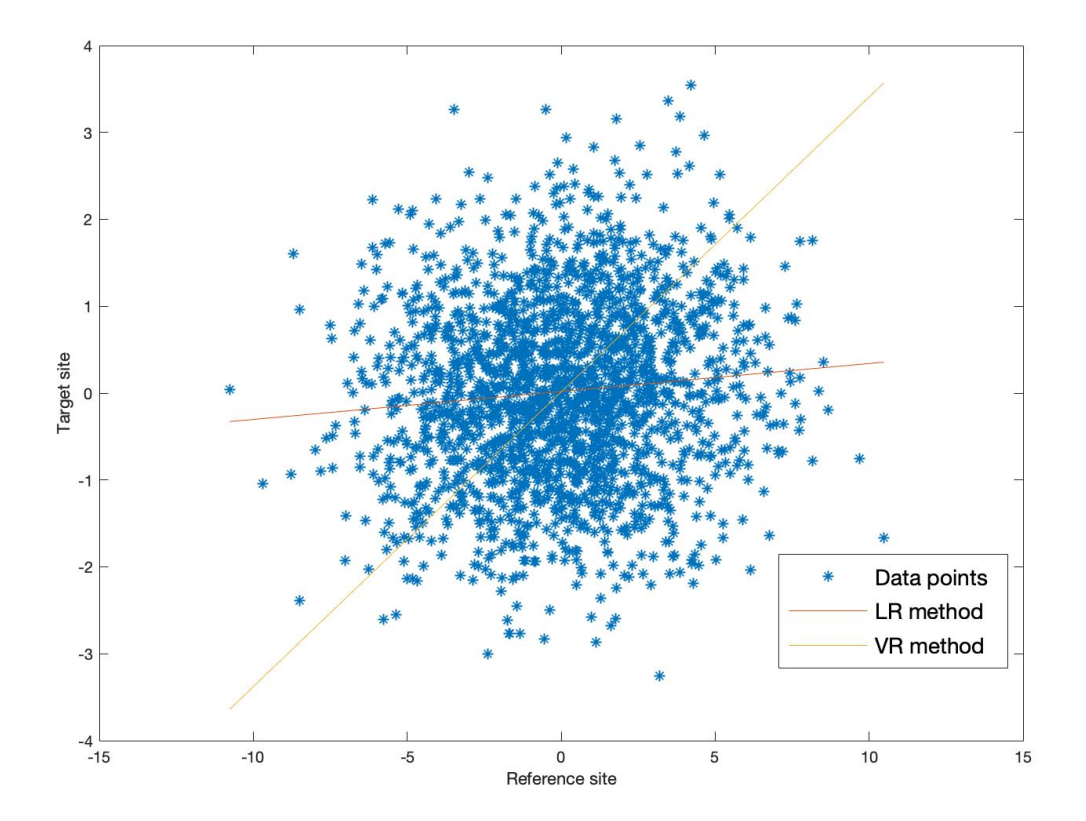


Figure A.2: Data set with low R^2 in linear regression



Least-squares fit Weibull parameters

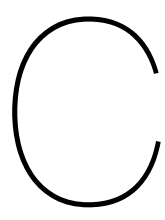
The wind speed distribution at a certain location is expected to be Weibull distributed, an assumption that is widely used in wind energy science and is adopted here too. This gives the opportunity to determine the distribution of the local wind speed via various algorithms [111]. Three of the most commonly used algorithms are the European Wind Atlas Method, the Maximum Likelihood Method and the Least-squares Fit Method [53]. For being easy to implement and reliable, the latter was adopted in this research and is elaborated on below.

The least-squares fit method to estimate the Weibull parameters works via the principle of altering the cumulative probability distribution function from an exponential function to a linear function. Since this is done by taking the logarithmic twice, the method is also known as the log-log method. The starting point to find the Weibull shape parameter k and Weibull scale parameter k is the cumulative probability distribution function in Equation B.1. This formula is related to the Weibull probability density function in Equation 5.1.

$$F(U,k,a) = 1 - e^{-\frac{U}{a}^{k}}$$
 (B.1)

By isolating the e and taking the logarithmic of the whole function twice, one ends up with a new formula, shown in Equation B.2. This formula has the form of a linear equation y = ax + b, as also discussed in Subsection 2.3.2. When the measured wind speeds U are plotted in the obtained form of Equation B.2 and a linear fit is taken as elaborated on in the same Subsection, one is able to determine both Weibull parameters.

$$\ln(-\ln(1 - F(U, k, a))) = -k\ln(U) + k\ln(a)$$
(B.2)



An example case study on the versatility of transience

The findings on the inherent inaccuracy of turbulence intensity TI measured by LiDAR compared to met masts in Chapter 5 did not only bring up ideas to handle or mitigate this inaccuracy of TI from LiDAR itself by for instance an alteration of the internal correction factor C, but also induced a discussion whether TI is the best parameter to represent the short-term variabilities in the horizontal wind speed U after all. A possible layout for a case study is proposed to give handles for further research to confirm the usability of transience and emphasize the possible advantages of using transience $\tau_{\rm m}$ over $\sigma_{\rm u}$. The argumentation for conducting such case study is given in Section C.1, after which the setup of the case study is treated in Section C.2.

C.1. Argumentation for and setup of case study

The idea for the proposition of the use of transience τ_m over standard deviation σ_u originated from the inherent inability of LiDAR to achieve the same accuracy in measuring σ_u than met masts. This was researched in Chapter 5 and confirmed that the consistent overestimation of σ_u was one of the reasons for the overestimation of common turbulence indicator TI by LiDAR. The combination of the matter in Chapter 5 and the determination of the sensitivity of fatigue lifetime damage of Dutch modern multi-megawatt turbine for TI by means of rain flow counting in Chapter 6, led to the question whether it is more logical to involve the mean wind speed μ in the representation of turbulence in the wind, in favour of neighboring data points. The hypothesis stated in this chapter that transience might be a better representative of turbulent variability in the wind than standard deviation leans on a now known set of three formulas in Equation C.1. The formula for σ_u is part of that for TI. The formula for τ_m is quite similar to that of σ_u , but contains an important difference: data points are paired to their neighboring predecessor and not to the mean μ of the 10 minute interval.

$$TI = \frac{\sigma_u}{\overline{U}}$$
 $\sigma_u = \sqrt{\frac{1}{N} \sum_{i=1}^{N} (x_i - \mu)^2}$ $\tau_m = \sqrt{\frac{1}{N} \sum_{i=1}^{N} (x_i - x_{i+m})^2}$ (C.1)

The first reason to favour $\tau_{\rm m}$ over $\sigma_{\rm u}$ as a representative for turbulence or variability in the wind speed is that it is believed that transience can distinguish various situations of turbulence from each other, where standard deviation is not able to do this. In other words, 10 minute intervals with the same value of $\sigma_{\rm u}$ are suspected to have different values of $\tau_{\rm m}$. This would make transience a better indicator for variability in the horizontal wind speed U than the standard deviation and therefore seriously question the use of TI. One could think of multiple sets of 10 minute intervals with 600 1 Hz wind speed U data points that have the same mean \overline{U} and standard deviation $\sigma_{\rm u}$, but are otherwise very different. These sets would for that reason end up with the same TI value, which should be a good indicator for the variability of the wind speed. But in reality it might not be the best option, since these sets can differ significantly in variability and thereby turbulence.

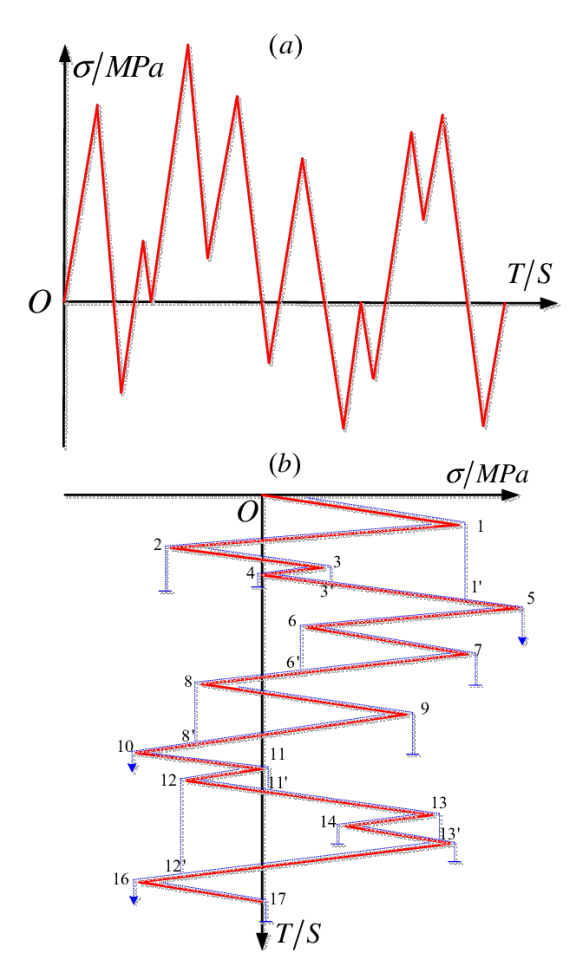


Figure C.1: The principle of rainflow-counting used on stress cycles for fatigue determination [35]

The second reason favour τ_m over σ_u as a turbulence indicator is related to the concept of rainflow-counting. This algorithm is used in fatigue damage determination and reduces spectra of stress cycles into equivalent sets of stress reversals. It is mentioned in Chapter 6 too and can extract smaller interruption cycles from a sequence to model the material memory effect [114]. It is based on a simplification of reality, but since is allows the calculation of the fatigue lifetime damage for each rainflow cycle by means of the widely accepted Palmgren-Miner's rule of Equation 6.5, it is the most used approach for the determination of material fatigue from stress cycles [96]. This rule is elaborated on in Section 6.1.3. Figure C.1 visualises the concept of rainflow-counting. A spectrum of stresses over time is seen at the top of the figure. Below, the stresses are subdivided into equivalent sets of stress reversals.

The rainflow-counting algorithm is based on adjacent stress values and influenced by variation of these stresses. These stresses vary with changing loads, which in their turn vary with wind speed U via the formula for thrust T_R from Equation 2.16. This highlights the relationship between the determination of fatigue via rain-flow counting and variations in the wind speed, also called turbulence. Because of the use of adjacent data points for τ_m , this parameter is suspected to be more suitable for establishing clear relationships between variability of the wind and fatigue damage or damage equivalent loads of wind turbine parts than σ_u .

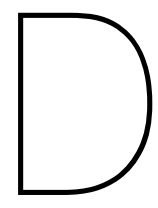
An additional reason for this case study relates to the following. TI values between 0.1 and 0.13 refer to a neutral atmosphere, lower values to a stable atmosphere and higher values to an unstable atmosphere, according to Table 2.1. These stability classes therefore also correlate to lower, average and higher variability of the wind. This cannot be translated directly to similar sets of values for σ_u , since \overline{U} is also involved in the formula for TI. However, low variability in the wind is considered to be represented by σ_u values ranging from 0.1 to 0.5 m/s. Average variability ranges from approximately 0.5 to 1 m/s and higher values of σ_u indicate high variability [62]. Although it is sure that transience τ_m will increase as a function of neighboring (turbulent) variability, it is not known how the spectrum of values should be interpreted. The proposed case study can help to establish an interpretation of a new spectrum of turbulent variability based on transience.

C.2. Setup case study

An example case study on transience is given here, in which several 10 minute intervals are examined. Normally, the precise content thereof is not given that much attention, that often goes out to the 10 minute averaged statistics of the measurement data. However, in this case study a closer look can be taken at the 1 Hz measurements of which the 10 minute averaged statistics are built from. The suspicion exists of transience $\tau_{\rm m}$ being a more precise and better representative of turbulent structures in the wind than $\sigma_{\rm u}$. This hypothesis can be tested with this case study. For this purpose, several 10 minute intervals with the same value for $\sigma_{\rm u}$ have to be chosen to evaluate these intervals for transience $\tau_{\rm m}$. 10 minute intervals with varying levels of 10 minute averaged standard deviation $\sigma_{\rm u}$ should be included too in the case study, as well as intervals with different levels of horizontal wind speed U. These distinctions should be made to assess the usability of transience for different levels of $\sigma_{\rm u}$ and U and thereby provide a complete picture of the use of transience in the usual practices of wind site assessment. Table C.1 gives an overview of an example selection of 10 minute intervals and their corresponding values of $\sigma_{\rm u}$ and U.

#	Timestamp interval	Standard deviation $\sigma_{\sf u}$	Mean wind speed $\it U$
1	e.g. 11.30 - 11.40 @ 10-11-2019	0.60	7.0
2	-	0.60	7.0
3	-	0.60	12.0
4	-	0.60	12.0
5	-	1.00	9.0
6	-	1.00	9.0
7	-	1.00	14.0
8	-	1.00	14.0
9	-	1.80	8.0
10	-	1.80	8.0
11	-	1.80	16.0
12	-	1.80	16.0

Table C.1: Overview of an example selection of 10 minute intervals with their corresponding values for standard deviation and mean horizontal wind speed over that interval



TurbSim input file

```
TurbSim Input File. Valid for TurbSim v1.06.00, 21-Sep-2012
                             ---Runtime Options--
                                                                                          - First random seed (-2147483648 to 2147483647)

- Second random seed (-2147483648 to 2147483647) for intrinsic pRNG, or an alternative pRNG: "RanLux" or "RNSNLN"

- Output hub-height turbulence parameters in binary form? (Generates RocotName.ln)

- Output hub-height turbulence parameters in formatted form? (Generates RocotName.dat)

- Output hub-height turbulence parameters in formatted form? (Generates RocotName.dat)

- Output hub-height time-series data in ReroDyn form? (Generates RocotName.bh)

- Output full-field time-series data in ILADED/AeroDyn form? (Generates RocotName.wnd)

- Output tower time-series data; (Generates RocotName.tvr)

- Output tower time-series data? (Generates RocotName.tvr)

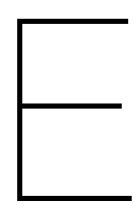
- Output full-field time-series data in formatted (readable) form? (Generates RocotName.u, RocotName.v, RocotName.w)

- Output coherent turbulence time steps in AeroDyn form? (Generates RocotName.cts)

- Clockwise rotation looking downwind? (used only for full-field binary files - not necessary for AeroDyn)

- Scale IEC turbulence models to exact target standard deviation? [0=no additional scaling; l=use hub scale uniformly; 2=use individual scales]
           2318573
                                                             RandSeedl
                                                             RandSeed2
           False
           False
                                                              WrFHHTP
           False
9 True
10 False
11 True
12 False
13 False
14 True
15 0
16
17 -----
18 30
20 0.05
21 600
22 500
23 90
24 160.00
25 160.00
26 0
27 0
28 -----
28 -----
31 "1-ED3"
32 "9"
31 "1-ED3"
32 "9"
31 "1-ED3"
34 default
36 100
37 8.2
38 default
30 0.2
40 0.03
                                                             WrBLFF
                                                             Wradtwr
Wrfmtff
Wract
                                                             Clockwise
ScaleIEC
                             --Turbine/Model Specifications--
                                                                                            el Specificati
NumGrid_Z
NumGrid_Y
TimeStep
AnalysisTime
UsableTime
HubHt
GridHeight
GridWidth
VFlowAng
                                                             VFlowAng
HFlowAng
```

Figure D.1: Graphic of one of the used TurbSim input files



FAST input file

```
- FAST v8.16.* INPUT FILE --
FAST Certification Test #18: NREL 5.0 MW Baseline Wind Turbine (Onshore)
-----SIMULATION CONTROL
                                                                                                  - Echo input data to <RootName>.ech (flag)
                                                                                                    - Error level when simulation should abort (string) {"WARNING", "SEVERE", "FATAL"} - Total run time (s)
   "FATAL"
                                               Abort Level
              0.00625
                                                                                                     - Recommended module time step (s)
                                                   InterpOrder - Recommended module time step (s)
InterpOrder - Interpolation order for input/output time history (-) {l=linear, 2=quadratic}
InterpOrder - Interpolation order for input/output time history (-) {l=linear, 2=quadratic}
InterpOrder - Number of correction iterations (-) {0=explicit calculation, i.e., no corrections}
Interpolation order (-) {0=explicit calculation, i.e., no corrections}
Interpolation (-) {0=e
                                               InterpOrder
                    1E+06
                                               UJacSclFact
                                               CompElast
                                               CompInflow
                                               CompAero
                                               CompHydro
                                                                                                   - Compute sub-structural dynamics (switch) {0=None; 1=SubDyn}
- Compute mooring system (switch) {0=None; 1=MAP++; 2=FEAMcoring; 3=MoorDyn; 4=OrcaFlex}
- Compute ice loads (switch) {0=None; 1=IceFloe; 2=IceDyn}
                                               CompSub
                                               CompMooring
                                              Complice ----- INPUT FILES -
"SNW_Baseline/NRELOffshrBslineSNW_Onshore_ElastoDynT17.dat" EDFile - Name of file containing ElastoDyn input parameters (quoted string)
"SNW_Baseline/NRELOffshrBslineSNW_BeamDyn.dat" BDBldFile(1) - Name of file containing BeamDyn input parameters for blade 1 (quoted string)
"SNW_Baseline/NRELOffshrBslineSNW_BeamDyn.dat" BDBldFile(2) - Name of file containing BeamDyn input parameters for blade 2 (quoted string)
"SNW_Baseline/NRELOffshrBslineSNW_BeamDyn.dat" BDBldFile(3) - Name of file containing BeamDyn input parameters for blade 2 (quoted string)
"SNW_Baseline/NRELOffshrBslineSNW_InflowWind T111.dat" InflowFile - Name of file containing inflow wind input parameters (quoted string)
"SNW_Baseline/NRELOffshrBslineSNW_Onshore_AeroDyn15.dat" AeroFile - Name of file containing aerodynamic input parameters (quoted string)
"unused" ServoFile - Name of file containing control and electrical—drive input parameters (quoted string)
"unused" SubFile - Name of file containing sub-structural input parameters (quoted string)
"unused" SubFile - Name of file containing sub-structural input parameters (quoted string)
"unused" MooringFile - Name of file containing in put parameters (quoted string)
"unused" For File - Name of file containing in put parameters (quoted string)
"unused" For File - Name of file containing in put parameters (quoted string)
"unused" For File - Name of file containing in put parameters (quoted string)
"unused" For File - Name of file containing in put parameters (quoted string)
                                               IceFile - Name of Tile
   "unused"
                                                                                                      - Name of file containing ice input parameters (quoted string)
                                                                                                     - Print summary data to "<RootName>.sum" (flag)
- Amount of time between screen status messages (s)
                                               SttsTime
                                               ChkptTime
DT_Out
TStart
                                                                                                    Amount of time between creating checkpoint files for potential restart (s)

- Time step for tabular output (s) (or "default")

- Time to begin tabular output (s)
                    99999
                                                                                                     - Format for tabular (time-marching) output file (switch) {1: text file [<RootName>.out], 2: binary file [<RootName>.outb], 3: both}
- Use tab delimiters in text tabular output file? (flag) {uses spaces if false}
- Format used for text tabular output, excluding the time channel. Resulting field should be 10 characters. (quoted string)
                                3
                                               OutFileFmt
                                               TabDelim
                                               OutFmt - roll
------ LINEARIZATION -
- Linear
   ES10.3E2"
                                                                                                  False
                              30,
                                               LinInputs
                                               LinOutputs
LinOutJac
                                1
False
                                               LinOutMod
                                                      ---- VISUALIZATION ---
                                               WrVTK
VTK_type
VTK_fields
                                                                                                   - VTK visualization data output: (switch) {0=none; l=initialization data only; 2=animation}
- Type of VTK visualization data: (switch) {1=surfaces; 2=basic meshes (lines/points); 3=all meshes (debug)} [unused if WrVTK=0]
- Write mesh fields to VTK data files? (flag) {true/false} [unused if WrVTK=0]
true
                           15
                                               VTK_fps
                                                                                                     - Frame rate for VTK output (frames per second) [will use closest integer multiple of DT] [used only if WrVTK=2]
```

Figure E.1: Graphic of one of the used FAST input files

Chi-squared test example

An example on the normalized chi-squared statistic is given here. Note that random numbers are used. The data contains expected and observed values. In relation to the content of this thesis, the expected data represents the data from the met masts and the observed data represents the data of the LiDARs. The data is subdivided in five bins, which have no meaning here. In this thesis, these bins represent the groups of values for TI with a bin width of 0.01. A histogram of the counted data is depicted in Figure F.1, showing that bin values between 160 and 240 for both expected and observed values. The total number of data points for the expected data N_E and the observed data N_O is 970 and 934, respectively. A different number of total data points in two time series spanning the same time period can in real life be caused by missing data. This can happen with met masts or LiDARs for various causes, as discussed in Chapter 5.

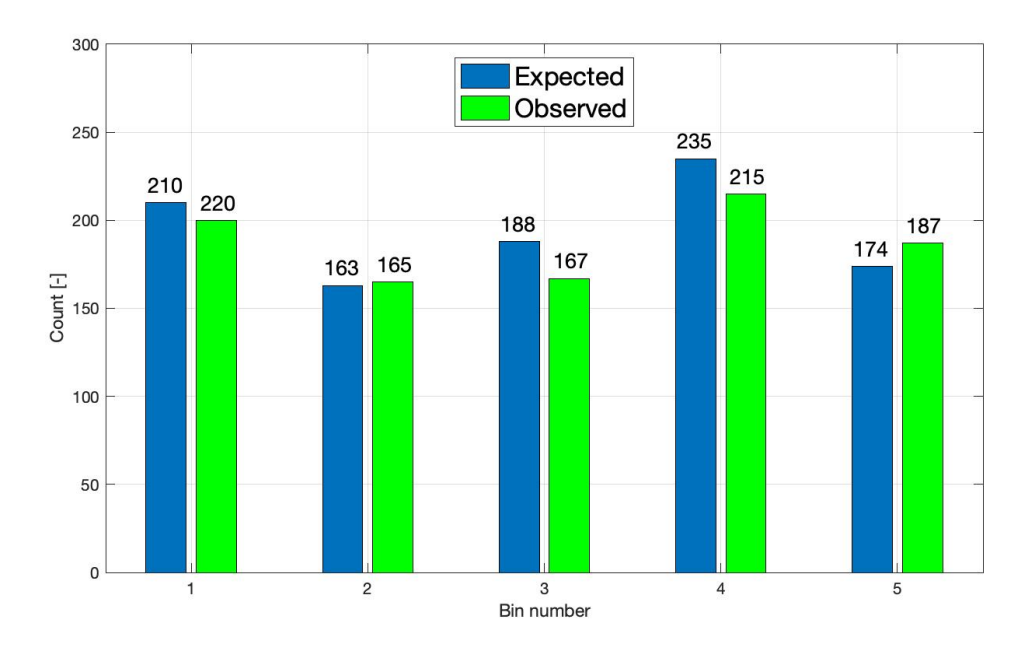


Figure F.1: Bin counts of expected and observed data points

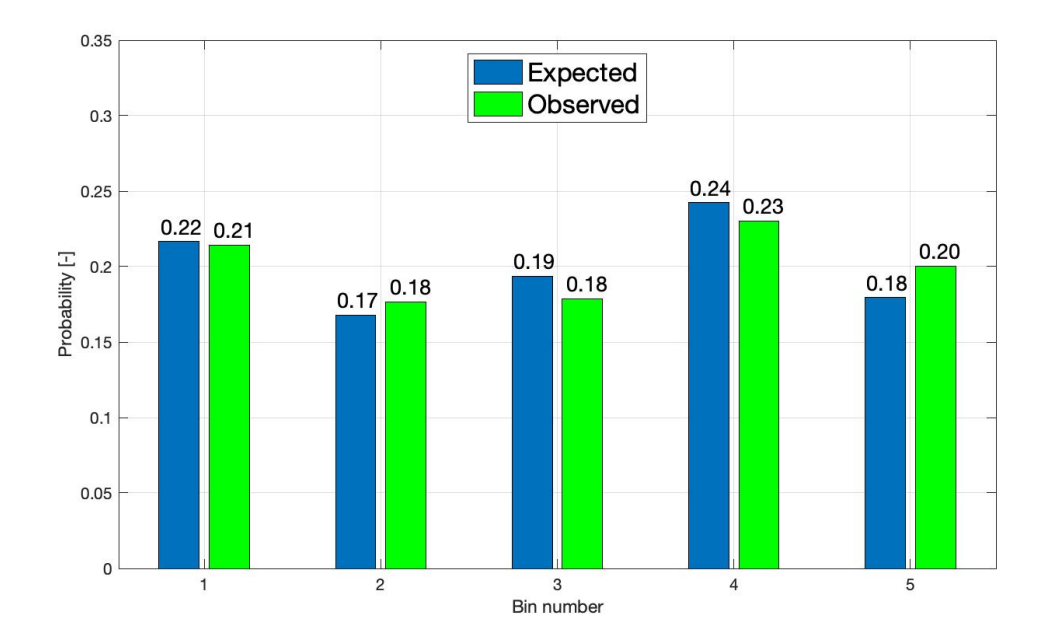


Figure F.2: Probability of expected and observed data points

When the bin counts from Figure F.1 are converted to probabilities, the results is as in Figure F.2. For both expected and observed values, this is simply done by dividing the bin count of all five bins by N_E and N_O , respectively. One now has both fractions that appear in Equation 8.4 and can determine the value of $\chi^2_{\rm norm}$ for each bin. The last step to arrive at the final normalized chi-squared statistic is the addition of the $\chi^2_{\rm norm}$ value for each bin M, in this case M=5. This is shown in Equation F.1 and adds up to a safe and desired value of 0.01, meeting the commonly used threshold of 0.05.

$$\chi_{\text{norm}}^2 = \sum_{i=1}^M \frac{\left(O_i/N_O - E_i/N_E\right)^2}{E_i/N_E} = 0.0017 + 0.0005 + 0.0012 + 0.0006 + 0.0024 = 0.01$$
 (F.1)



Overview intermediate results for correlation step in MCP

Sector	$y = \alpha x + \beta$	$y = \mu_{y} - \frac{\sigma_{y}}{\sigma_{x}} \mu_{x} + \frac{\sigma_{y}}{\sigma_{x}} x$	Data
#	Linear regression method	Variance ratio method	points
1	y = 0.14x + 0.10	y = 0.55x + 0.07	534
2	y = 0.30x + 0.08	y = 1.05x + 0.02	466
3	y = 0.37x + 0.06	y = 1.06x + 0.02	684
4	y = 0.33x + 0.06	y = 0.94x + 0.01	1072
5	y = 0.40x + 0.07	y = 0.92x + 0.04	2250
6	y = 0.29x + 0.06	y = 0.91x + 0.01	2069
7	y = 0.23x + 0.05	y = 0.98x - 0.01	1721
8	y = 0.10x + 0.06	y = 0.53x + 0.01	1305
		Total	10101

Table G.1: Intermediate results on correlation for both MCP methods for the first experiment: January - March

Sector	$y = \alpha x + \beta$	$y = \mu_{y} - \frac{\sigma_{y}}{\sigma_{x}} \mu_{x} + \frac{\sigma_{y}}{\sigma_{x}} x$	Data
#	Linear regression method	Variance ratio method	points
1	y = 0.36x + 0.08	y = 0.82x + 0.04	656
2	y = 0.58x + 0.04	y = 1.01x + 0.01	708
3	y = 0.71x + 0.03	y = 1.19x + 0.00	763
4	y = 0.47x + 0.05	y = 0.89x + 0.01	1030
5	y = 0.79x + 0.04	y = 1.50x - 0.01	3384
6	y = 0.28x + 0.08	y = 1.12x + 0.00	2581
7	y = 0.26x + 0.08	y = 0.87x + 0.02	1799
8	y = 0.20x + 0.09	y = 0.86x + 0.00	1707
		Total	12628

Table G.2: Intermediate results on correlation for both MCP methods for the third experiment: July - September

Sector	$y = \alpha x + \beta$	$y = \mu_{y} - \frac{\sigma_{y}}{\sigma_{x}} \mu_{x} + \frac{\sigma_{y}}{\sigma_{x}} x$	Data
#	Linear regression method	Variance ratio method	points
1	y = 0.64x + 0.07	y = 1.85x - 0.03	439
2	y = 0.79x + 0.03	y = 1.45x - 0.02	1113
3	y = 0.38x + 0.06	y = 1.08x + 0.02	1224
4	y = 0.56x + 0.04	y = 1.23x - 0.01	2436
5	y = 0.84x + 0.04	y = 1.50x - 0.01	4349
6	y = 0.28x + 0.06	y = 1.55x - 0.04	1531
7	y = 0.26x + 0.08	y = 1.37x - 0.05	1077
8	y = 0.17x + 0.07	y = 0.81x + 0.00	557
		Total	12726

Table G.3: Intermediate results on correlation for both MCP methods for the fourth experiment: October - December

Sector	$y = \alpha x + \beta$	$y = \mu_{y} - \frac{\sigma_{y}}{\sigma_{x}} \mu_{x} + \frac{\sigma_{y}}{\sigma_{x}} x$	Data
#	Linear regression method	Variance ratio method	points
1	y = 0.31x + 0.09	y = 0.89x + 0.04	2101
2	y = 0.60x + 0.05	y = 1.27x - 0.01	3319
3	y = 0.53x + 0.05	y = 1.09x + 0.01	1815
4	y = 0.52x + 0.05	y = 1.04x + 0.00	2105
5	y = 0.48x + 0.07	y = 1.00x + 0.03	3857
6	y = 0.33x + 0.06	y = 0.91x + 0.01	3785
7	y = 0.24x + 0.07	y = 0.91x + 0.00	2906
8	y = 0.20x + 0.07	y = 0.84x - 0.01	3150
		Total	23038

Table G.4: Intermediate results on correlation for both MCP methods for the fifth experiment: January - July

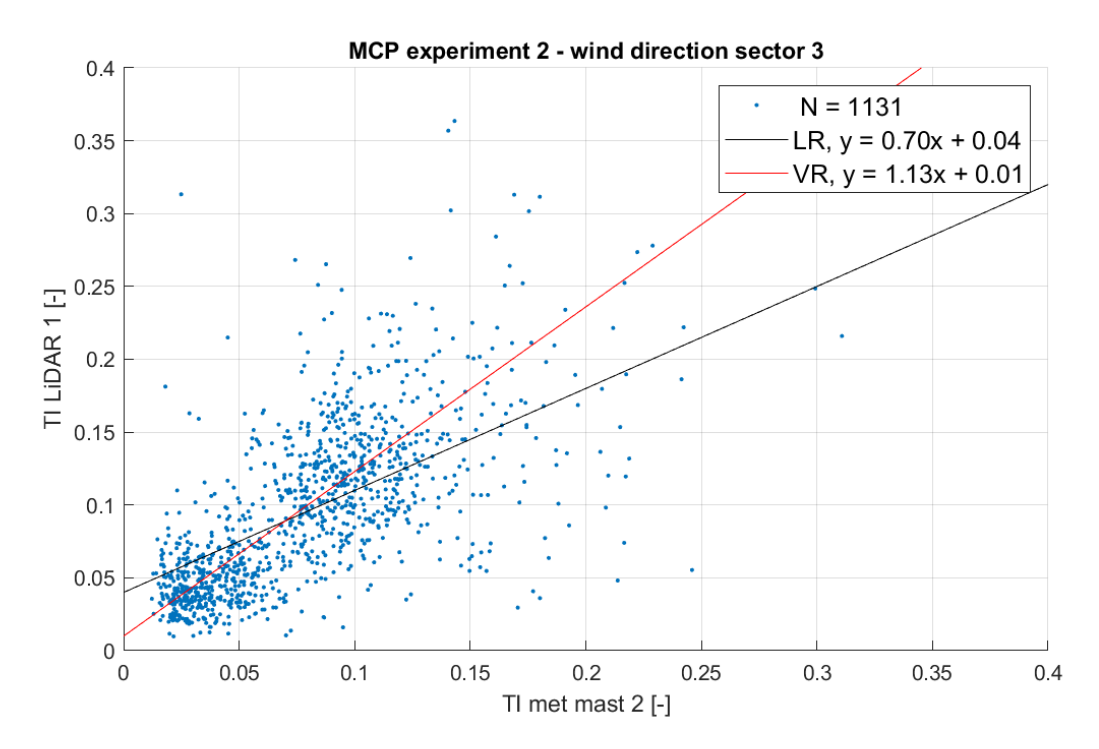


Figure G.1: Correlation via both MCP algorithms for experiment 2 - wind direction sector 3

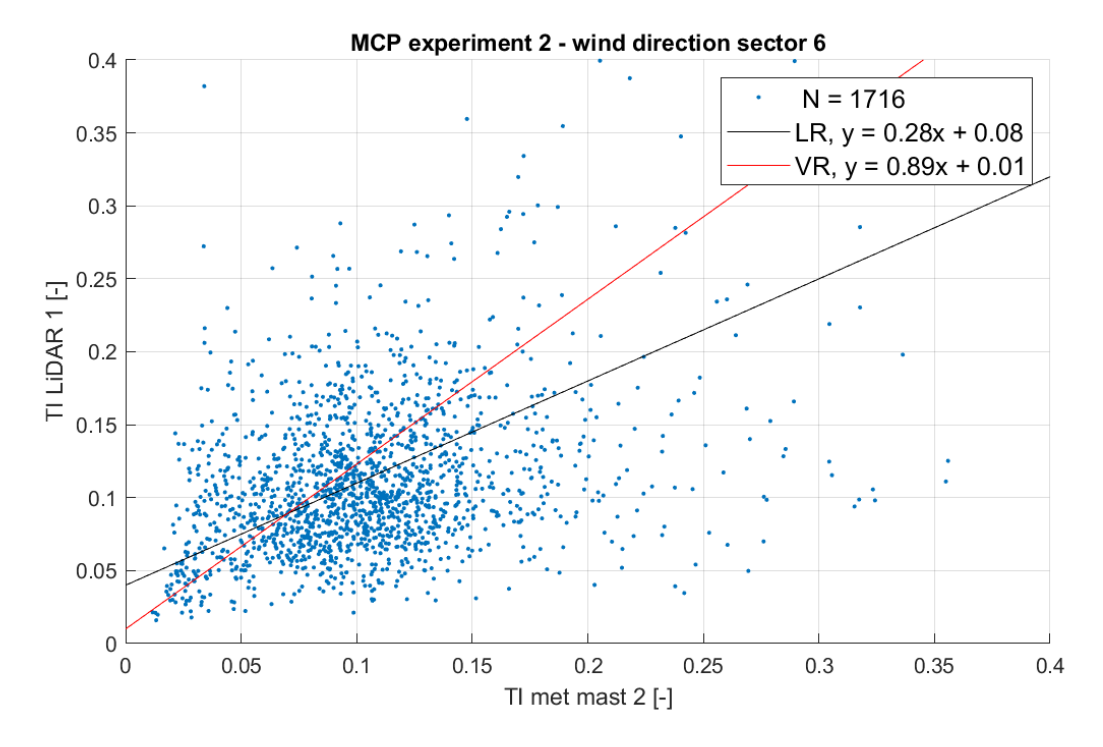


Figure G.2: Correlation via both MCP algorithms for experiment 2 - wind direction sector 6

Overview final results for prediction step in MCP

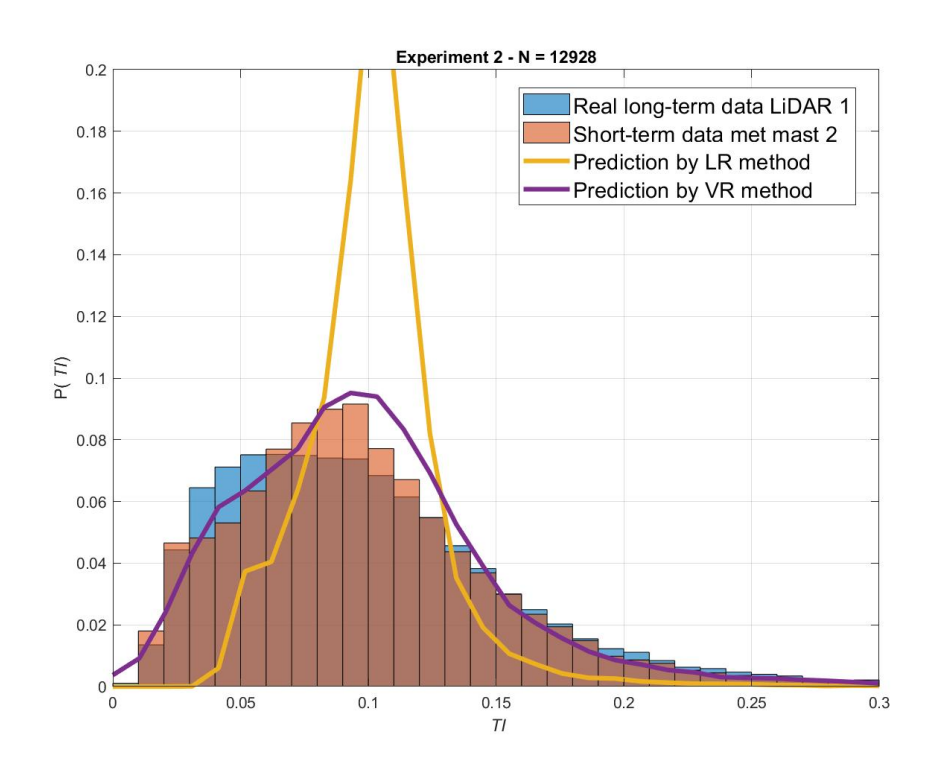


Figure H.1: Prediction via both MCP algorithms for experiment 2

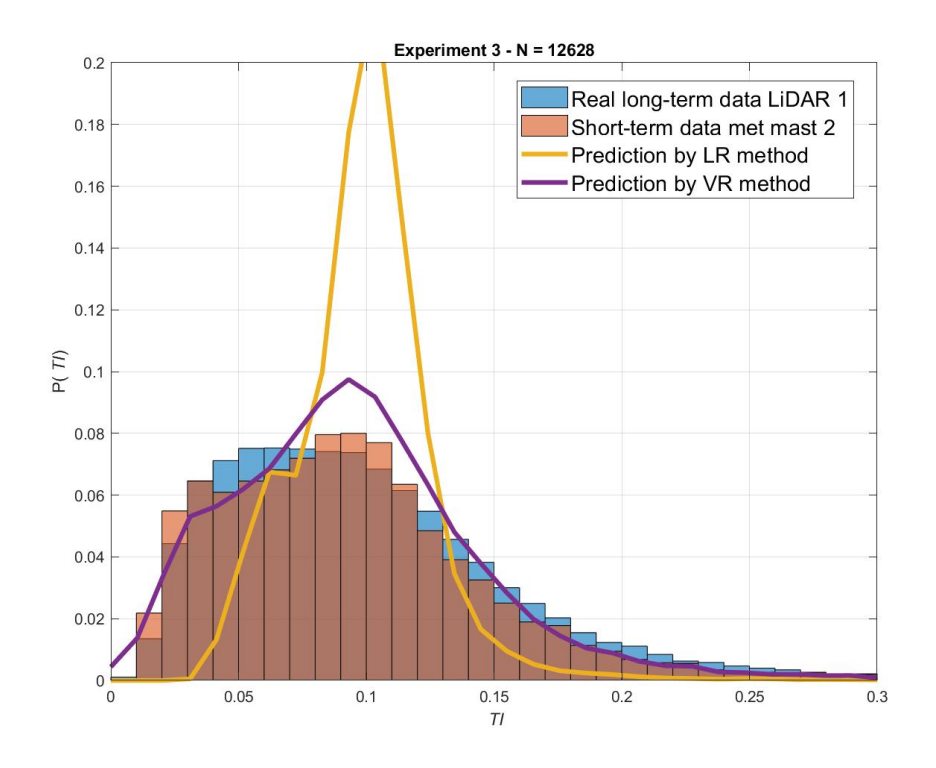


Figure H.2: Prediction via both MCP algorithms for experiment 3

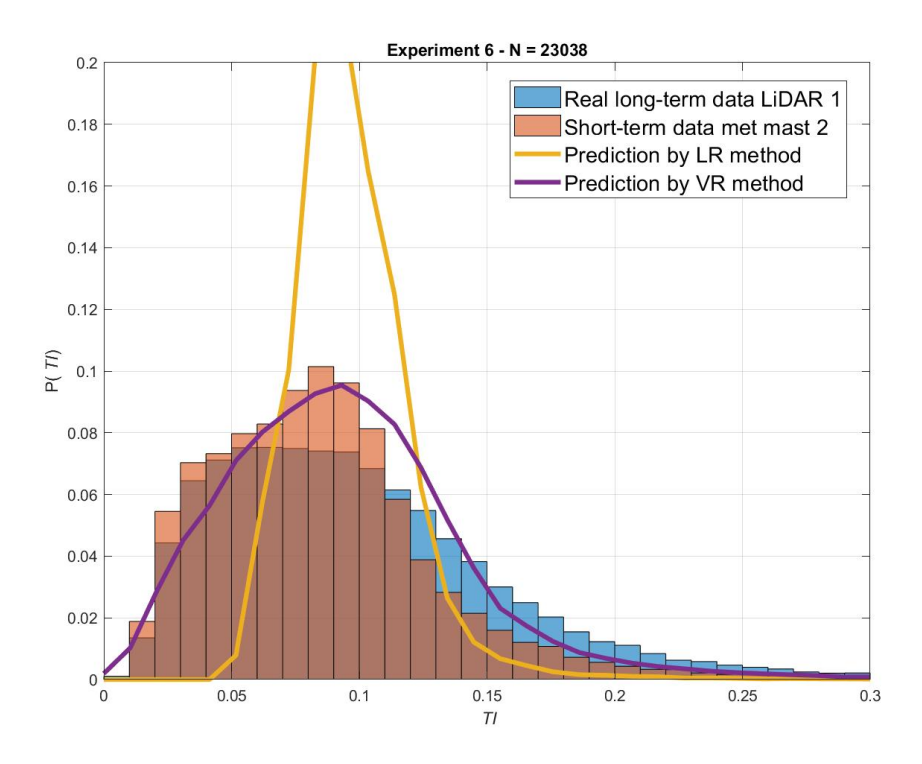


Figure H.3: Prediction via both MCP algorithms for experiment 6

- [1] Wikimedia Commons several gaussian distributions. https://commons.wikimedia.org/wiki/File:Normal Distribution PDF.svg. Accessed: 2019-09-03.
- [2] Internal boundary layer glossary. https://www.aiche.org/ccps/resources/glossary/process-safety-glossary/internal-boundary-layer. Accessed: 2020-05-10.
- [3] Fast, an aeroelastic computer-aided engineering (cae) tool for horizontal axis wind turbines. https://nwtc.nrel.gov/FAST, . Accessed: 2019-10-10.
- [4] Turbsim, a stochastic, full-field, turbulence simulator primarialy for use with inflowwind/aerodyn-based simulation tools. https://nwtc.nrel.gov/TurbSim, . Accessed: 2019-10-10.
- [5] Wikimedia Commons ordinary least squares. https://commons.wikimedia.org/wiki/File:Coefficient_of_Determination.svg. Accessed: 2019-09-03.
- [6] Lopende projecten windpark windplan blauw. https://www.rvo.nl/onderwerpen/bureau-energieprojecten/lopende-projecten/windparken/windpark-windplan-blauw. Accessed: 2019-09-17.
- [7] Turbsim a stochastic, full-field, turbulence simulator primarialy for use with inflowwind/aerodyn-based simulation tools. https://nwtc.nrel.gov/TurbSim. Accessed: 2019-10-15.
- [8] Het plan windplan windpark blauw. https://windplanblauw.nl/windplanblauw/. Accessed: 2019-09-17.
- [9] Zx 300 lidar by zx lidars. https://www.zxlidars.com/. Accessed: 2019-09-17.
- [10] Wikimedia Commons wind turbine size increase. https://bmeafl.com/the-project-proposal/. Accessed: 2019-09-03.
- [11] Wind field simulation (the user-friendly version). https://www.mathworks.com/matlabcentral/fileexchange/50041-wind-field-simulation-the-user-friendly-version. Accessed: 2019-11-15.
- [12] Why do we measure turbulence intensity? https://www.linkedin.com/pulse/ why-do-we-measure-turbulence-intensity-peter-clive/. Accessed: 2019-10-15
- [13] Can the wind industry bank on wind lidar? https://www.zxlidars.com/wp-content/uploads/2014/12/WPM-Expert-Report-Can-the-wind-industry-bank-on-wind-lidapdf. Accessed: 2019-10-15.
- [14] Wikimedia Commons wind turbine size increase. https://commons.wikimedia.org/wiki/File:Wind turbine size increase 1980-2015.png. Accessed: 2019-09-30.
- [15] Rakesh Aggarwal and Priya Ranganathan. Common pitfalls in statistical analysis: Linear regression analysis. *Perspectives in clinical research*, 8(2):100, 2017.
- [16] A Albers, AW Janssen, and J Mander. German test station for remote wind sensing devices. *measurement*, 3:1, 2009.
- [17] Sajid Ali, Sang-Moon Lee, and Choon-Man Jang. Forecasting the long-term wind data via measure-correlate-predict (mcp) methods. *Energies*, 11(6):1541, 2018.

[18] Ioannis Antoniou, Mike Courtney, Hans E Jørgensen, Torben Mikkelsen, Sabine Von Hunerbein, Stuart Bradley, Ben Piper, Michael Harris, Ignacio Marti, Mariano Aristu, et al. Remote sensing the wind using lidars and sodars. In *Proceedings EWEC*, 2007.

- [19] Roberto Lacal Arantegui and Arnulf Jäger-Waldau. Photovoltaics and wind status in the european union after the paris agreement. *Renewable and Sustainable Energy Reviews*, 81:2460–2471, 2018.
- [20] Cédric Arbez, Kossivi Tete, Antoine Amosse, Jean-Benoit Boucher, and Hussein Ibrahim. Met mast configuration and choice of sensors in cold climate conditions. *Measurement*, 95:156–165, 2017.
- [21] Lars Morten Bardal and Lars Roar Sætran. Influence of turbulence intensity on wind turbine power curves. *Energy Procedia*, 137:553–558, 2017.
- [22] W Barker, M Pitter, E Burin des Roziers, M Harris, and R Scullion. Can lidars measure turbulence? comparison between zephir 300 and an iec compliant anemometer mast, 2012.
- [23] Will Barker, M Harris, M Pitter, E Burin des Roziers, J Medley, and C Slinger. Lidar turbulence measurements for wind turbine selection studies: design turbulence. In *European Wind Energy Association Conference*, volume 10, 2014.
- [24] James P Barrett. The coefficient of determination—some limitations. *The American Statistician*, 28(1):19–20, 1974.
- [25] J Beltrán, L Cosculluela, C Pueyo, and JJ Melero. Comparison of measure-correlate-predict methods in wind resource assessments. In *European Wind Energy Conference and Exhibition*, pages 3280–3286, 2010.
- [26] Timothy A Bonin, Aditya Choukulkar, W Alan Brewer, Scott P Sandberg, Ann M Weickmann, Yelena L Pichugina, Robert M Banta, Steven P Oncley, and Daniel E Wolfe. Evaluation of turbulence measurement techniques from a single doppler lidar. Atmospheric Measurement Techniques, 10(8):3021–3039, 2017.
- [27] Clive Bonsall, Mark G Macklin, David E Anderson, and Robert W Payton. Climate change and the adoption of agriculture in north-west europe. *European Journal of Archaeology*, 5(1):9–23, 2002.
- [28] Larry S Bradshaw, E Petrescu, and I Grenfell. An initial analysis of relationships between 2-and 10-minute averaged winds at 10, 6, and 1.8 meters: Implications for fire behavior and danger applications. In *Preprints*, 5th Symp. on Fire and Forest Meteorology, Orlando, FL, Amer. Meteor. Soc, volume 4, 2003.
- [29] Arno J Brand, Joachim Peinke, and Jakob Mann. Turbulence and wind turbines. In *Journal of Physics: Conference Series*, volume 318, page 072005. IOP Publishing, 2011.
- [30] A Bustamante, L Vera-Tudela, and M Kühn. Evaluation of wind farm effects on fatigue loads of an individual wind turbine at the enbw baltic 1 offshore wind farm. In *Journal of Physics: Conference Series*, volume 625, page 012020. IOP Publishing, 2015.
- [31] Damien Caous, Christophe Bois, Jean-Christophe Wahl, Thierry Palin-Luc, and Julien Valette. Toward composite wind turbine blade fatigue life assessment using ply scale damage model. *Procedia engineering*, 213:173–182, 2018.
- [32] Livio Casella. A measure-correlation-predict method for turbulence intensity distribution assessment. *Wind Engineering*, 37(2):125–136, 2013.
- [33] Livio Casella. Performance analysis of the first method for long-term turbulence intensity estimation at potential wind energy sites. *Renewable energy*, 74:106–115, 2015.

[34] Prem Kumar Chaurasiya, Siraj Ahmed, and Vilas Warudkar. Comparative analysis of weibull parameters for wind data measured from met-mast and remote sensing techniques. *Renewable energy*, 115:1153–1165, 2018.

- [35] Jing Chen, Yongxing Jin, Qihuang Mao, Yingjie Xiao, Huafeng Wu, and Guochu Chen. Fourier hull fatigue assessment method's proposing and software development. *Sensors & Transducers*, 171(5):78, 2014.
- [36] Donald Cochrane and Guy H Orcutt. Application of least squares regression to relationships containing auto-correlated error terms. *Journal of the American statistical association*, 44(245):32–61, 1949.
- [37] Rachael V Coquilla, John Obermeier, and Bruce R White. Calibration procedures and uncertainty in wind power anemometers. *Wind Engineering*, 31(5):303–316, 2007.
- [38] Michael Courtney, Rozenn Wagner, and Petter Lindelöw. Commercial lidar profilers for wind energy: A comparative guide. In *Proc. European Wind Energy Conference, Brussels, Belgium,* 2008.
- [39] J-Å Dahlberg, Troels Friis Pedersen, and Peter Busche. Accuwind-methods for classification of cup anemometers. 2006.
- [40] Aiguo Dai. Drought under global warming: a review. Wiley Interdisciplinary Reviews: Climate Change, 2(1):45–65, 2011.
- [41] Wenbin Dong, Yihan Xing, and Torgeir Moan. Time domain modeling and analysis of dynamic gear contact force in a wind turbine gearbox with respect to fatigue assessment. *Energies*, 5(11):4350–4371, 2012.
- [42] J Feliciano, G Cortina, A Spear, and M Calaf. Generalized analytical displacement model for wind turbine towers under aerodynamic loading. *Journal of Wind Engineering and Industrial Aerodynamics*, 176:120–130, 2018.
- [43] International Organization for Standardization. Accuracy (trueness and precision) of measurement methods and results—part 1: general principles and definitions, 1994.
- [44] Dimitri Foussekis, F Mouzakis, P Papadopoulos, and P Vionis. Wind profile measurements using a lidar and a 100m mast. In *European Wind Energy Conference and Exhibition/Milan-Italy, EWEC*, 2007.
- [45] Sten Frandsen and Morten L Thøgersen. Integrated fatigue loading for wind turbines in wind farms by combining ambient turbulence and wakes. *Wind Engineering*, pages 327–339, 1999.
- [46] Sten Tronæs Frandsen. *Turbulence and turbulence-generated structural loading in wind turbine clusters*. 2007.
- [47] Gregg Freebury and Walter Musial. Determining equivalent damage loading for full-scale wind turbine blade fatigue tests. In 2000 ASME Wind Energy Symposium, page 50, 2000.
- [48] K Freudenreich and K Argyriadis. The load level of modern wind turbines according to iec 61400-1. In *Journal of Physics: Conference Series*, volume 75, page 012075. IOP Publishing, 2007.
- [49] Leo J Fritschen. A sensitive cup-type anemometer. *Journal of Applied Meteorology*, 6 (4):695–698, 1967.
- [50] John Roy Garratt. The atmospheric boundary layer. *Earth-Science Reviews*, 37(1-2): 89–134, 1994.
- [51] JR Garratt. The internal boundary layer—a review. *Boundary-Layer Meteorology*, 50 (1-4):171–203, 1990.

[52] Richard Gedney. Stress-life fatigue testing basics. Technical report, Quality Magazine, 2017. Accessed: 2019-10-28.

- [53] Asir Genc, Murat Erisoglu, Ahmet Pekgor, Galip Oturanc, Arif Hepbasli, and Koray Ulgen. Estimation of wind power potential using weibull distribution. *Energy Sources*, 27(9):809–822, 2005.
- [54] AH Giyanani, WAAM Bierbooms, and GJW Van Bussel. Analysis of inflow parameters using lidars. In *Proceedings of the 10th EAWE PhD seminar on wind energy in Europe, Orleans (France)*, 28-31 Oct. 2014. EAWE European Academy of Wind Energy, 2014.
- [55] Sven-Erik Gryning, Michael S Courtney, Ioannis Antoniou, and Torben Krogh Mikkelsen. On the study of wind energy at great heights using remote sensing techniques. 2007.
- [56] Kurt S Hansen, Rebecca J Barthelmie, Leo E Jensen, and Anders Sommer. The impact of turbulence intensity and atmospheric stability on power deficits due to wind turbine wakes at horns rev wind farm. *Wind Energy*, 15(1):183–196, 2012.
- [57] G Hayman. Mlife theory manual for version 1.00. National Renewable Energy Laboratory, Golden, CO, 74(75):106, 2012.
- [58] E Holstag. Improved bankability, the ecofys position on lidar use, 2013.
- [59] Roymond S Hunter, B Maribo Pedersen, TF Pedersen, H Klug, N van der Borg, N Kelley, and JÅ Dahlberg. Recommended practices for wind turbine testing and evaluation. 11. wind speed measurement and use of cup anemometry. 1. IEA, 1999.
- [60] Amr Mohamed Metwally Ismaiel and Shigeo Yoshida. Study of turbulence intensity effect on the fatigue lifetime of wind turbines. *Evergreen ISNN*, pages 2189–0420, 2018.
- [61] Daniel W Jaynes, Jon G McGowan, Anthony L Rogers, and James F Manwell. Validation of doppler lidar for wind resource assessment applications. In AWEA Windpower2007 Conference. Citeseer, 2007.
- [62] Sylvain M Joffre and Tuomas Laurila. Standard deviations of wind speed and direction from observations over a smooth surface. *Journal of Applied Meteorology*, 27(5):550–561, 1988.
- [63] Bonnie J Jonkman and Marshall L Buhl Jr. Turbsim user's guide. Technical report, National Renewable Energy Lab.(NREL), Golden, CO (United States), 2006.
- [64] Jason Jonkman, Sandy Butterfield, Walter Musial, and George Scott. Definition of a 5-mw reference wind turbine for offshore system development. Technical report, National Renewable Energy Lab.(NREL), Golden, CO (United States), 2009.
- [65] Jason M Jonkman, Marshall L Buhl Jr, et al. Fast user's guide. *National Renewable Energy Laboratory*, *Golden*, *CO*, *Technical Report No. NREL/EL-500-38230*, 2005.
- [66] Christoph W Kensche. Fatigue of composites for wind turbines. *International journal of fatigue*, 28(10):1363–1374, 2006.
- [67] Shigeo Kimura, Ken'ichi Abe, Kazuhiro Tsuboi, Bengt Tammelin, and Kohji Suzuki. Aerodynamic characteristics of an iced cup-shaped body. *Cold regions science and technology*, 33(1):45–58, 2001.
- [68] L Kristensen. The perennial cup anemometer. Wind Energy: An International Journal for Progress and Applications in Wind Power Conversion Technology, 2(1):59–75, 1999.
- [69] Pravin A Kulkarni, Weifei Hu, Ashwinkumar S Dhoble, and Pramod M Padole. Statistical wind prediction and fatigue analysis for horizontal-axis wind turbine composite material blade under dynamic loads. Advances in Mechanical Engineering, 9(9): 1687814017724088, 2017.

[70] Steven Lang and Eamon McKeogh. Lidar and sodar measurements of wind speed and direction in upland terrain for wind energy purposes. *Remote Sensing*, 3(9):1871–1901, 2011.

- [71] Jiale Li and Xiong Bill Yu. Lidar technology for wind energy potential assessment: Demonstration and validation at a site around lake erie. *Energy Conversion and Management*, 144:252–261, 2017.
- [72] Brian Loza, Josué Pacheco-Chérrez, Diego Cárdenas, Luis I Minchala, and Oliver Probst. Comparative fatigue life assessment of wind turbine blades operating with different regulation schemes. *Applied Sciences*, 9(21):4632, 2019.
- [73] John F Mandell, Robert M Reed, and Daniel D Samborsky. *Fatigue of fiberglass wind turbine blade materials*. Sandia National Laboratories Contractor Report SAND92-7005. Albuquerque, NM, 1992.
- [74] James F Manwell, Jon G McGowan, and Anthony L Rogers. *Wind energy explained: theory, design and application.* John Wiley & Sons, 2010.
- [75] Charles F Marvin. Recent advances in anemometry. *Bulletin of the American Meteorological Society*, 15(6-7):169–172, 1934.
- [76] Daniel A Mazzarella. An inventory of specifications for wind measuring instruments. *Bulletin of the American Meteorological Society*, 53(9):860–871, 1972.
- [77] Daniel Miessler. The difference between accuracy and precision. Business, 2019.
- [78] Philippa L Moore and Geoff Booth. *The welding engineer's guide to fracture and fatigue*. Elsevier, 2014.
- [79] Ranganath R Navalgund, V Jayaraman, and PS Roy. Remote sensing applications: An overview. *Current Science* (00113891), 93(12), 2007.
- [80] Jennifer F Newman and Andrew Clifton. Quantifying the effect of lidar turbulence error on wind power prediction. Technical report, National Renewable Energy Lab.(NREL), Golden, CO (United States), 2016.
- [81] Jennifer F Newman, Andrew Clifton, Matthew J Churchfield, and Petra Klein. Improving lidar turbulence estimates for wind energy. In *Journal of Physics: Conference Series*, volume 753, page 072010. IOP Publishing, 2016.
- [82] Rogier Pieter Louis Nijssen. Fatigue life prediction and strength degradation of wind turbine rotor blade composites. *Contractor Report SAND2006-7810P*, *Sandia National Laboratories*, *Albuquerque*, *NM*, 2006.
- [83] Markus Pahlow, Marc B Parlange, and Fernando Porté-Agel. On monin-obukhov similarity in the stable atmospheric boundary layer. *Boundary-Layer Meteorology*, 99(2): 225–248, 2001.
- [84] KH Papadopoulos, NC Stefantos, U Schmidt Paulsen, and E Morfiadakis. Effects of turbulence and flow inclination on the performance of cup anemometers in the field. *Boundary-Layer Meteorology*, 101(1):77–107, 2001.
- [85] B Maribo Pedersen, Kurt S Hansen, Stig Øye, Michael Brinch, and Ole Febian. Some experimental investigations on the influence of the mounting arrangements on teh accuracy of cup-anemometer measurements. *Journal of Wind Engineering and Industrial Aerodynamics*, 39(1-3):373–383, 1992.
- [86] Joachim Peinke, Stephan Barth, Frank Böttcher, Detlev Heinemann, and Bernhard Lange. Turbulence, a challenging problem for wind energy. *Physica A: Statistical Mechanics and its Applications*, 338(1-2):187–193, 2004.

[87] Alfredo Peña and Charlotte Bay Hasager. Remote sensing for wind energy. 2011.

- [88] Alfredo Pena, Charlotte Bay Hasager, Sven-Erik Gryning, Michael Courtney, Ioannis Antoniou, Torben Mikkelsen, and Paul Sørensen. Offshore winds using remote sensing techniques. In *Journal of Physics: Conference Series*, volume 75, page 012038. IOP Publishing, 2007.
- [89] Alfredo Peña, Charlotte Bay Hasager, Sven-Erik Gryning, Michael Courtney, Ioannis Antoniou, and Torben Mikkelsen. Offshore wind profiling using light detection and ranging measurements. Wind Energy: An International Journal for Progress and Applications in Wind Power Conversion Technology, 12(2):105–124, 2009.
- [90] Santiago Pindado, Antonio Barrero-Gil, and Alfredo Sanz. Cup anemometers' loss of performance due to ageing processes, and its effect on annual energy production (aep) estimates. *Energies*, 5(5):1664–1685, 2012.
- [91] Santiago Pindado, Imanol Pérez, and Maite Aguado. Fourier analysis of the aerodynamic behavior of cup anemometers. *Measurement Science and Technology*, 24(6): 065802, 2013.
- [92] Santiago Pindado, Javier Cubas, and Félix Sorribes-Palmer. The cup anemometer, a fundamental meteorological instrument for the wind energy industry. research at the idr/upm institute. *Sensors*, 14(11):21418–21452, 2014.
- [93] Robin L Plackett. Karl pearson and the chi-squared test. *International Statistical Review/Revue Internationale de Statistique*, pages 59–72, 1983.
- [94] Adam Podhala, Steve Bowen, Michal Lorinc, and Anwesha Bhattacharya. Global catastrophe recap. 2019.
- [95] Oliver Probst and Diego Cárdenas. State of the art and trends in wind resource assessment. *Energies*, 3(6):1087–1141, 2010.
- [96] Patrick Ragan and Lance Manuel. Comparing estimates of wind turbine fatigue loads using time-domain and spectral methods. *Wind engineering*, 31(2):83–99, 2007.
- [97] Gilbert S Raynor, S Sethuraman, and Robert M Brown. Formation and characteristics of coastal internal boundary layers during onshore flows. *Boundary-Layer Meteorology*, 16(4):487–514, 1979.
- [98] Guorui Ren, Jinfu Liu, Jie Wan, Fei Li, Yufeng Guo, and Daren Yu. The analysis of turbulence intensity based on wind speed data in onshore wind farms. *Renewable energy*, 123:756–766, 2018.
- [99] Anthony L Rogers, John W Rogers, and James F Manwell. Comparison of the performance of four measure–correlate–predict algorithms. *Journal of wind engineering and industrial aerodynamics*, 93(3):243–264, 2005.
- [100] Alejandro Romo Perea, Javier Amezcua, and Oliver Probst. Validation of three new measure-correlate-predict models for the long-term prospection of the wind resource. *Journal of renewable and sustainable energy*, 3(2):023105, 2011.
- [101] Mathieu Rouaud. Probability, statistics and estimation. *Propagation of uncertainties*, 2013.
- [102] M Sanuki and S Kimura. Some aerodynamic aspects deduced for the start and stop experiment of three-and four-cup anemometer. *Papers in Meteorology and Geophysics*, 5(2):186–188, 1954.
- [103] S Sanz. Validation of lidar measurements in extremely complex terrain. *Wind Europe*, 2016.

[104] Ameya Sathe, Jakob Mann, Julia Gottschall, and Michael S Courtney. Can wind lidars measure turbulence? *Journal of Atmospheric and Oceanic Technology*, 28(7):853–868, 2011.

- [105] Ameya Rajiv Sathe. Influence of wind conditions on wind turbine loads and measurement of turbulence using lidars. 2012.
- [106] George AF Seber and Alan J Lee. *Linear regression analysis*, volume 329. John Wiley & Sons, 2012.
- [107] Javier Serrano-González and Roberto Lacal-Arántegui. Technological evolution of onshore wind turbines—a market-based analysis. *Wind Energy*, 19(12):2171–2187, 2016.
- [108] Mahmood M Shokrieh and Roham Rafiee. Simulation of fatigue failure in a full composite wind turbine blade. *Composite Structures*, 74(3):332–342, 2006.
- [109] David A Smith, Michael Harris, Adrian S Coffey, Torben Mikkelsen, Hans E Jørgensen, Jakob Mann, and Régis Danielian. Wind lidar evaluation at the danish wind test site in høvsøre. Wind Energy: An International Journal for Progress and Applications in Wind Power Conversion Technology, 9(1-2):87–93, 2006.
- [110] H Söker. Loads on wind turbine blades. In *Advances in Wind Turbine Blade Design* and *Materials*, pages 29–58. Elsevier, 2013.
- [111] KP Soman and KB Misra. A least square estimation of three parameters of a weibull distribution. *Microelectronics Reliability*, 32(3):303–305, 1992.
- [112] Roland B Stull. *An introduction to boundary layer meteorology*, volume 13. Springer Science & Business Media, 2012.
- [113] Herbert J Sutherland. A summary of the fatigue properties of wind turbine materials. Wind Energy: An International Journal for Progress and Applications in Wind Power Conversion Technology, 3(1):1–34, 2000.
- [114] E Tatsuo, M Koichi, T Kiyohumi, K Kakuichi, and M Masanori. Damage evaluation of metals for random of varying loading-three aspects of rain flow method. In *Mechanical behavior of materials, Symp. Proc., Soc. Materials Scientists*, pages 21–24, 1974.
- [115] Morten Lybech Thøgersen, Maurizio Motta, Thomas Sørensen, and Per Nielsen. Measure-correlate-predict methods: Case studies and software implementation. In European Wind Energy Conference & Exhibition, page 10, 2007.
- [116] John Twidell and Tony Weir. Renewable energy resources. Routledge, 2015.
- [117] Nikola Vasiljevic, Andrea Vignaroli, Andreas Bechmann, and Rozenn Wagner. Digitizing scanning lidar measurement campaign planning.
- [118] Paul S Veers, Thomas D Ashwill, Herbert J Sutherland, Daniel L Laird, Donald W Lobitz, Dayton A Griffin, John F Mandell, Walter D Musial, Kevin Jackson, Michael Zuteck, et al. Trends in the design, manufacture and evaluation of wind turbine blades. Wind Energy: An International Journal for Progress and Applications in Wind Power Conversion Technology, 6(3):245–259, 2003.
- [119] Herman Frederik Veldkamp. Chances in wind energy: a probalistic approach to wind turbine fatigue design. 2006.
- [120] HM Villanueva Lopez. The illusion of power curves: Understanding ti, shear, and atmospheric stability in power performance. 2014.
- [121] Niels Waars. Lidar and mcp in wind resource estimations above measurement-mast height. 2017.

[122] Rozenn Wagner, Torben Mikkelsen, and Michael Courtney. Investigation of turbulence measurements with a continuous wave, conically scanning lidar. 2009.

- [123] Eric W Weisstein. Area moment of inertia. 2009.
- [124] Annette Westerhellweg, Beatriz Canadillas, Andreas Beeken, and Thomas Neumann. One year of lidar measurements at fino1-platform: Comparison and verification to metmast data. In *10th German Wind Energy Conference, Bremen*, pages 18–19, 2010.
- [125] M. Zaayer. Introduction to wind turbines, 2019.
- [126] Jie Zhang, Souma Chowdhury, Achille Messac, and Bri-Mathias Hodge. A hybrid measure-correlate-predict method for long-term wind condition assessment. *Energy conversion and management*, 87:697–710, 2014.